EXPERIMENTAL TESTING OF A SHAPE MEMORY ALLOY SLAT COVE FILLER FOR NOISE REDUCTION

A Thesis

by

ANDREW LEATON

Submitted to the Office of Graduate and Professional Studies of
Texas A&M University
in partial fulfillment of the requirements for the degree of

MASTER OF SCIENCE

Chair of Committee,	Darren J. Hartl
Committee Members,	Thomas W. Strganac
	Michael B. Pate
Head of Department,	Rodney Bowersox

August 2020

Major Subject: Aerospace Engineering

ABSTRACT

Aircraft noise is a source of disruption and annoyance to those living within close proximity to airports. Airframe noise is a main contributor to the overall noise level created by aircraft during approach and landing. One of the major sources of acoustic noise is the leading-edge slat, a high lift device on general transport aircraft. The slat has complex geometry from the dual role they perform on the wing leading edge during flight. During takeoff and landing, high lift devices are deployed to provide supplemental lift at low velocity. During cruise, additional camber and separated lifting surfaces are unnecessary to produce the required lift and the devices are retracted against the main wing, with the slat providing a cove with which the wing leading edge can fit into, creating a more efficient airfoil. Because of this complex geometry, when the slat deploys, flow on the pressure side of the wing separates and circulates within the cove of the slat. There are several known noise production mechanisms in this flow field. The slat cove filler (SCF) has been proven to be an effective tool in the reduction of unsteadiness in the flow, and thus noise radiated to the far field. The current SCF utilizes a shape memory alloy (SMA) insert that redirects flow along an acoustically advantageous path, avoiding circulation and reducing noise. Using the Texas A&M University 3 ft x 4 ft wind tunnel, the noise reduction capabilities of an SMA-based SCF have been proven for the first time experimentally across multiple flight conditions (angle of attack, %-deployment, and flow velocity). Structural assessments were conducted as well using non-intrusive means to obtain displacement and geometric information on the SCF under flow. Aerodynamic measures were compared between experimental setups with and without the SCF in place, with minor variations in pressure, lift, and drag distribution when the high lift devices were fully deployed. Additional acoustic savings may be discovered in future research by altering the geometry of the SCF to reflect the flow conditions specific to the length and velocity scale.

DEDICATION

To my family, Aliya, and dog Newton. Thank you for supporting me through the years.

ACKNOWLEDGMENTS

This work was done in collaboration with NASA Structural Acoustic Branch at the LaRC under prime award number NNL09AA00A. Thank you to Dr. Hartl, Dr. Travis Turner, Dr. Thomas Strganac, and Dr. Michael Pate for funding and guiding my education and research. An enormous debt of gratitude is due to Dr. Travis Turner (thesis committee special appointee) for his funding, assistance, and edits over the course of this project. Additionally, thank you to William Scholten for guidance, and Pedro Leal, William Scholten, Madalyn Mikkelsen, Hannah Stroud, Patrick Walgren, and Kevin Lieb for writing assistance. A final thank you to Nik Zawodny of NASA Langley for advice on microphone placement.

CONTRIBUTORS AND FUNDING SOURCES

Contributors

This work was supported by a thesis committee consisting of Professors Darren Hartl and Thomas Strganac of the Department of Aerospace Engineering, Professor Michael Pate of the Department of Mechanical Engineering, and Dr. Travis Turner of NASA Langley Research Center.

Experimental wind tunnel testing was completed with the assistance of William Scholten, Kevin Lieb, Mitchell Mu, and Jake Schrass. Post processing contributions were made by William Scholten, Ryan Patterson, Trent White, and Kevin Lieb.

Funding Sources

Graduate study was supported by Texas A&M University and NASA Langley Research Center.

NOMENCLATURE

SCF	Slat Cove Filler
SMA	Shape Memory Alloy
Treated	Slat with attached Slat Cove Filler
Untreated	Slat without attached Slat Cove Filler
TAMU	Texas A&M University
DIC	Digital Image Correlation
CRM	Common Research Model
NASA	National Aeronautics and Space Administration
dB	Decibel
SPL	Sound Pressure Level
OASPL	Overall Sound Pressure Level
RPM	Rotations Per Minute
NiTi	Nickel Titanium
CSM	Cross-Spectral Matrix
PSF	Point Spread Function
FFT	Fast Fourier Transform
TL	Tranform Length
RMS	Root Mean Square

TABLE OF CONTENTS

Page

LIST OF FIGURES

FIGURE Page

LIST OF TABLES

TABLE Page

1. INTRODUCTION AND LITERATURE REVIEW

1.1 Background

Air travel, transporting both people and products, has only increased since its inception over a century ago. With increases in frequency of flights comes advances in aircraft technology and regulation. The Concorde, for instance, was the first commercially available supersonic transport aircraft, which could traverse the Atlantic in under three hours. However, due to noise concerns, the vehicle could not exploit its state-of-the-art supersonic technology, and was required to fly subsonically over land [1]. In every facet of air travel, from the most progressive to the most trivial, the acoustic production of the aircraft is a top priority, as is mandated by current international standards. In 2013, the International Civil Aviation Organization, a United Nations aviation-focused body, stipulated that new aircraft must be at least 7 EPNdB (effective perceived noise in decibels) quieter than previous generations of aircraft [2]. Those most impacted by the dramatic uptick in air travel reside closest to their point of departure and entry. The amount of noise produced by aircraft has long been problematic for communities nearby airports. Studies have even related increased noise caused by air travel near Heathrow airport with increased risk of stroke, heart disease, and cardiovascular disease [3]. The engines that propel the aircraft are commonly thought to be the culprit of the majority of this noise. However, advances in engine technology in recent decades have reduced this source by a significant margin, especially during landing [4], making airframe noise a leading contributor. The landing and approach phases of flight are particularly relevant to noise reduction, as the aircraft is closest to residential areas. Within the category of airframe noise, unsteadiness and circulation of flow over high lift devices make up a large portion of the total noise creation [5]. During takeoff and landing, aircraft speed is relatively low, therefore, high-lift devices are deployed to provide the additional lift needed to maintain flight. A high lift device extending from the wing leading edge is referred to as a slat, and from the trailing edge is referred to as a flap.

Flaps, due to flow around the wing, typically have a cross section resembling an airfoil. Slats, on the other hand, have much more complicated geometries. This geometry arises from the dual role slats perform on the wing leading edge during flight [6]. During takeoff and landing, high lift devices are deployed to increase effective lift at low velocity. During cruise this supplemental lift is no longer necessary, and the high lift devices are retracted against the wing. Because of this retraction, the slat must have a hollow trailing edge cove into which the main wing fits during cruise, providing an aerodynamically conducive assembly. This geometry results in flow irregularities created near the slat cove when fully deployed. The geometric discontinuity develops flow separation and circulation within the cove. A shear layer is created between the circulating flow within the cove and flow traveling around the cove. The interaction between these two flow conditions is a source of airframe noise, and is schematically detailed in Figure 1.1. The mechanism behind many aeroacoustic sources can be summarized as vortical structures, such as those in boundary layers or created by vortex shedding, being partially converted to acoustic signals when moving past geometric inconsistencies [7]. A reduction in the acoustic source of the slat will be attempted using an experimental flow path adjustment method, referred to as the slat cove filler (SCF).

1.2 Slat Cove Filler

One method to reduce the unsteadiness in the flow within the slat cove involves placing a structural impediment connecting the front of the cove to the slat trailing edge. This concept was referred to as the slat cove filler, and its shape was derived from the path of a flow isobar. This insert redirected flow along an acoustically advantageous path. Previous research [8, 9, 10, 11] concluded that noise level was reduced by this alteration of flow over the slat using a SCF (depicted in Figure 1.1). These conclusions are not based on an SMA SCF, though.

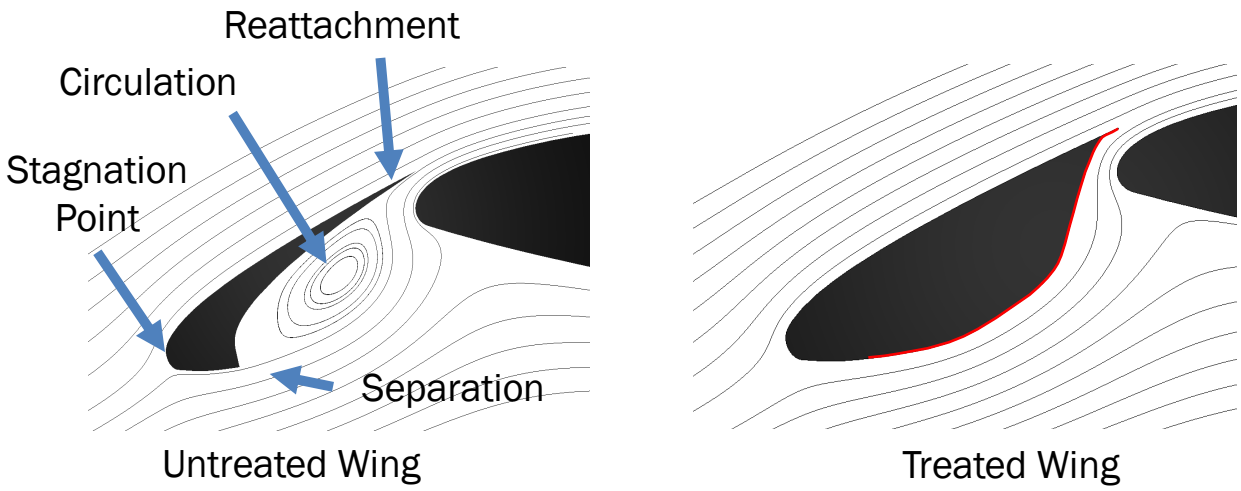

Figure 1.1: Streamlines around the deployed slat with and without the SCF. Treated refers to the slat with the SMA-based SCF in place, whereas untreated refers simply to an unchanged slat.

The role of the SCF is twofold: i) provide adequate stiffness against aerodynamic loading when deployed, and ii) snap into a stowed configuration within the cove during cruise. These conflicting requirements (stiff when deployed, compliant when retracted) led to non-typical material selection. Standard aerospace materials, such as aluminum and steel, did not possess the structural modularity necessary for this task. Due to the high strains the SCF was subject to during deployment and retraction [12], a particular type of material was needed. The unique phase transformation of shape memory alloys (SMA) provided an ideal solution [5].

1.3 Shape Memory Alloys

Shape memory alloys are a type of active material used in many engineering applications due to a coupling of thermal energy and mechanical work. With sufficient energy input, whether mechanical or thermal, SMAs will respond in a non-linear manner due to a solid phase transformation (from a cubic austenite phase to a tetragonal martensite phase, or vise versa [13]). SMAs can recover large amounts of inelastic strain (up to 5-10% in uniaxial test [14]) due to a solid phase-transformation from high temperature, low stress austenite to low temperature, high stress martensite, given a thermal or mechanical input. Shape memory alloys are commonly used in or-

thodontic braces [15], medical stents and catheters [16], and specialty eyeglass frames [17]. One way to characterize the current state of an SMA is by using martensitic volume fraction. Martensitic volume fraction is defined as the volumetric ratio between the portion of the sample that currently occupies a martensitic variant, and the total sample. The application of this stable and repeatable phase transformation (in the context of the SCF) is depicted in Figure 1.2, in which the slat is fully deployed in austenite with only aerodynamic loading (left), then during the retraction cycle (top), high strains begin a phase transformation from austenite to martensite. Once the SCF is fully stowed (top right), large portions of the SMA transform to a variant of martensite (i.e. the sample has high martensitic volume fraction) due to high strains. Finally, following a deployment cycle (bottom right), the material would recover all strain and return to austenite.

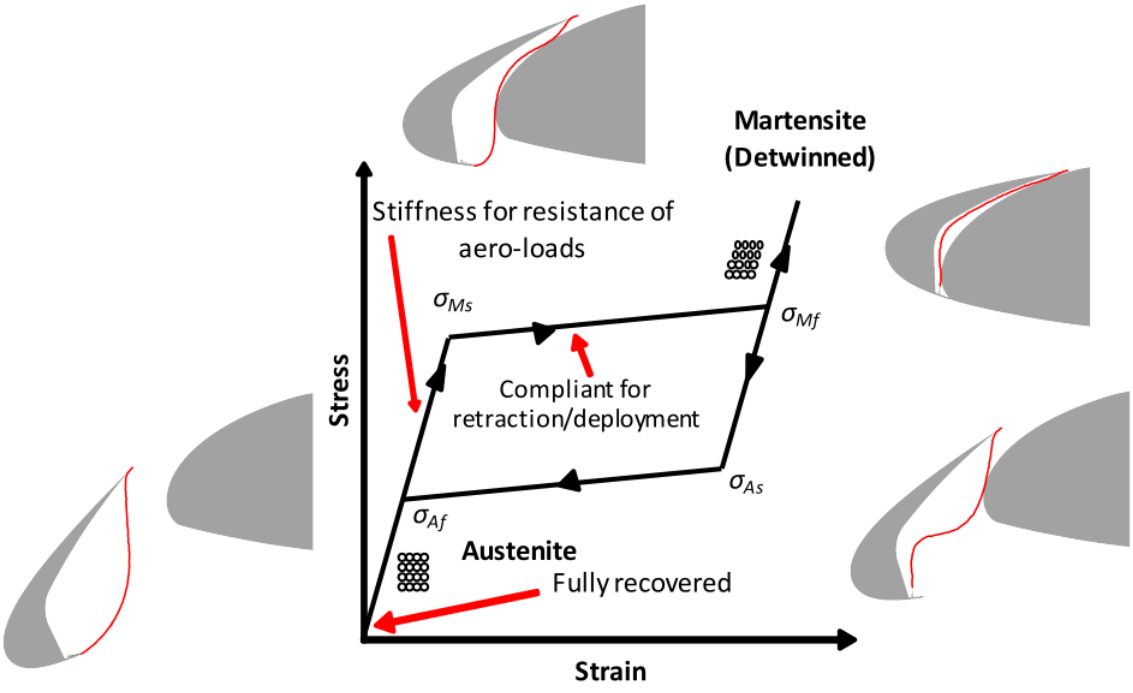

Figure 1.2: Phase diagram of SMA.

The multifaceted nature of SMAs can be attributed to the internal crystal structure of the constituent elements (e.g. NiTi in this work) before and after a phase change. As depicted in Fig-

ure 1.3, SMAs traditionally occupy 3 main phases. The first is austenite, which maintains a cubic structure and has its own material properties (A_s, A_f, C_A, E_A, etc). A_s and A_f refer to the temperatures at which zero-stress SMA would begin and end the transformation from martensite to austenite, respectively. C_A indicates that stress influence coefficient of austenite (i.e the slope of the austenite transformation surface in stress-temperature space), and E_A describes the elastic modulus of austenite. The other phase SMAs can occupy is martensite, which has its own properties as well (M_s, M_f, C_M, E_M, etc), and has twinned and detwinned variants. The martensitic properties listed are analogous to those described above for austenite.

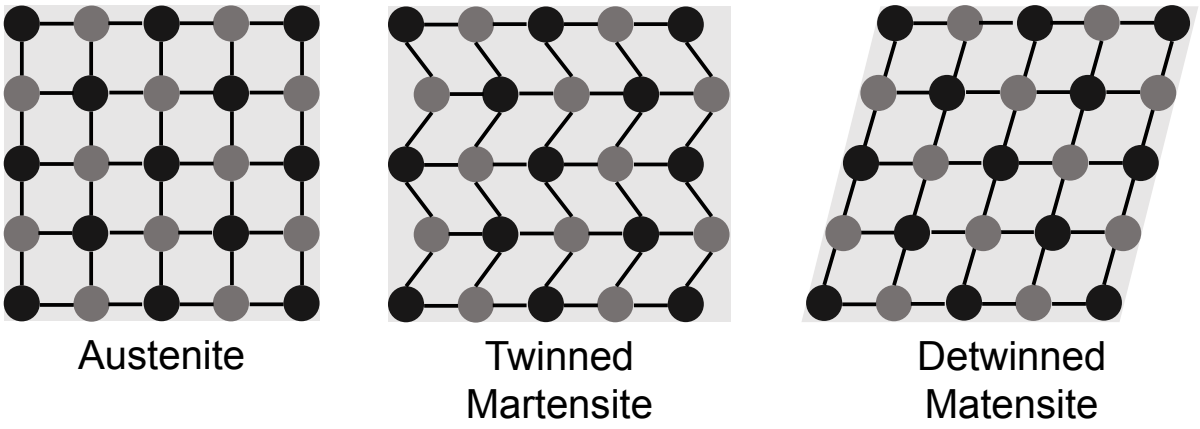

Figure 1.3: Structure of SMA in various phases.

Twinned martensite develops when the SMA cools below M_f without sufficient stress to detwin the internal micro-structure. The structure of a twinned variant is sometimes referred to as self-accommodating [18], describing the lack of macro-scale crystal directionality. Typically while demonstrating the other major property of SMAs, the shape memory effect, twinned martensite is deformed to create detwinned martensite. With a thermal input, the detwinned martensite transitions to cubic austenite and the deformation is recovered, returning to the original structure. The shape memory effect, while widely used in other SMA applications, was not utilized for this work. Many more complexities and nuance exists surrounding the shape memory effect, but are not ap-

plicable to this work, and therefore not covered. The detwinning process is a result of an applied stress and generates large-scale directionality within the crystal structure of the SMA. This cycle of recovering strain endured by the transition between austenite and martensite phases is referred to as superelasticity, a property inherent in SMAs at temperatures above A_f and only mechanical inputs. Specifically for this work, where there is no large change in temperature, the SCF is still able to recover large amounts of inelastic strain caused by mechanical inputs, as its temperature remains above A_f (the minimum temperature needed to completely transform the SMA into austenite). Therefore, when under high amounts of stress, the SCF locally changes from austenite to martensite, and when that stress is removed, areas of martensite return to austenite.

1.3.1 SMAs in Aerospace Applications

The idea behind using SMAs for aerospace applications is far from novel. While the SMA SCF has been explored both experimentally and computationally, only structural and aerodynamic responses of a 3D printed slat have been considered in the past [19]. This work specifically contributes to the body of knowledge surrounding the SMA SCF by performing aerodynamic and structural tests using improved materials (steel slat instead of 3D printed) and incorporating acoustic beamforming technology to spatially map noise creation as a result of the slat cove. The 3 ft x 4 ft Texas A&M University wind tunnel was used to record all aerodynamic and aeroacoustic data, and Digital Image Correlation techniques were utilized for structural data. In 2017, students at Texas A&M University conducted similar wind tunnel testing of a model scale SMA SCF [20], and found minor variations in aerodynamic results between the treated and untreated slat. For brevity, the treated configuration referred to the slat with the SMA SCF attached, whereas the untreated configuration did not contain the SCF. These terms are used extensively throughout this work to compare the wing with the SCF in place to an unmodified wing. This work acted as a base on which the current research relied, with some modern additions. Structurally, Digital Image Correlation testing within a wind tunnel has been utilized previously to extract accurate three dimensional shape data without flow impediments [21]. Stroud et al. conducted wind tunnel tests using SMA actuators to change the outer mold line from a normal configuration to a high

lift configuration. For this work, Digital Image Correlation was successfully used to verify shape characteristics of the wing.

Hartl and Lagoudas [22] detailed many current applications for shape memory alloys, such as their use on fixed and rotary wing aircraft, as well as spacecraft. Barbarino and company compiled a collection of morphing-wing designs utilizing shape memory alloy actuators [23]. Most often, these designs involved changing the camber or twist of the wing, which differs both in execution and result from the SCF concept. Strelec and coworkers computationally explored the possibility of shape memory alloy actuators embedded under the airfoil for geometry modification with the overall goal of efficiency improvement [24]. The modified airfoil demonstrated increased lift, and experimental models validated many of the computational claims. Finally, Roh et al. [25] used ABAQUS and SMA thin film actuators to change the outer mold line of an aircraft wing, and compared the modified wing results to a typical wing with a solid and slotted flap. Roh found that the morphing airfoil delayed flow separation for both flap types, improving aerodynamic performance.

1.3.2 Aeroacoustic Wind Tunnel Testing

While the study of aeroacoustics is not new, few schools have the facilities needed to effectively collect reliable data. Work done by Vishwanathan et al. at Virginia Tech utilized a 6 ft x 6 ft test section and aeroacoustic wind tunnel to better characterize flow behavior, with the end goal of improving CFD validation testing [26]. Mayer and coworkers at the University of Bristol used a close circuit, open section concept to test various airfoils using airflow up to 120 m/s (393 ft/s) [27]. Pascioni et al. at Florida State University have demonstrated both an open and closed test section system [28]. Their primary acoustic testing occurs within a open-jet anechoic chamber, but, due to differences in the aerodynamics experienced by bodies in flow in an open compared to close section, an additional section was utilized. This closed section had acrylic and glass walls to contain flow, but these surfaces are also highly reflective to acoustic sources, possibly contaminating results.

1.4 Research Goals and Plan

This work will strive to convey the structural, aerodynamic, and aeroacoustic behavior of the SMA-based SCF using new methods and materials available to Texas A&M University. Specifically, the scale model behavior will be examined at multiple angles of attack, flow velocities, and deployment levels. Structurally, the shape and deflection of the SCF will be presented and compared across multiple flow conditions. Aerodynamically, measures such as lift, drag (as well as their coefficients), and coefficient of pressure will be shown for both the treated and untreated slat. This data is used to estimate the effectiveness of the SCF, specifically that the SCF inclusion should have little effect on the aerodynamic characteristics of the wing. Finally, aeroacoustic results will be presented demonstrating the effectiveness of noise reduction using the SMA-based SCF. Dynamic tests will also be depicted, presenting follow-on research opportunities.

2. WIND TUNNEL MODEL AND SCF CONSTRUCTION

2.1 CRM Experimental Model

[1] For this work, a 1/16th scale model based off a 2D cross section of the NASA-Boeing Common Research Model (CRM) [29] was utilized for experimental testing. The exterior of the wing was made of 3D printed ABS plastic, supported by a steel and aluminum interior skeleton, as depicted in Figure 2.1.

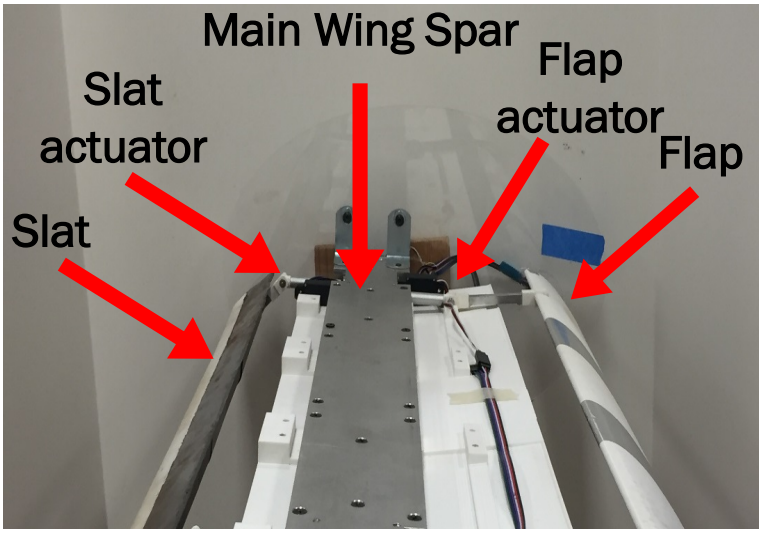

Figure 2.1: Structural setup of CRM model wing.

Twelve 3D-printed shells were created, which made up the outer mold line of the wing, with six placed on the suction side and six placed on the pressure side of the wing. Each shell was fastened into the steel structure by 4 support bolts, and the seams created by the intersection of of two shells (as well as the bolt heads) were covered in packaging tape. This tape was used to minimize the aerodynamic effect of these small geometric discontinuities. The tape, made

[1]This chapter has content from [35]; reprinted by permission of the American Institute of Aeronautics and Astronautics, Inc.

by Intertape Polymer Group, was chosen because of its smooth exterior, strong adherence, and residue-free removal. The flap was made of 3D printed plastic, and supported by a central guide that bisected the wing. Additionally, acrylic side-guides were used to assist and support the slat and flap. Because these guides were placed on both sides of the wing near the walls, wall effects would likely overshadow any negative aerodynamic effects created by the guides. These guides provided the proper deployment and retraction paths as well. Unlike previous experimental work on the SMA SCF, the slat in this work was made of solid machined steel, instead of 3D-printed ABS plastic [5]. This increased overall stiffness, which improved aerodynamic, structural, and aeroacoustic results. The slat and flap were each controlled by three Firgelli L12 linear actuators located at each end of the wing as well as the center. These actuators were powered by an external power supply and controlled via LabView. Given that the slat and flap traversed a known path directed by the guides, calibrations were created to correlate input voltages to important slat and flap positions. More specifically, a linear equation between the voltage required to fully deploy the high lift devices and the voltage required to fully retract those devices was calculated and used to obtain voltages that correspond to all intermediate deployment levels as well. Figure 2.2 depicts the scale model CRM wing treated with an SMA SCF installed in the wind tunnel.

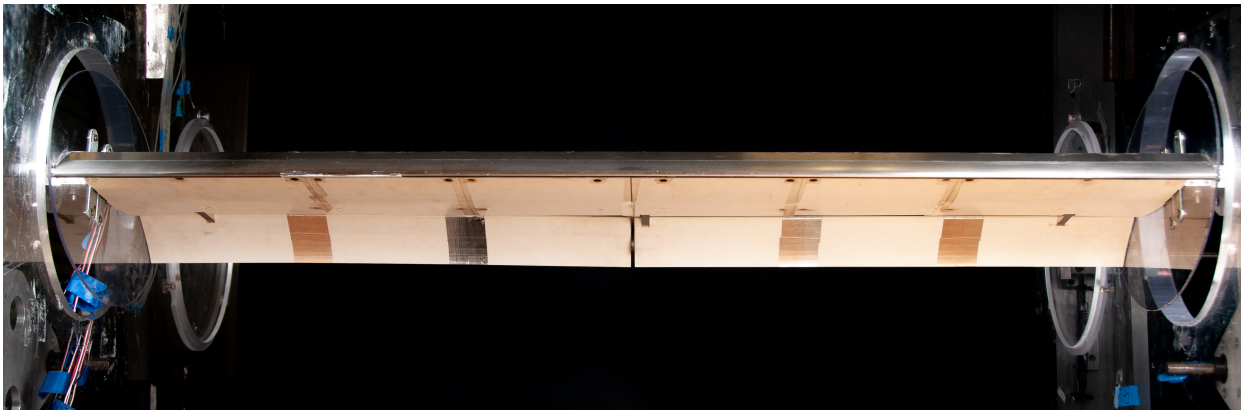

Figure 2.2: Experimental setup of CRM wing treated with SMA SCF.

2.1.1 Construction of the SMA-Based Slat Cove Filler

To form the SMA sheets (equiatomic NiTi) into the shape of the SCF, heat-treating was needed. The SCF was geometrically configured by placing the 0.002 inch thick sheets between two steel molds, and placing the molds in a 600 °C (1112 °F) oven for 30 minutes, followed by a water quench. The mold is depicted below in Figure 2.3. When multiple molds were needed for one length of SMA, the top and bottom molds were offset to avoid large gaps in the strong thermal mass provided by the molds. As a result, the division between the top molds can be seen to be staggered from the division between the bottom molds. This technique minimized inconsistent heating as much as possible.

Figure 2.3: Steel mold used to geometrically configure the SMA SCF.

Once the shape had been set, individual SMA pieces had to be secured on the slat. Fastening via chemical bonding was determined to be the best route, as mechanical fastening would impact other

aspects of the testing process (impeding flow, acting as a source of noise, etc). For this process, the SMA surface was prepared to increase bonding strength. The exterior was first roughened using sanding pads, which removed the oxide layer and prepared the bonding area. Using a technique developed by Boeing [30], a sol-gel pre-treatment was applied to the bonding area of the SMA. This sol-gel solution promotes the production of a hybrid inorganic/organic compound gradient from the metallic SMA surface to the organic bonding agent (in this case, J.B. Weld). This coating, which is applied as a liquid but after a heat treatment turns to a gel, increases adhesion by adding covalent bonds to the surface of the Ni-Ti SMA. This in turn increased bond strength.

Once sol-gel had been applied to the SCF, the slat itself was prepared for bonding. At the cove leading edge, a hinge was formed using aluminum tape. This hinge enabled the snap-in and snap-out of the SCF when it was entering and leaving the stowed configuration. Because of the scale of the model, tape was used as the hinge in place of ordinary mechanical hinge materials. At the trailing edge of the slat, the aluminum was roughened using sand paper, again to remove any oxide layer and assist in adhesion. Finally, J.B. Weld was applied to the SCF, slat trailing edge, and hinge, and allowed to cure for 24 hours. The final resulting treated slat is shown in Figure 2.4.

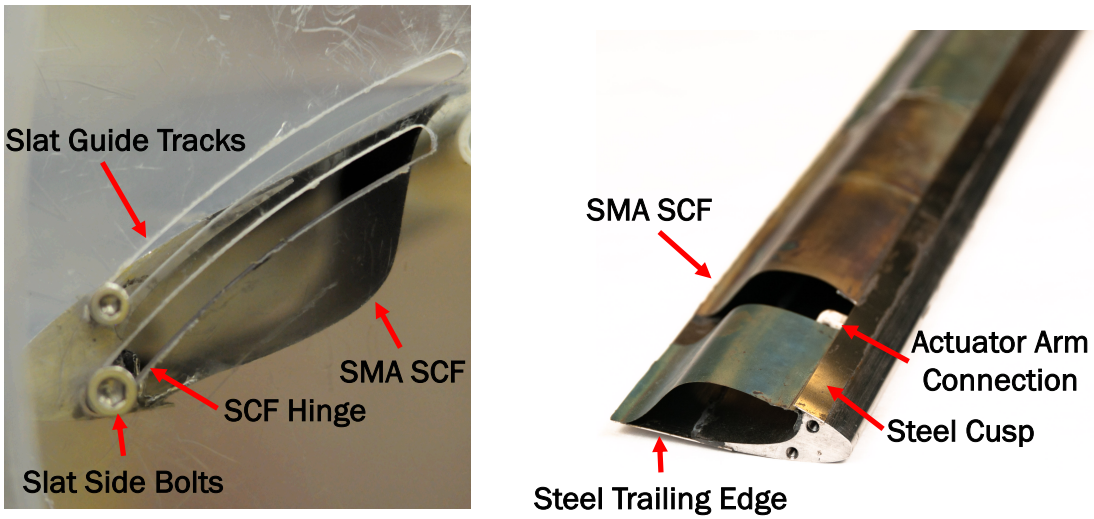

(a) Profile of SMA-Based SCF (b) View of Treated Slat

Figure 2.4: Slat with attached SCF on plastic guides (adapted from Leaton, 2020 [35]).

For thoroughness, a test was created to examine the effects of possible SCF manufacturing defects. Individually producing 4 ft of SMA SCF with identical geometry is likely impossible, therefore, an ideal SCF was 3D printed and sanded to a smooth surface before attaching it to the steel slat. The 3D printed SCF is depicted in Figure 2.5. Acoustic and aerodynamic tests were completed using the 3D printed SCF, and the results were compared to both SMA SCF and the untreated model. These tests took place after SMA-based SCF testing had been completed.

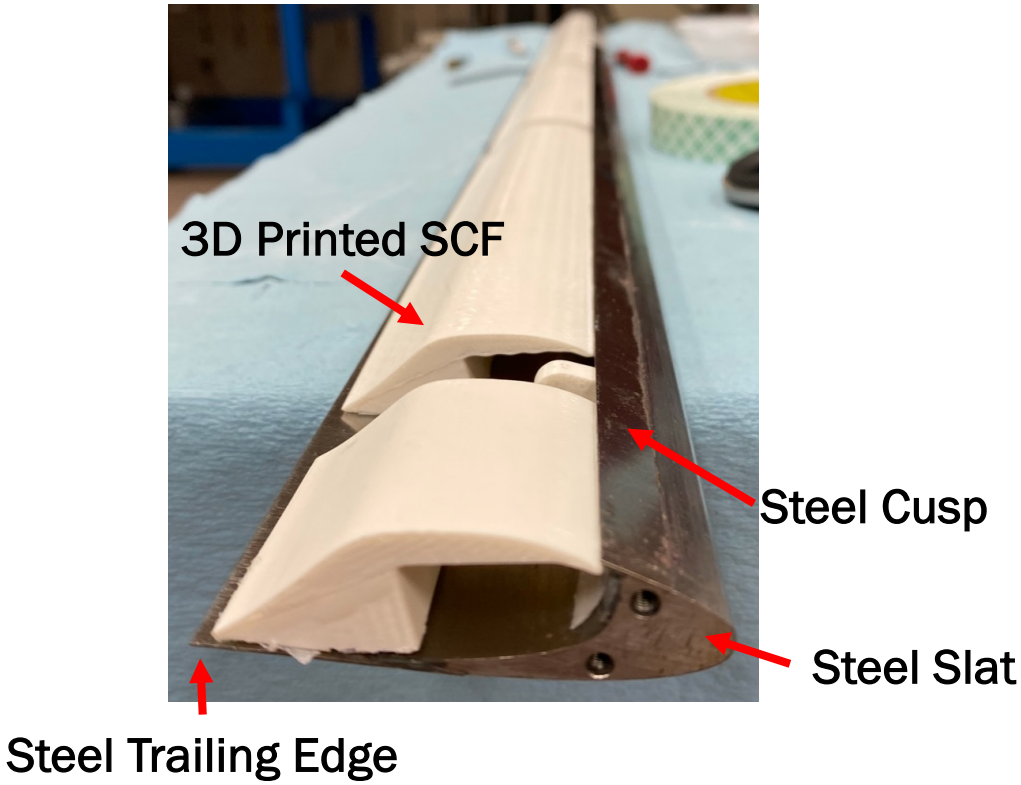

Figure 2.5: 3D Printed SCF.

3. EXPERIMENTAL AERODYNAMIC TESTING METHODS AND RESULTS

3.1 Aerodynamic Setup

[1] All aerodynamic and structural data was collected in the aerodynamic test section at the Texas A&M University H.R.B. Bright building low speed wind tunnel. The tunnel was powered by a constant pitch, variable RPM fan (depicted in Figure 3.1 and Figure 3.2), reaching a maximum velocity of around 50 m/s at the test section.

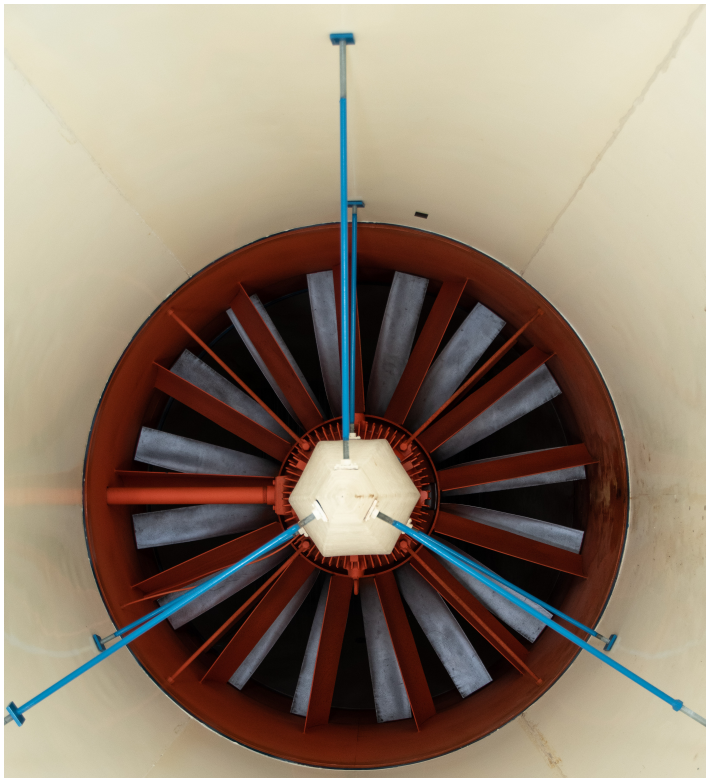

Figure 3.1: Texas A&M University wind tunnel fan.

[1]This chapter has content from [35]; reprinted by permission of the American Institute of Aeronautics and Astronautics, Inc.

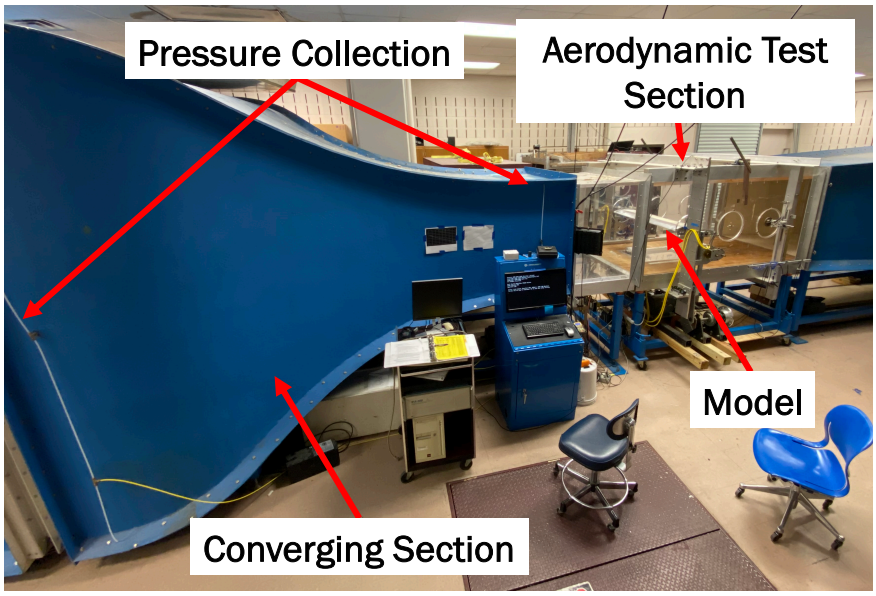

Figure 3.2: Texas A&M University 3 ft x 4 ft wind tunnel.

Velocity at the test section was measured by a differential pressure transducer. Static pressure ports were located at the converging portion of the wind tunnel, upstream of the test section. With knowledge of the static pressure difference, the velocity was obtained using a combination of Bernoulli's equation and the one-dimensional continuity equation assuming constant density.

$$p_1 - p_2 = \frac{1}{2}\rho(V_2^2 - V_1^2) \tag{3.1}$$

$$A_1 V_1 = A_2 V_2 \tag{3.2}$$

With knowledge of the pressure difference ($p_1 - p_2$), density (ρ), and area difference (A_1, A_2), the velocity both before and after the contracting section was found. The aerodynamic test section had a 3 ft x 4 ft cross section, and was 8 ft in length. The vertical walls and ceiling were made from 1.25 in thick Lexan plastic, and used to contain flow within the section. The floor was 1.5 in thick plywood, with a rectangular cutout directly underneath the wing. This cutout was fitted with a 0.1 in thick clear plexiglass window, referred to herein as the optical window. Cameras placed beneath the section were able to obtain structural information of the SCF through this

optical window. Finally, for all aerodynamic tests, the side bolts depicted in Figure 2.4 were tightened during all testing. This was done in response to slat deflection being discovered when under aerodynamic loading, and allowed the slat to stay in the exact deployment position initially specified.

For aerodynamic data collection, the CRM wing was mounted on two ATI Delta F/T load cells, which measured forces and moments in three directions ($F_X, F_Y, F_Z, M_X, M_Y, M_Z$). The data collected in these three directions from each load cell was combined to produce overall forces and moments. These features are depicted in Figure 3.3 and Figure 3.5.

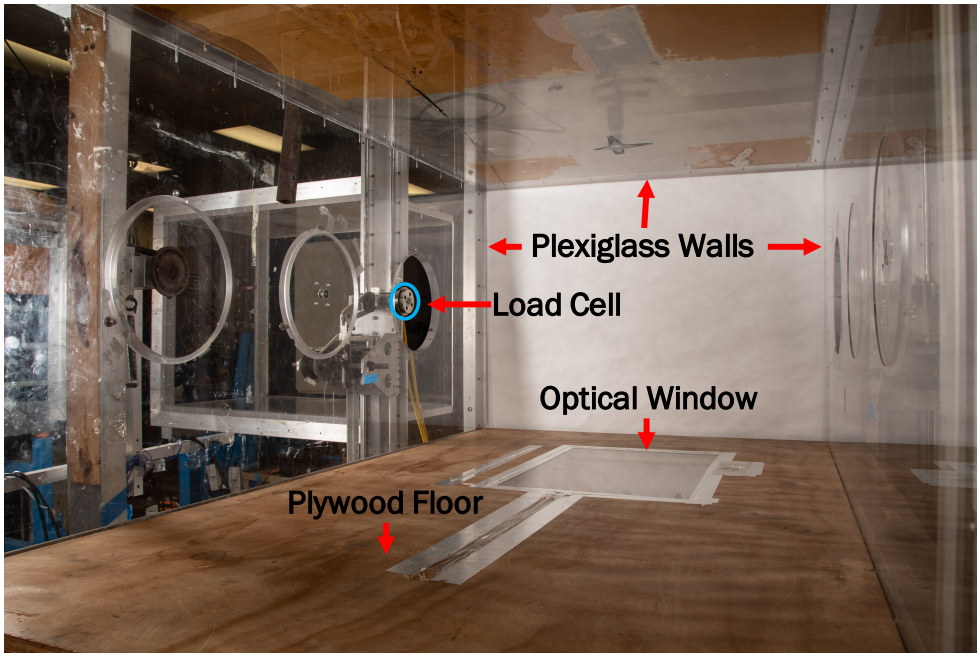

Figure 3.3: 3 ft x 4 ft aerodynamic test section (adapted from Leaton, 2020 [35]).

Aerodynamic measurements such as lift, drag, and their respective coefficients, were calculated by comparing load cell readings between tests with and without flow. Tests in which no flow was present were referred to as inertial tests. The equations to calculate these quantities experimentally

are shown below.

$$F_{Lift} = -(F_{W,X} - F_{G,X})\sin\alpha + (F_{W,Y} - F_{G,Y})\cos\alpha \tag{3.3}$$

$$F_{Drag} = (F_{W,X} - F_{G,X})\cos\alpha + (F_{W,Y} - F_{G,Y})\sin\alpha \tag{3.4}$$

$$C_L = \frac{F_{Llift}}{0.5\rho U^2 S} \tag{3.5}$$

$$C_D = \frac{F_{Drag}}{0.5\rho U^2 S} \tag{3.6}$$

where $F_{W,X}$ and $F_{G,X}$ describe the summed force from both load cells (-($F_{port} + F_{starboard}$)) in the local X direction under flow and solely under gravity, respectively. $F_{W,Y}$ and $F_{G,Y}$ describe the summed force from both load cells ($-F_{port} + F_{starboard}$) in the local Y direction under flow and solely under gravity, respectively, and α is the angle of attack. For additional clarity, S is the planform area of the retracted wing, U is the freestream flow velocity, and ρ is the flow density. C_L and C_D are non-dimensionalized descriptions of lift and drag with respect to airfoil geometry and dynamic pressure. The local coordinate systems are depicted in Figure 3.5. It is important to note that the retracted airfoil was pitched 1.48° down relative to the internal structure. Therefore, this value had to be added to the measured angle to obtain the correct angle of attack. To zero the wing, a Lucas AngleStar Digital Protractor was stationed on the starboard side of the external wing structure, and the wing was pitched until the protractor returned a 0.00° value, indicating the structure was level. Once this was true, the LabView code used for recording data automatically included the -1.48° airfoil pitch angle and updated the overall measured angle of attack.

In addition to load cells, pressure data was collected over the chord of the CRM wing using a 64 port Scanivalve MPS4264 Miniature Pressure Scanner (depicted in Figure 3.4), though only 15 ports were used for testing. These ports were centrally located on the wing to avoid the interference of wall effects. The ports were only located on the main wing as the slat was made of solid steel, so pressure lines could not be machined, and the geometry of the flap was too thin to include any lines. Such problems are inherent in many scale model experiments. Though the settings could be

changed, for all testing shown, the pressure transducer measured 100 gauge pressure samples in Pa over a 20 second period, then these values were time-averaged.

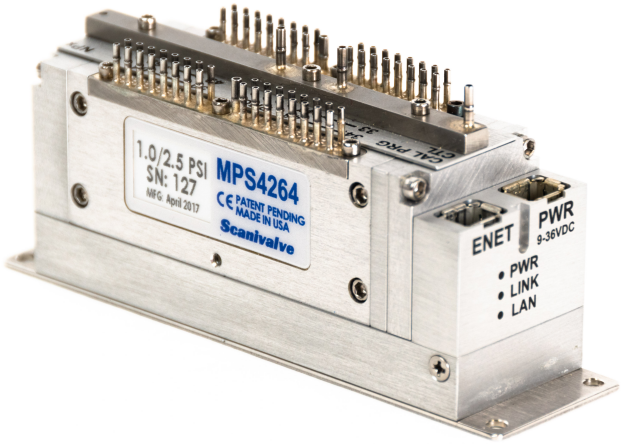

Figure 3.4: 64 port pressure transducer used in experimental testing.

Using the pressure reading at each station down the length of the main wing (P) and comparing them to the free stream static pressure (P_∞), coefficient of pressure was calculated, via Eq. (3.7).

$$C_P = \frac{P - P_\infty}{0.5\rho U^2} \tag{3.7}$$

By calculating C_P at all 15 locations, a general pressure distribution was achieved. The location of the 15 pressure ports, as well as the orientation of both load cells, is depicted below in Figure 3.5 and Figure 3.6.

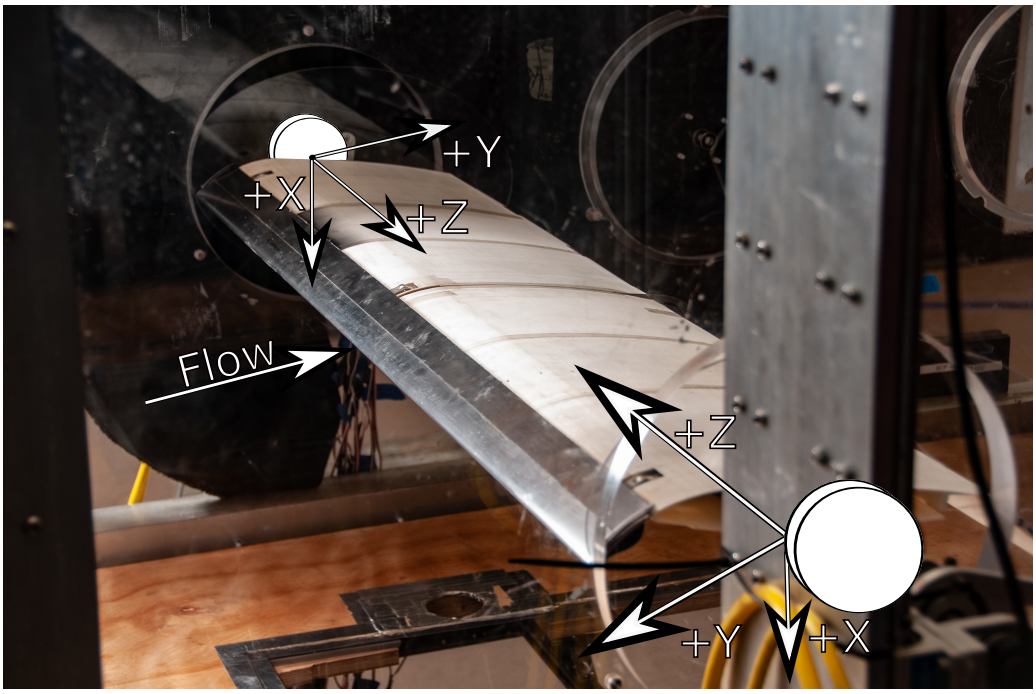

Figure 3.5: Load data collection method (adapted from Leaton, 2020 [35]).

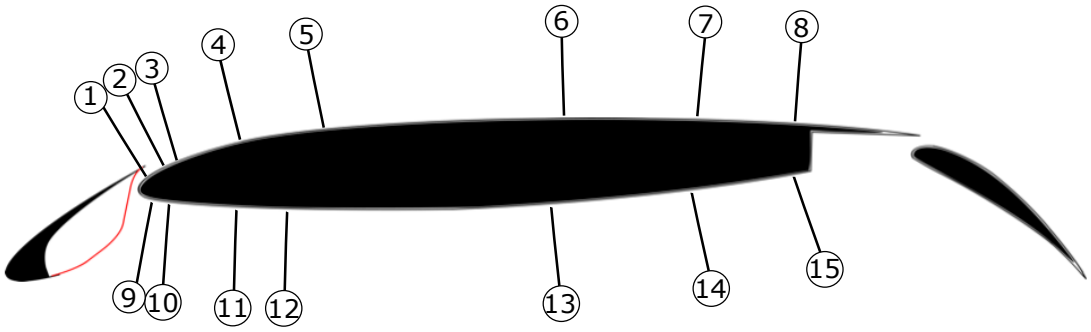

Figure 3.6: Pressure data collection ports (SCF highlighted in red) (adapted from Leaton, 2020 [35]).

Due to the additional volume of the SMA SCF and hinge in the slat cove, full retraction was not possible. In simulations, though, full retractions was achieved, leaving the possibility that the hinge or SCF geometry itself deviated from the desired performance. Additionally, consideration

was paid to the actuators, which may have been able to fully retract the slat, with a high likelihood of the motors being overtaxed. In full scale production, the actuators driving the motion of high lift devices is certainly more capable than the linear actuators used in this study. Therefore, the lowest deployment level attained for all tests was 5%. As a result, 5% deployment for both treated and untreated tests was considered fully retracted.

The experimental test matrix had several parameters that had to be carefully controlled. First, angles of attack between -2 and 12 degrees were tested. At fully deployed and fully retracted positions, where the effects of the SCF would be the most prevalent, the angle of attack was sampled every half degree. For all other deployment levels, data was only sampled at full degree increments across the listed angle span. For slat/flap deployment levels, data was collected at 10% increments, with the exception of the fully retracted position, which was at 5% deployed. Finally, multiple velocities were considered for this work as well. The range of velocities was based on the limitations of the Texas A&M University wind tunnel as well as the CRM model itself. The chosen velocities were 15, 20, 25, and 30 m/s. Below 15 m/s, the tunnel produced a significant amount of velocity variation, and above 30 m/s, the aerodynamic loading on the model was sufficient to degrade the structure. At several locations, especially combining high deployment level, high angle of attack, and high velocity, flow around the wing would separate and cause a pitching instability. In those select cases, data was not taken, as the dynamic nature of that position would have corrupted the steady-state test. Lastly, all tests displayed repeatable results, as additional trials were completed and matched closely with the original data collected. For more on error analysis of aerodynamic results, view appendix A.

3.2 Aerodynamic Results

Once pressure and load data was collected, the results were analyzed. Coefficient of pressure plots were produced using a MATLAB script. The data showed good agreement between the treated and untreated configuration, a sample of which is depicted in Figure 3.7. While the majority of coefficient of pressure data, especially past x/c=0.2, indicated little change in pressure distribution over the chord of the wing, the suction peak in some tests differed when comparing

treated and untreated. This difference was understandable, and can likely be attributed to minute changes to deployment level, overall configuration, and flow setting between tests. Additionally, a secondary effect may have been friction between the flow and SCF, causing local decreases in velocity, which in turn, increases pressure. An increase in pressure would correspond with a less negative C_P than the untreated case. When examining Appendix A (Figure A.3), the ports at the leading edge of the wing consistently had 2-3 times the error of the following ports, which certainly played a role. Minimal pressure inconsistency between configurations is preferable, as it would eliminate the need to change flight software and personnel training if the SCF were to be put into full scale production. Previous work showed minimal variation for C_P and C_L between treated and untreated configurations [31] as well, validating the results given in this work. This work is adding to that body of information but expanding it to include changes in material, deployment levels, and metrologies.

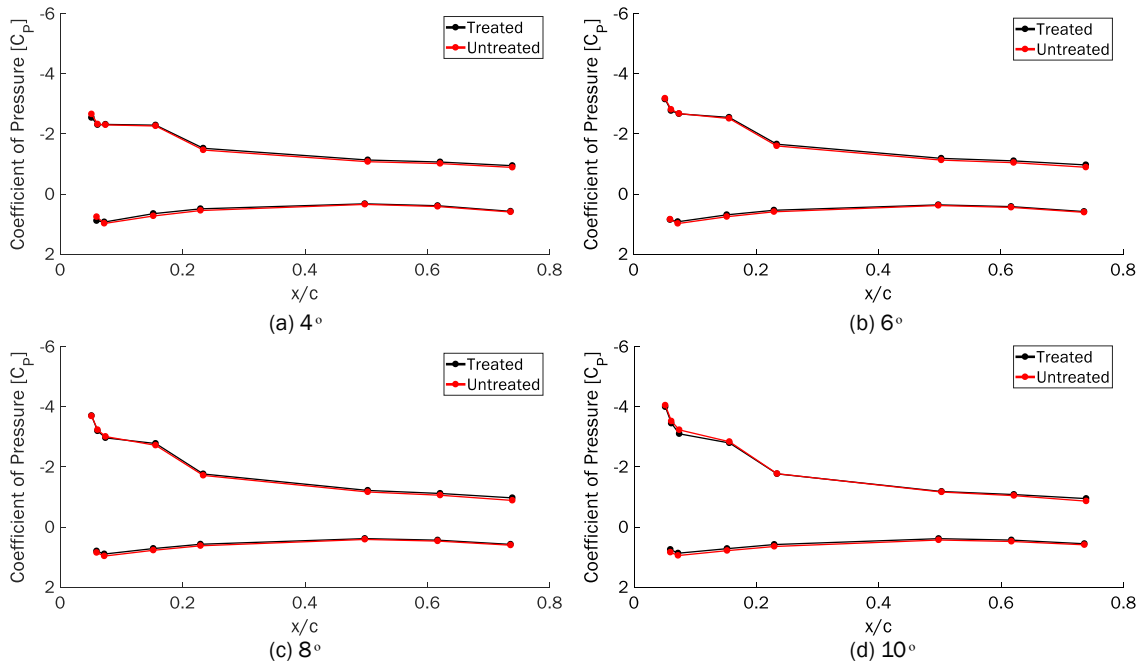

Figure 3.7: Pressure distribution comparison at 100% deployed and 30 m/s.

When comparing the treated and untreated configurations at various deployment levels, significant pressure distribution discrepancies emerged, as depicted in Figure 3.8. The SCF was not expected to closely match data from an untreated wing when not fully deployed, so this result was not unexpected. For subplots containing the label "R-D" refer to the SCF being in a stowed configuration, indicating that on that particular test, the slat was fully retracted first, then deployed to the steady-state position. Large differences were also expected between treated configurations when the SCF was stowed as opposed to deployed, as the differing geometry of the cove filler changed the aerodynamics around the wing. Figure 3.8 demonstrates that the pressure distribution comparison between treated and untreated was highly dependent on deployment level, and possibly less so on angle of attack, as depicted in Figure 3.7.

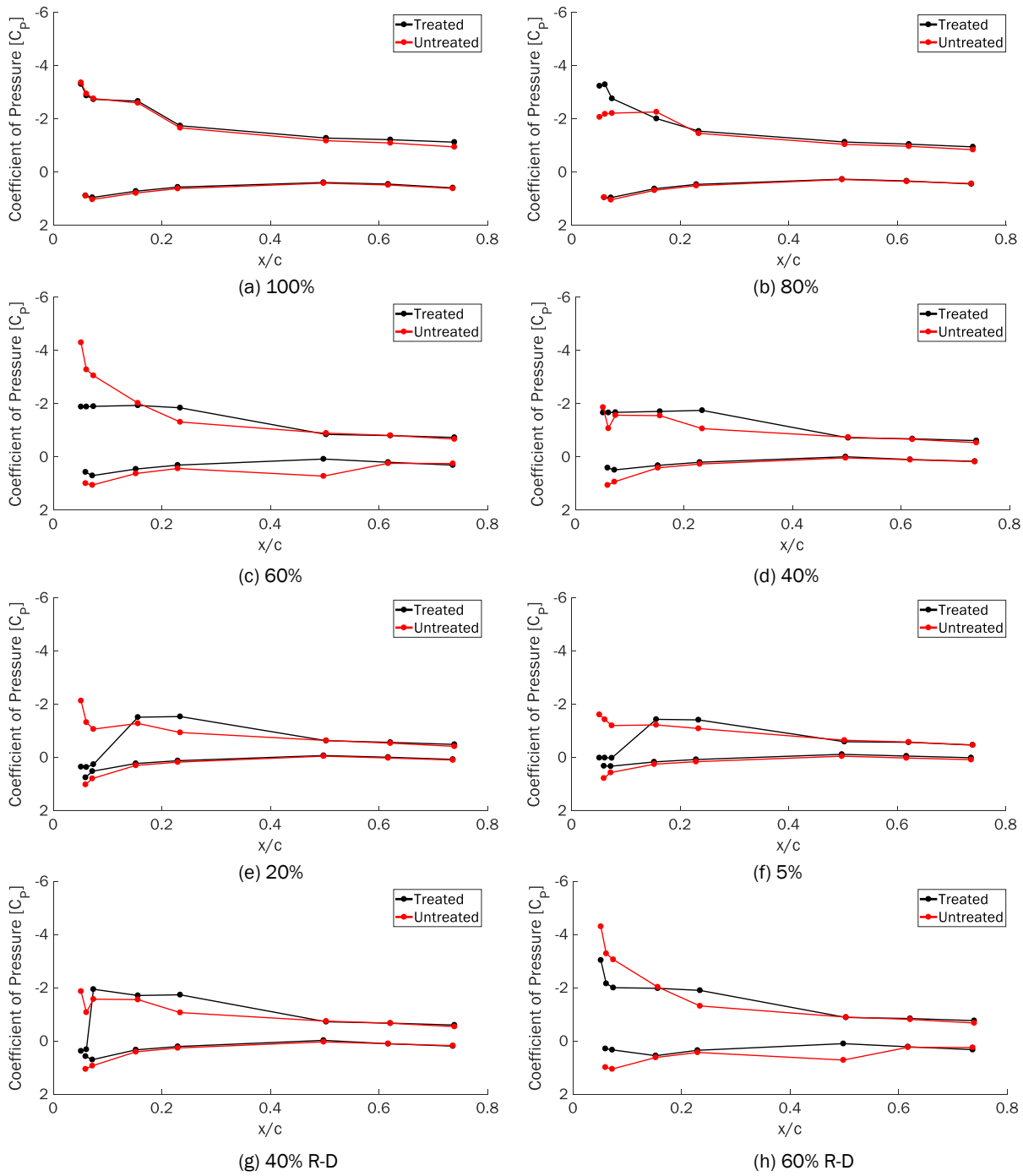

Figure 3.8: Pressure distribution comparison at 6°, 25 m/s across many deployment levels. R-D, used in (g) and (h), refer to the SCF being in a stowed configuration during those tests.

When processing load data, a modified MATLAB script was used to calculate C_L, C_D. When

comparing coefficient of lift and coefficient of drag over the range of tested angles of attack, as depicted in Figure 3.9, the treated configuration generated slightly higher C_L and C_D, until around 7 degrees, when the untreated configuration generates more lift. For reference, previous experimental SMA-based SCF work [20] demonstrated lower levels of drag than the current work. One of the reasons for this discrepancy could be that, in previous work, the SMA SCF was 50% thicker than in the current work. For that reason, much smaller deflections would occur as a result of aerodynamic loading. With a thinner SCF, large deflection could have contributed to increased flow instability and therefore, increases in drag around the SCF. For the majority of angles of attack, excluding -2 degrees, the C_L for both configurations was very similar. A possible cause of the significant drop in lift at -2 degrees was flow separation, which could be promoted by slat cove circulation. This manifested itself experimentally in wing instability, shaking the wing violently during testing. However, at all angles of attack above -2 degrees at 15 m/s, this instability dissipated. When flow speed was increased, instability would appear at higher angles of attack (up to about -0.5 degrees at 30 m/s). Recall that the purpose of the SCF was to reduce noise production while minimally impacting aerodynamic performance, which pressure data appeared to validate aerodynamically. Figure 3.9 and Figure 3.7 both indicate that for the majority of the tested flight envelope, the treated and untreated configurations produced similar results.

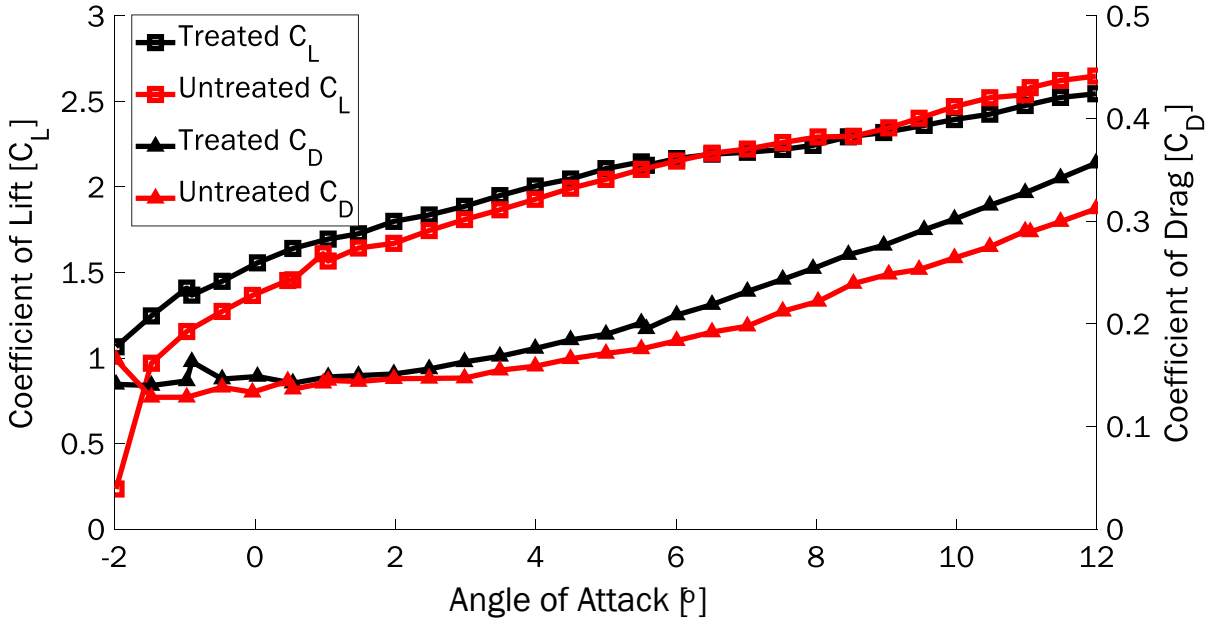

Figure 3.9: Coefficient of Lift and Drag for treated and untreated configurations at 100% deployed and 15 m/s.

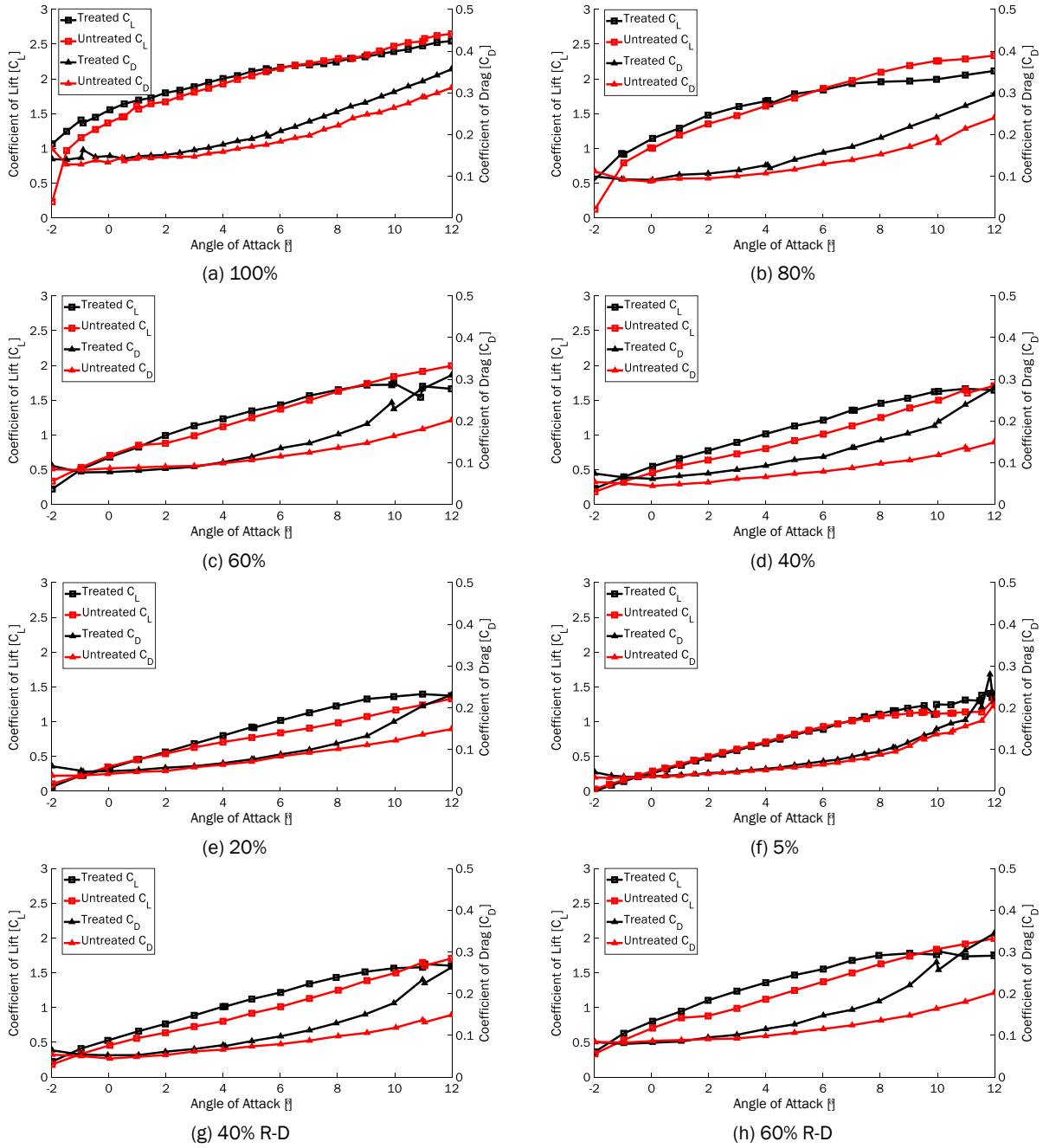

Figure 3.10: Coefficient of Lift for treated and untreated configurations at many deployment levels and 15 m/s.

Figure 3.10 depicts the change in lift coefficient as deployment level changed. As expected, in all cases, as high lift devices were retracted, coefficient of lift decreased as well. The comparative trend between treated and untreated appears to be consistent throughout the range of deployments.

At low angles, both treated and untreated had similar coefficients of lift and drag, with the treated case consistently generating more of each. However, especially when deployment percentage was closer to fully deployed (i.e., 100%, 80%, 60%), a drop in lift was detected at higher angles of attack, whereas the untreated case remains approximately linear. The SCF was designed for nominal landing angles, therefore the lift generated by the treated configuration likely suffered more than the untreated case. Additionally, the interaction between the flow through the gap between the SCF and wing leading edge and the flow around the airfoil may have caused early separation, reducing the amount of lift. The trends displayed in Figure 3.10 were true for all velocities tested. Additionally, similar to how the pressure distribution varied between the treated and untreated case in Figure 3.8 when the SCF was stowed, the coefficient of lift and drag displayed the same trend. However, when examining the lift and drag coefficient, but focusing on how the treated case changed when the SCF was stowed (R-D) and deployed (nominal), very few differences were found. Therefore, it seems that in terms of lift and drag, the shape of the SCF at a given deployment setting may have played a smaller role than originally thought.

Comparing Figure 3.9 to Figure 3.7, the results appear contradictory. For instance, at 4°, the treated and untreated coefficient of pressures appeared to be nearly identical, but the coefficients of lift and drag had noticeable differences. To investigate this further, a rough conversion between the two metrics was calculated. While at 0°, coefficient of lift was calculated from the coefficient of pressure data using Eq. (3.8).

$$C_L = \int_0^1 C_{P,l}(x) - C_{P,u}(x)\,\mathrm{d}x \tag{3.8}$$

where x was normalized by chord (effectively x/c) and $C_{P,l}$ and $C_{P,u}(x)$ refer to the pressure coefficient of the lower surface and upper surfaces, respectively. Numerically, this computation was completed using MATLAB's "trapz()" function, which utilized a trapezoidal integration scheme because of the scarcity of data in each C_P plot. This calculated coefficient of lift was referred to as the approximate lift coefficient, whereas the lift coefficient recorded by the load cells was

referred to as the measured lift coefficient. While the magnitude of the approximate lift coefficient differed from the measured, the difference between the treated and untreated was nearly identical. The approximate calculated 0.13 more lift coefficient from the treated configuration, whereas the measured coefficient displayed 0.15. This "ΔC_L" was a more important metric, as pressure coefficient wasn't influenced by wall effects, additional flow from the high lift devices, etc, and was only measured in a small central chord of the wing, therefore the approximated magnitude wasn't likely to match the measured value. Therefore, the agreement between the ΔC_L values demonstrated that, while Figure 3.9 and Figure 3.7 may appear to demonstrate differing behavior, the underlying data was in agreement.

The effect of various variables (velocity, deployment level, configuration, and angle of attack) on coefficient of lift and drag was depicted in Figure 3.11. This image depicts that angle of attack and deployment level both heavily impacted aerodynamic performance, whereas velocity and, most importantly, configuration (whether the slat was treated or untreated) had very little impact. This confirmed the notion that the inclusion of the SCF minimally impacted aerodynamics, and validates the aerodynamic purpose of the SCF.

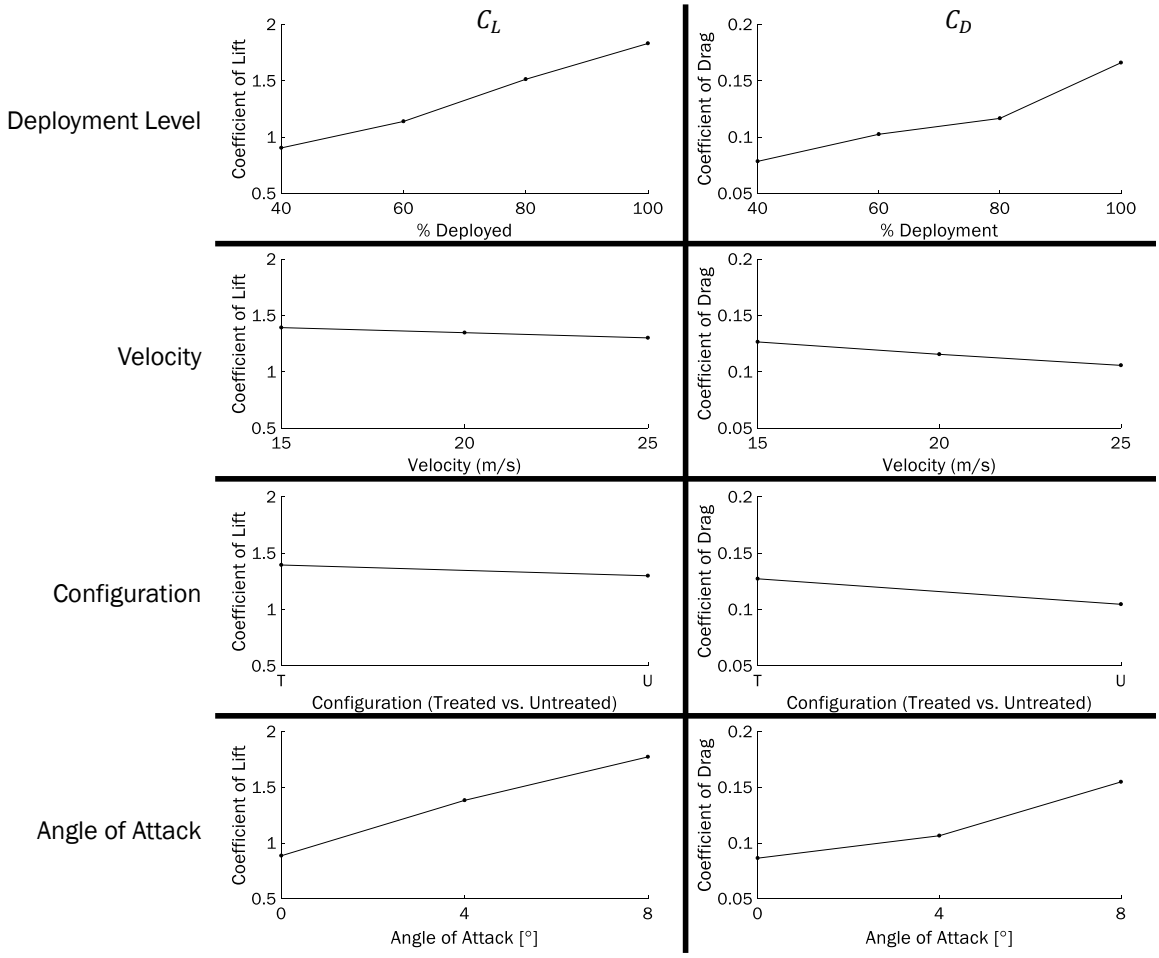

Figure 3.11: Factor effects plots for several important variables. It is clear that angle of attack and deployment level have the most significant impact on coefficient of lift and drag, whereas the addition of the SCF had very little effect.

Another measure of aircraft performance is the relationship between lift and drag forces, calculated as L/D, and depicted in Figure 3.12. Both treated and untreated configurations have maximum L/D between 2 and 4 degrees, with diminishing values on either side. In previous work [20], larger negative gradients existed both preceding and following the maxima around 2 degrees. While the test setup in Patterson's work was similar, the discrepancy was likely caused by the the use of a flexible 3D-printed slat in the past. The current work utilized a machined stainless steel slat, which deformed less under similar aerodynamic loading, and thus, likely exhibit fewer large gradients in experimental data.

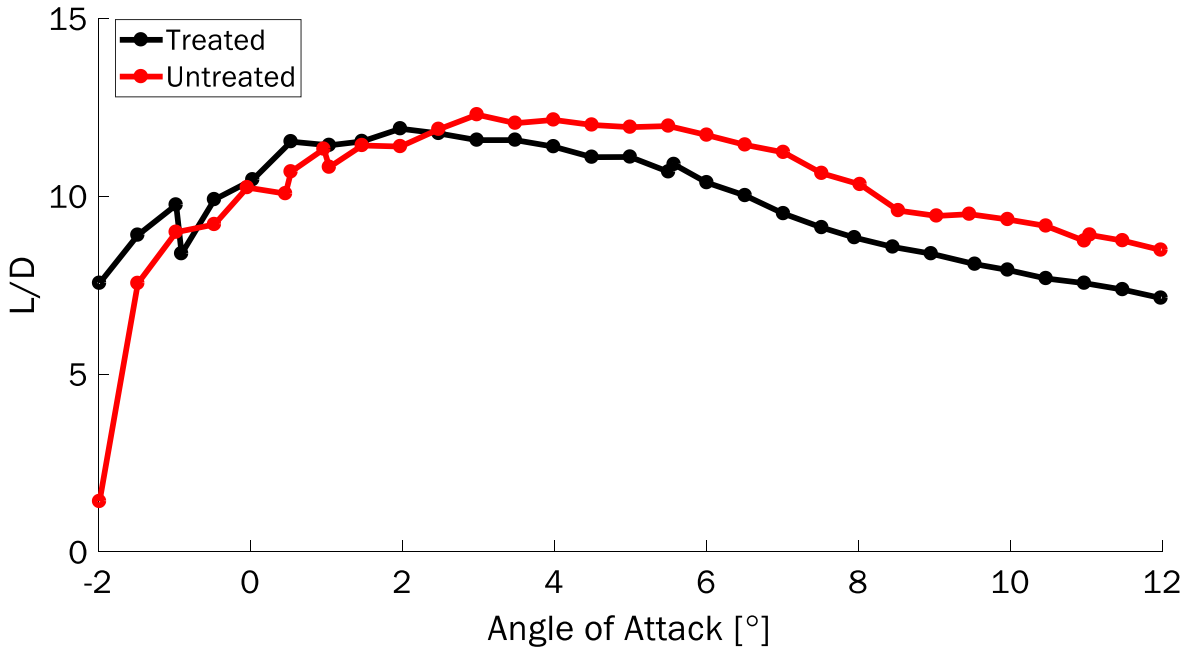

Figure 3.12: L/D for all tested angles of attack at 100% deployed and 15 m/s flow velocity.

Finally, drag polar data was calculated as well, comparing the coefficient of lift to the coefficient of drag. Notice in Figure 3.13, a drag bucket existed (which describes a global minima for the coefficient of drag and is indicative of an efficient travel configuration). Relating the values of C_L and C_D to Figure 3.9, it was apparent that this efficient zone existed around an angle of attack of 2°, which again corresponds to the maxima of Figure 3.12 as well. Although Figure 3.12 and Figure 3.9 are at two separate flow velocities, C_L and C_D were normalized by velocity, so comparisons between the two could be made.

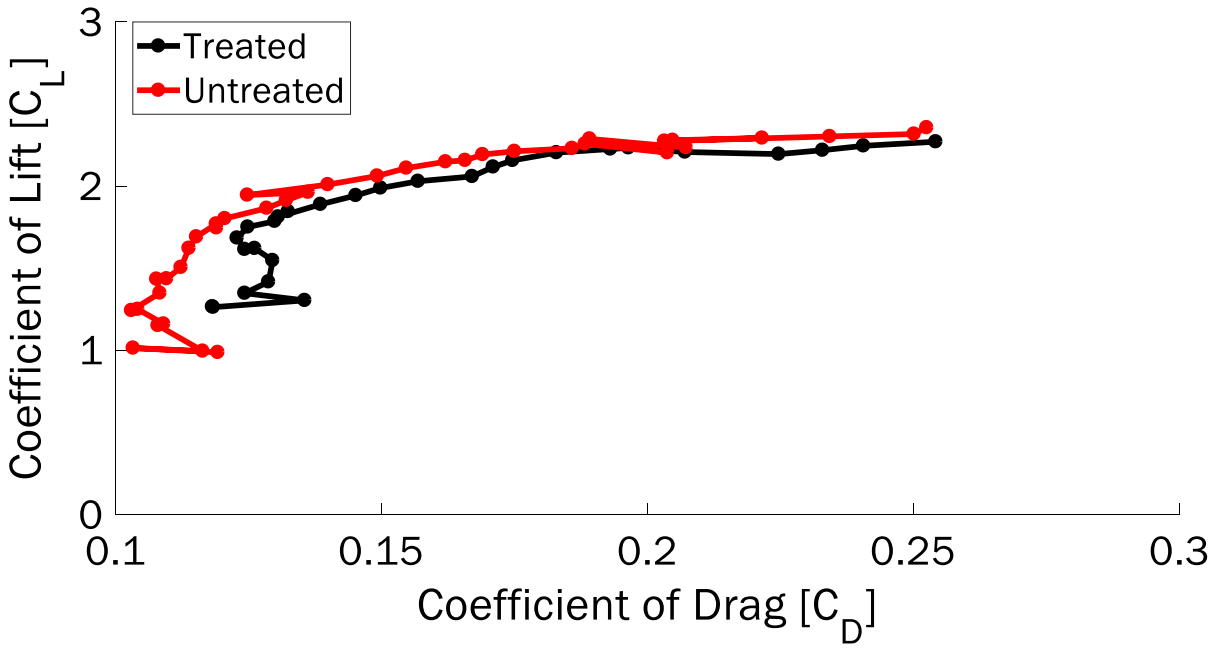

Figure 3.13: Coefficient of lift vs coefficient of drag at 100% deployed at 30 m/s flow velocity.

From an aerodynamic perspective, the data indicated a small, but not unnoticeable, variation caused by the implementation of the SCF, especially when in configurations with low lift generation. As C_L increased past 2, the two drag polars demonstrated very similar data. The SCF was theorized to cause negligible differences in aerodynamic performance, which is optimal for implementation onto full-scale aircraft. In summary, the relative performance of the SCF to an untreated wing was highly dependent on the deployment level and angle of attack. For efficiency improvements, the aircraft should trim to below 2° angle of attack. This trim is likely unattainable, however, during takeoff and landing.

Wind tunnel blockage is a pervasive issue within experimental testing. Blockage effects occur as a result of some portion of the flow being diverted from its original path due to the body of the wing, which increases local flow velocity and impacts experimental results. In general, blockage percentage should be as low as possible, typically below 10% [32]. For the aerodynamic test section, where the full 4 ft span of the wing was contained within the section, the maximum blockage percentage (achieved at 12 degrees angle of attack and 100% deployed) is approximately 13.8%.

This indicates that data taken at that particular position and deployment condition may be affected by this increase in velocity. In the aerodynamic test section, angles of attack above 7 degrees while fully deployed caused greater than 10% blockage ratio, and therefore were more prone to error.

As a measure of the impact that manufacturing defects may have had on the results obtained, a 3D-printed "ideal" SCF was created and attached to the slat. To cover the 4 ft span of the slat, several individual parts had to be printed, with identical cross section but varying span. Four 10 in, two 1.5 in, and one 1 in sections were printed. The 3D-printed SCF was first treated for smoothness with 200, 600, and 1000 grit sand paper to reduce flow disruption.

Once sanding was completed and the 3D-printed SCF was attached to the slat via double sided tape, normal 100% deployed testing was completed both in the aerodynamic and aeroacoustic test sections. The continuity of the aerodynamic surfaces was ensured using tape to cover the small gaps between 3D-printed sections. A comparison between the SMA SCF and the "ideal" 3D-printed SCF is depicted in Figure 3.14 and Figure 3.15.

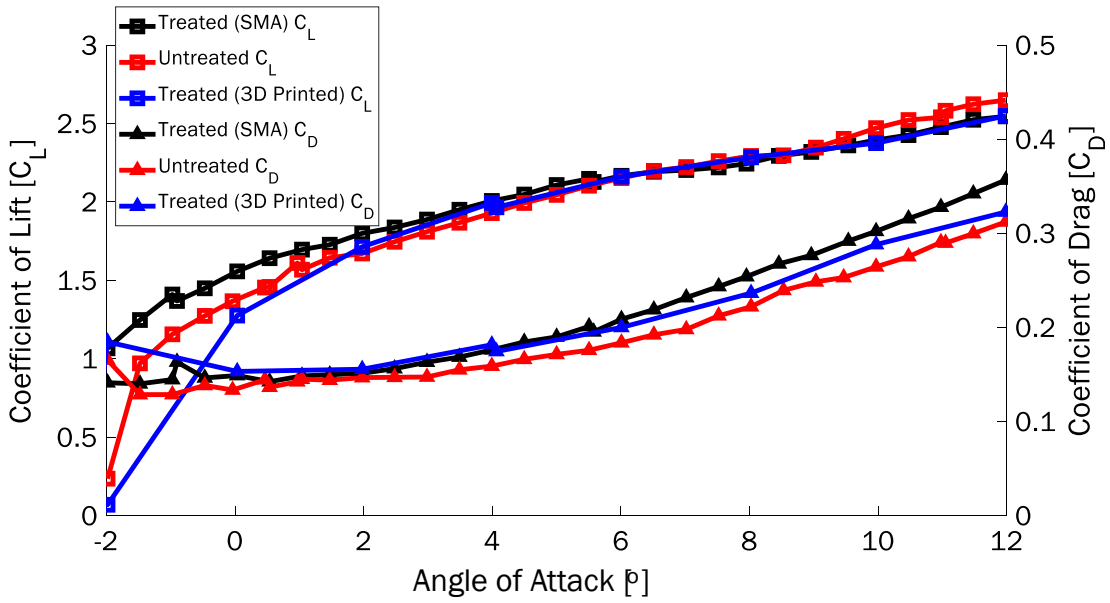

Figure 3.14: Coefficients of lift and drag vs angle of attack for untreated, SMA, and 3D-printed SCF at 100% deployed at 15 m/s flow velocity.

The coefficients of lift and drag for the 3D-printed SCF model behaved very similarly to those of the SMA SCF, except at low angles of attack. When the angle was below 2°, the behavior matched more closely with the untreated configuration. Considering the purpose of the SCF was to reduce noise generation while minimally impacting aerodynamic characteristics, this goal seems to have been achieved by the "ideal" 3D-printed case for lift and drag. As for coefficient of pressure, large variations were noted at the suction peak when compared to either the SMA SCF or untreated case. The suction peak was extremely sensitive, and this discrepancy was possibly caused by the improvements made between the shim (the steel sheet directly preceding the SCF on the lower surface of the slat) and the start of the 3D-printed SCF. Assuming flow transitioned from the shim to the SCF (and thus the leading edge of the wing) more easily, the corresponding velocity would have likely increased as well, causing a more negative suction peak. This also could be the result of the pressure ports being directly downstream of a gap between sections in the 3D-printed SCF, although this is unlikely. While this gap had smooth tape covering the discontinuity, it's possible the added thickness of the tape caused flow disruption, resulting in a change in coefficient of pressure values. During testing, it was noticed that very small changes to slat geometry yielded large variations in the suction peak (changes of greater than ± 1), therefore the peak was known to be extremely sensitive. However, given the issues with the suction peak, all ports downstream of x/c=0.2 corresponded well with the untreated configuration, as well as the entirety of the pressure side of the wing.

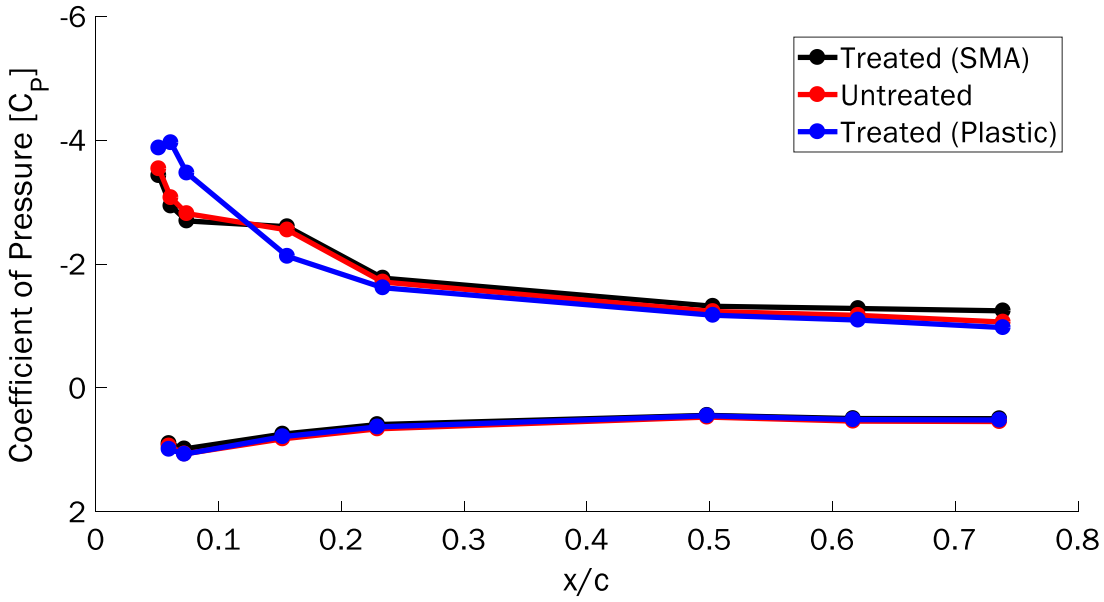

Figure 3.15: Coefficient of pressure for untreated, SMA, and 3D-printed SCF at 100% deployed, 6° angle of attack, and 15 m/s flow velocity.

4. EXPERIMENTAL STRUCTURAL TESTING METHODS AND RESULTS

4.1 Structural Setup

[1] Structural testing was completed on the SMA SCF to further understand the response under load. To obtain structural information, typical experimental extensometer systems were deemed too intrusive for use. Not only were the deflections likely too great for most systems to measure, but also their presence would likely corrupt other data, such as lift, drag, and pressure measurements. As a result, Digital Image Correlation (DIC) methods were used to non-intrusively collected deflection measurements.

The main operating principle behind digital image correlation relies on tracking dots on a test surface. In the case of a theoretical tensile test, the surface would be painted with dots, and a reference (no load) image would be taken. As load is applied and strain becomes non-zero, the dots move relative to their original unloaded position, and subsequent images are taken. By comparing the movement of the dots, local sample displacements and strains can be calculated. If 3-dimensional displacements are needed, two cameras must be used, with some prescribed angle between them (which is typically around 15°). To capture and post process images, Vic-SNAP and Vic-3D were used respectively, both made by Correlated Solutions.

In the case of the SMA SCF, two cameras were placed beneath the aerodynamic test section. Both viewed the SCF through the optical window, and exceeded the minimum angular distance between the two cameras. The 2.3 MP Point Grey DIC cameras with NIKKOR 60 mm macro lenses had 50 ms exposure times, to reduce the possibility of motion blur. Additionally, an LED light source was placed between the cameras, and pointed towards the SCF. During testing to find the minimum acceptable shutter time, it was noted that DIC results became extremely unrepeatable when using an exposure time less than 50 ms. It was theorized that the refresh rate of the light source was greater than the camera exposure time. Therefore, the camera likely collected differ-

[1] This chapter has content from [35]; reprinted by permission of the American Institute of Aeronautics and Astronautics, Inc.

ing amounts of light for each image, which reduced the repeatability between the results of any two tests. For this reason, 50 ms was chosen as it resulted in repeatable results, and reduced the possibility of motion blur. The test setup for DIC cameras is shown below in Figure 4.1.

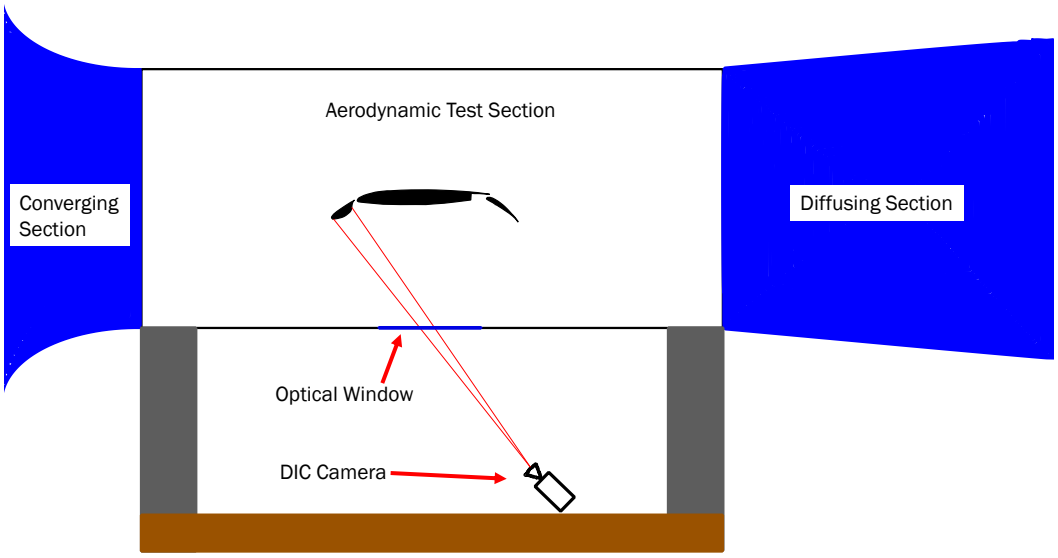

Figure 4.1: DIC camera setup.

Surface treatment was needed for the SMA SCF to enable DIC measurement. First, a layer of matte white spray paint was applied to a portion of the SCF within view of the cameras. Once the white paint had dried, black spray paint was carefully applied from a distance, so droplets formed while traveling towards the surface, and when they impacted the SCF, created individual, unique, black dots. This surface is shown in Figure 4.2, along with the materials used.

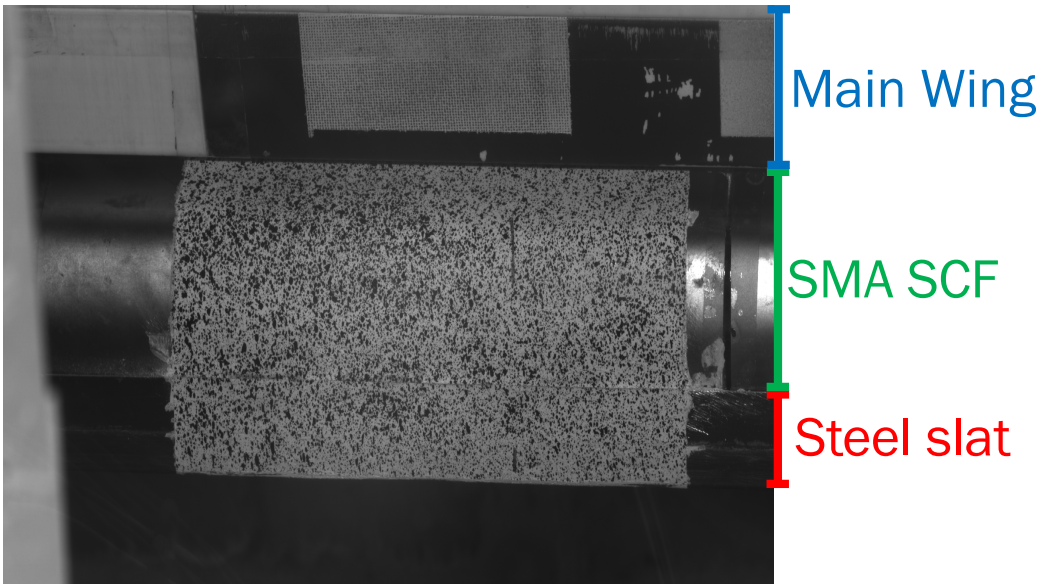

Figure 4.2: DIC speckle pattern.

To calibrate the DIC software, calibration targets were used as shown in Figure 4.3. These targets had 4 mm dots spaced across the surface, which were used for sizing calibration. 4 mm dots were chosen as they produced the least error for the given setup (lighting, distance from cameras, area coverage, lens settings, etc). First, the target was placed as close to the SCF surface as possible. Next, the target was rotated in all three axes and photographed. This rotation allowed the post-processing software to build a 3-dimensional coordinate system in the general vicinity of the area of interest. Finally, with knowledge of both sizing and a coordinate system, displacement was calculated from samples under load. Typically, between 50 and 100 calibration images are taken, and images with the best view of the calibration target are used to create a coordinate system. For the purposes of repeatability and procedure, calibration always preceded testing, though that isn't absolutely necessary.

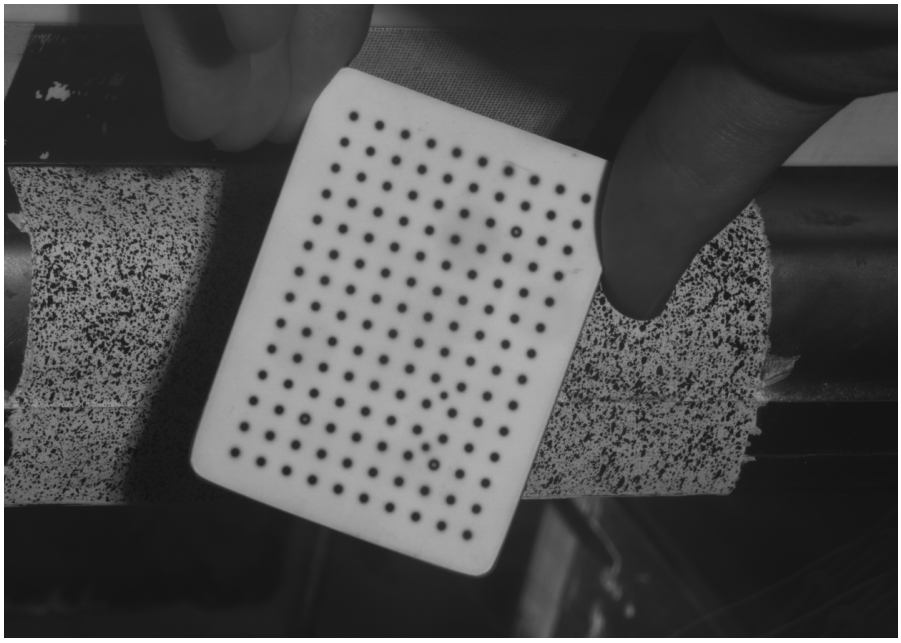

Figure 4.3: DIC calibration target.

DIC images were taken at a constant 6° angle of attack. This was done to maintain a constant distance between the camera and sample for each test, as well as keep the lighting the same. Inconsistencies in either of these areas likely would have led to additional error in the DIC-generated displacement measurements. Images were collected at 10% deployment intervals across the four flow velocities stated previously.

Once DIC images had been collected for a calibration, wind-off reference test, and wind-on test, these images were moved into Vic-3D for post processing. To begin, calibration images were loaded into the software, and depending on the ability of the cameras to create a coordinate system, a calibration score was given. The calibration score was based on projection errors for each pixel of the camera as the coordinate system was being created [33]. Typically, a score below 0.1 was acceptable. Once calibration was completed and an acceptable score was obtained, images from the wind-off and wind-on tests were loaded into the software.

4.2 Structural Results

An image from the unloaded, wind-off test was specified as the reference image, to which loaded, wind-on test images were compared. On the reference image, an area of interest was established. This area of interest contained the speckles that needed to be tracked by Vic-3D. Although a large area of interest may be specified, only speckles that are sufficiently visible and illuminated will be tracked. In the case of the SCF, the area of interest covered the entire speckled portion of the slat, from solid steel leading edge to SCF trailing edge, though the trailing edge wasn't entirely covered due to high angle of incidence with the cameras. The area of interest is highlighted in blue in Figure 4.4. Once the area of interest was specified, Vic-3D processed each image and calculated three values of displacement.

Once the images had been processed, rigid body motion was digitally removed. During the course of testing, a 1-5 mm slat deflection due to bending was noticed. This bending occurred due to aerodynamic loading, and had to be removed for proper SCF deflection to be calculated. Vic-3D included a tool for rigid body motion removal, which was applied to all wind-on data sets. An area of minimum deflection was specified, which in the case of the SCF, was the steel slat leading edge. Relative to the 0.002 in thick SMA, the slat had much less deflection under loading. The rigid body motion area selection is highlighted in red in Figure 4.4.

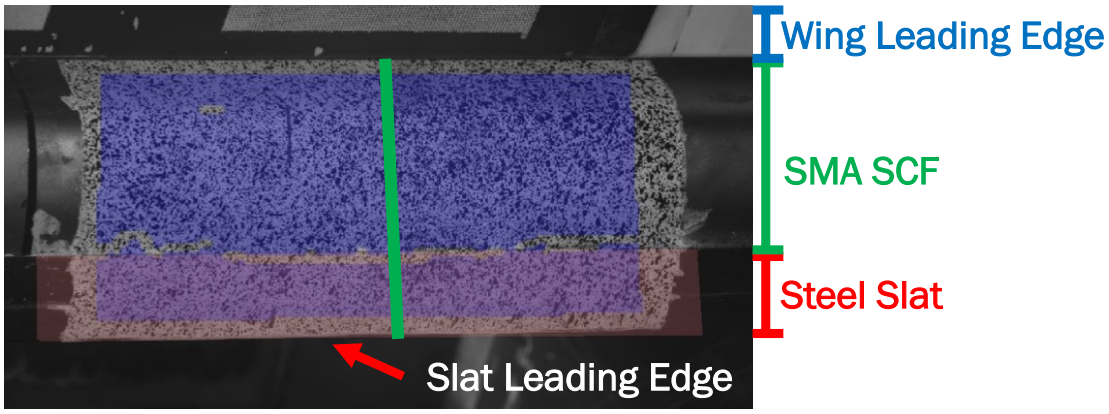

Figure 4.4: DIC area of interest and rigid body motion selection. The green line indicates the path of the shape data that was queried, the blue highlight covered the area of interest, and red shading depicted an area of minimum deflection for the rigid body motion removal tool (adapted from Leaton, 2020 [35]).

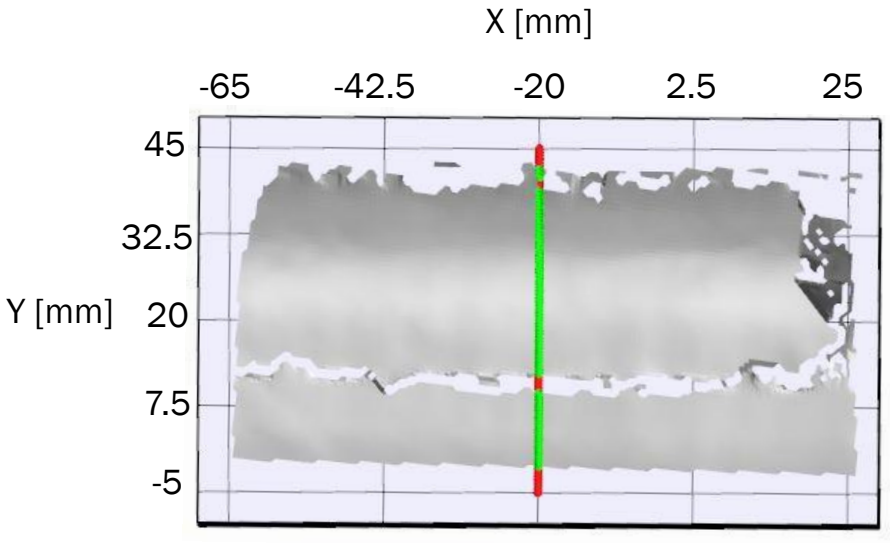

Figure 4.5: Sampled area from DIC topology. Green dots indicated that the point was able to be queried, red indicated that it was not. 100 points in all were sampled.

Once rigid body motion was removed, deflections were calculated. Specifically, surface co-

ordinates and displacements values along a specified 1-D line in the chord-wise direction were outputted (see Figure 4.5). All data was then exported as an ASCII file of comma separated values (.csv) which was post processed further through a python script. This script simply collected and standardized the coordinate systems produced by Vic-3D so all DIC data was directly comparable. Figure 4.6 depicts displacements generated by DIC for the SMA SCF in the flow-wise direction only, though displacements in all three directions were calculated. The DIC software used did not have the capability of producing displacement magnitude contours, only displacements in specific directions. Notice the relatively low displacement near the leading edge, which was made of stainless steel, and higher displacement in the center and trailing edge, which was made of SMA. Additionally, between the steel leading edge and SMA SCF is an area of no contour. Due to the geometry of the SCF, there is approximately a 0.5 mm step between the steel and SMA, which DIC could not be accurately applied to.

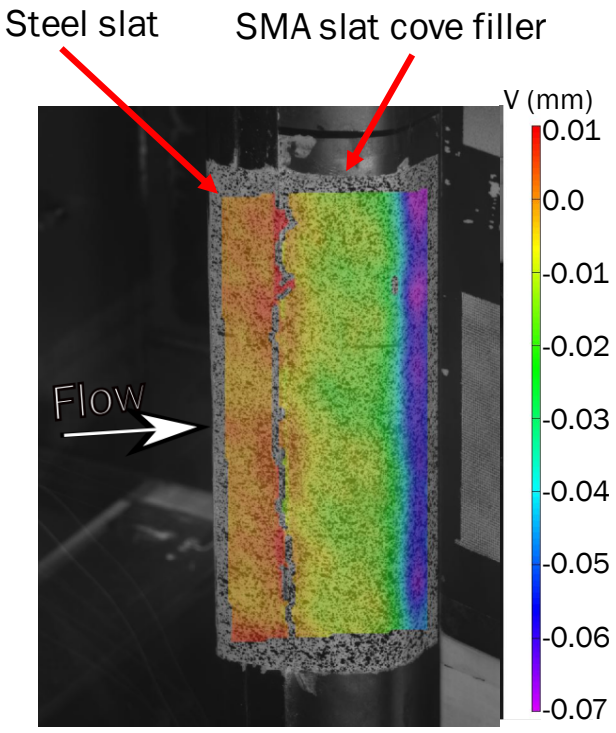

Figure 4.6: DIC displacement contour displaying the deflection in the flow-wise direction (adapted from Leaton, 2020 [35]).

As stated earlier, once the contour from Figure 4.6 is created in DIC, a single line of data in the chord-wise direction is taken and exported. In most tests, approximately 80 data points were taken along a chordwise curve from each post-processed DIC image. Each data point contained three coordinates, three displacements, and six strains. By combining the three displacements into a magnitude, Figure 4.7 was created. Recall that, when comparing Figure 4.6 to Figure 4.7, the trend differs due to the fact that the contour in Figure 4.6 could only display one of the three components of displacement.

As an example of the accuracy of the DIC process, data was overlaid on a cross-section of the slat (Figure 4.8), revealing the data to closely follow the complex shape of the SCF. As depicted in Figure 4.7, deflection increases as dynamic pressure increases, as expected. Areas with large displacements under flow correspond to the SMA area directly following the steel leading edge, and the area directly preceding the epoxied trailing edge. The deflection towards the slat appearing at around 18 mm likely drove the deflection away from the slat at around 2 mm. Again, the material change from steel to SMA at around x=0 mm was likely the cause of low deflections from 10 mm to 0 mm, and higher deflections when $\leq$0 mm. Additionally, areas of higher deflections coincide with areas of relatively low curvature. Finally, assuming pressure could be recorded on the SCF, it is possible that a negative pressure may have been present near the slat trailing edge, causing the SCF to deflect away from the slat. This pressure is dependent on angle of attack and deployment, and wasn't able to be measured experimentally.

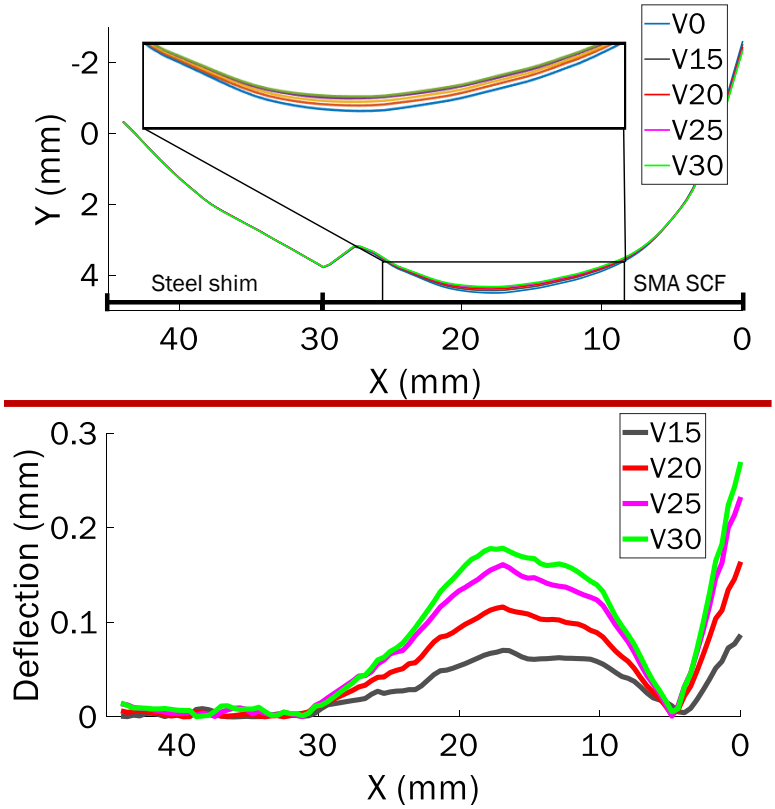

Figure 4.7: DIC generated shape and deflection data at 100% deployed.

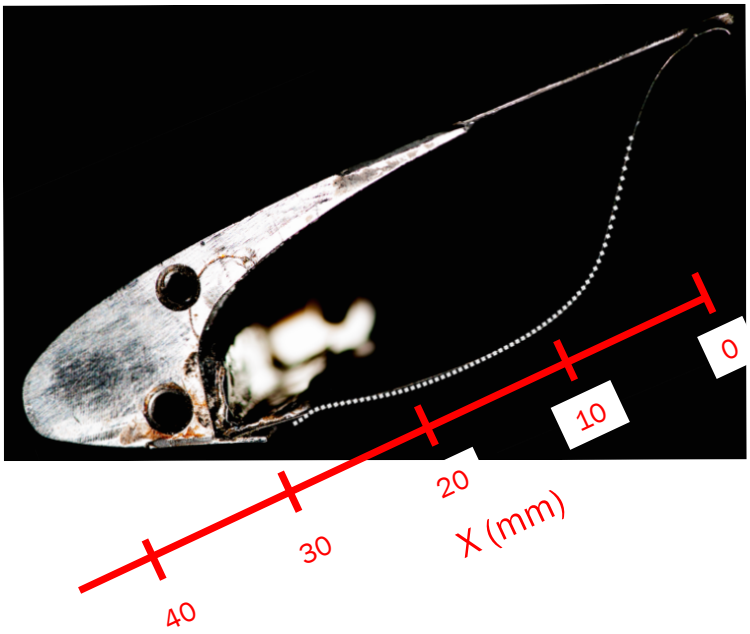

Figure 4.8: DIC generated points overlaid on SCF with approximate coordinate system (adapted from Leaton, 2020 [35]).

5. EXPERIMENTAL AEROACOUSTIC TESTING METHODS AND RESULTS

5.1 Aeroacoustic Setup

5.1.1 Design and Implementation of Aeroacoustic Section and Anechoic Chambers

[1] The most innovative contribution of this work was within the field of aeroacoustics. From an aeroacoustic perspective, it was expected that the treated (slat with bonded SCF) configuration would produce less noise than the untreated (slat without any SCF) configuration, where noise production is quantified later in Eq. (5.11) and (5.14). Using the Texas A&M University new acoustic wind tunnel test section, anechoic chambers, and microphone array, the noise produced by the CRM wing in flow was characterized. Texas A&M University is one of the few universities with an aeroacoustic wind tunnel, along with University of Bristol [27], Virginia Tech [34], and Florida State University [28]. Typically, investing in an aeroacoustic wind tunnel involves building a tunnel (usually an open-jet [28]) which cannot be used for normal aerodynamic testing. However, Texas A&M University has built interchangeable aerodynamic and aeroacoustic test sections, enabling both tests to be conducted with minimal changes. The design of the acoustic test section and anechoic chambers by the mechanical engineering senior design team is depicted in Figure 5.1.

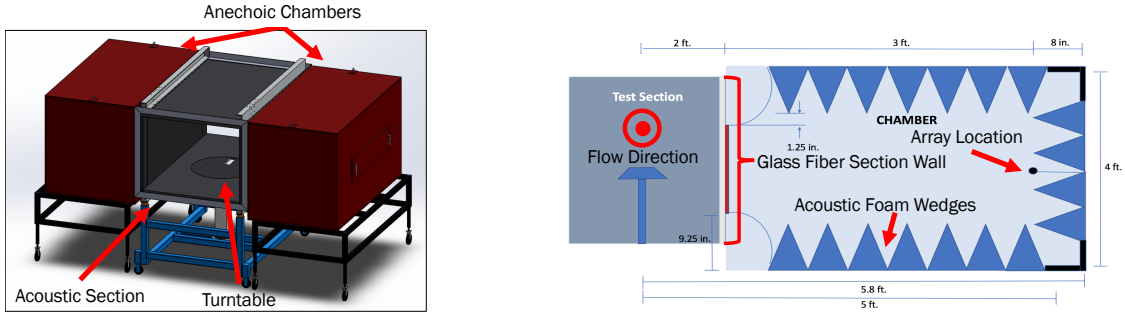

(a) Design of acoustic assembly

(b) Design of anechoic chamber

Figure 5.1: Diagrams describing the design of the acoustic section and chambers by the senior design team.

[1]This chapter has content from [35]; reprinted by permission of the American Institute of Aeronautics and Astronautics, Inc.

The Texas A&M University acoustic test section had a 3 ft x 4 ft cross section, and was constructed using flat acoustic foam panels wrapped in stretched glass fiber cloth, as depicted in Figure 5.3. The foam was used reduce reflections from the test section walls, which contaminate microphone measurements. The two side walls of the test section included a rectangular region over which only the glass fiber extended, i.e., no structure or acoustic foam was present here. Two anechoic chambers were placed against the vertical walls of the acoustic section, covering the two rectangular glass fiber cloth walls of the test section. Unlike the aerodynamic test section, the vertical walls of the aeroacoustic section were acoustically transparent but constrained the majority of flow inside. Virginia Tech accomplished the same task using Kevlar [26] instead of glass fiber. As a result of the vertical walls not being load-bearing, the CRM wing and slat had to be mounted vertically (Figure 5.2), with a rotational motor (known as a turntable) beneath the section enabling changes to angle of attack, and a 1/8 in thick steel rod extending through the roof of the section, acting as a pin.

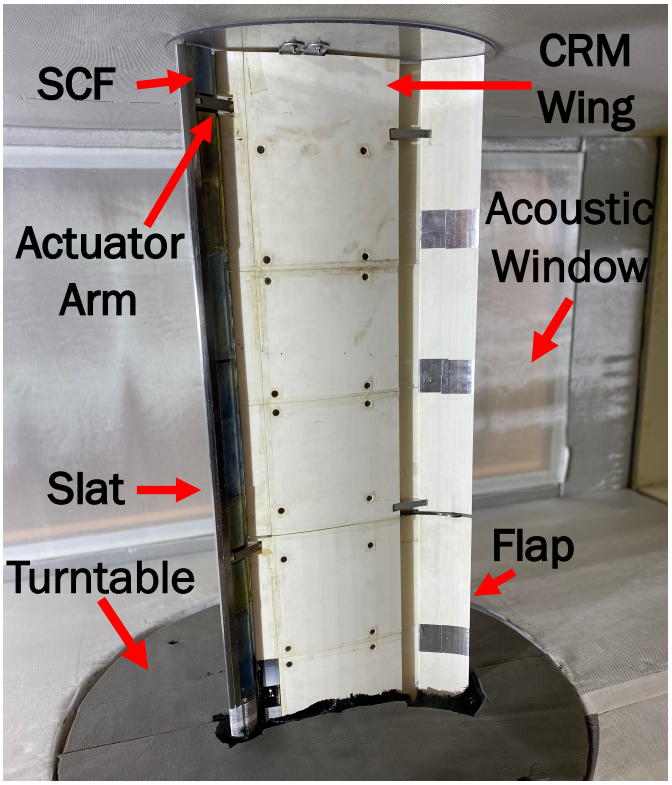

Figure 5.2: Experimental setup of CRM wing treated with SMA SCF placed in the acoustic test section (adapted from Leaton, 2020 [35]).

As the acoustic signal left the test section via the vertical walls and entered the anechoic chamber, it either reached the microphone array or was attenuated by the acoustic foam wedges within the chamber, seen in Figure 5.4.

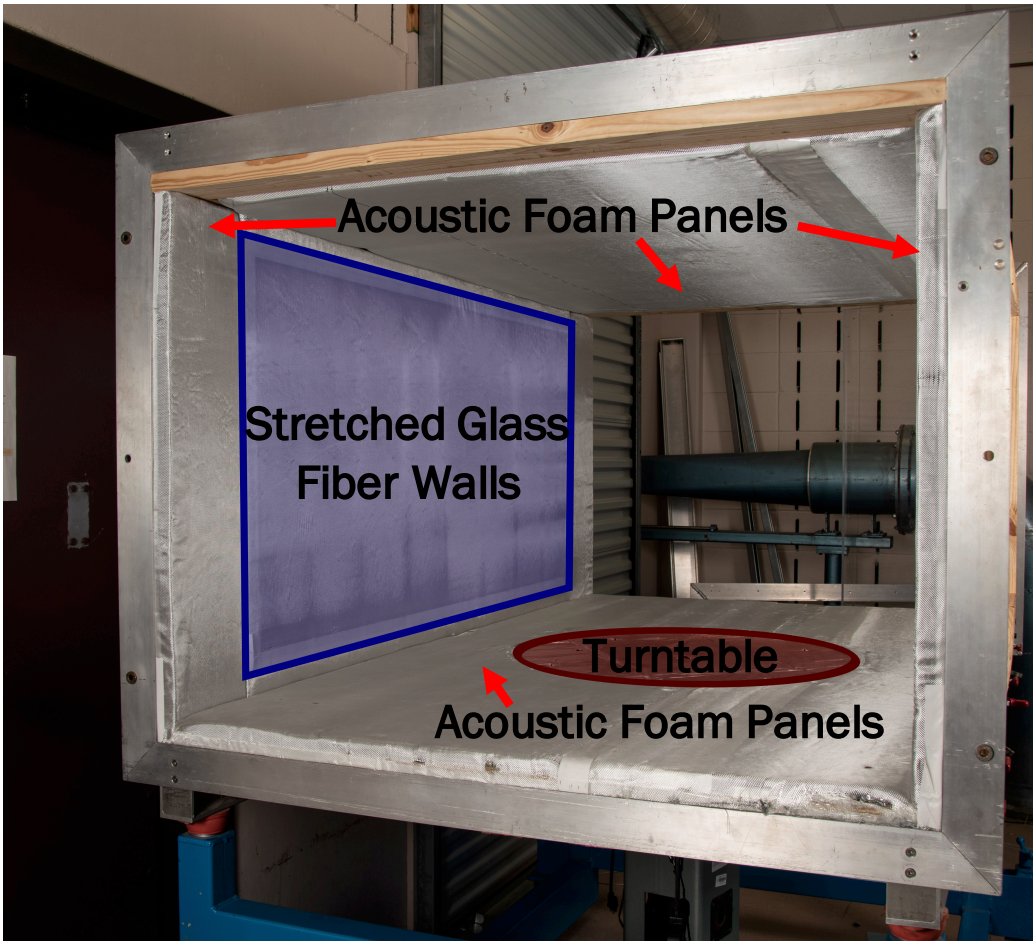

Figure 5.3: Acoustic wind tunnel test section (reprinted from Leaton, 2020 [35]).

Blockage percentage must be calculated for the aeroacoustic section in the same manner as the aerodynamic section. However, unlike the aerodynamic test section, only 3 ft of wing span fits within the confines of the aeroacoustic test section, making the maximum percent blockage approximately 10.4% at 12 degrees angle of attack and 100% deployed. This indicated that all angles of attack up to and including 100% deployed (with the exception of 12 degrees), had a blockage ratio below the 10% threshold.

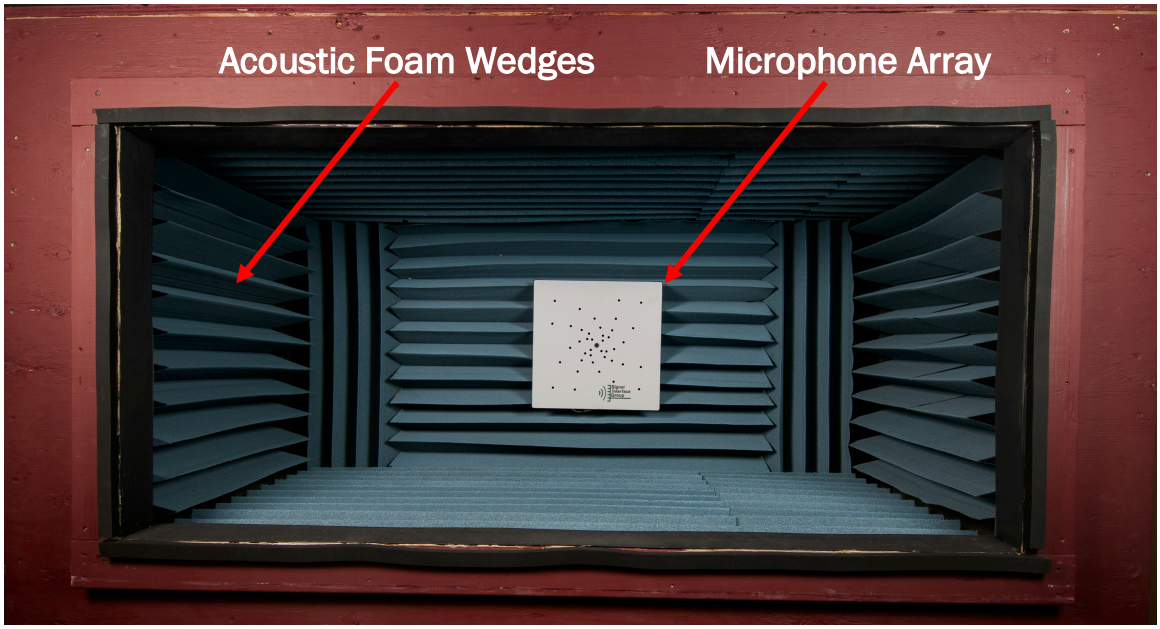

Figure 5.4: Anechoic chamber with microphone array (reprinted from Leaton, 2020 [35]).

To test the effectiveness of the anechoic chambers at reducing external acoustic signals from corrupting internal microphone measurements, a baseline test was conducted. The two chambers were pressed together, excluding the central acoustic wind tunnel section. In this configuration, the acoustic array was enclosed on all sides by the two chambers. Data was recorded and computed using methods explained later in this section (Eq. (5.11), acoustic post-processing, etc), and the results demonstrated the effectiveness of the chambers, as depicted in Figure 5.5. For a test that mirrored how aeroacoustic testing was completed, a second wind-off test was completed, and the results are depicted in Figure 5.6. In this configuration, both anechoic chambers were placed around the acoustic test section while it was inserted in the tunnel.

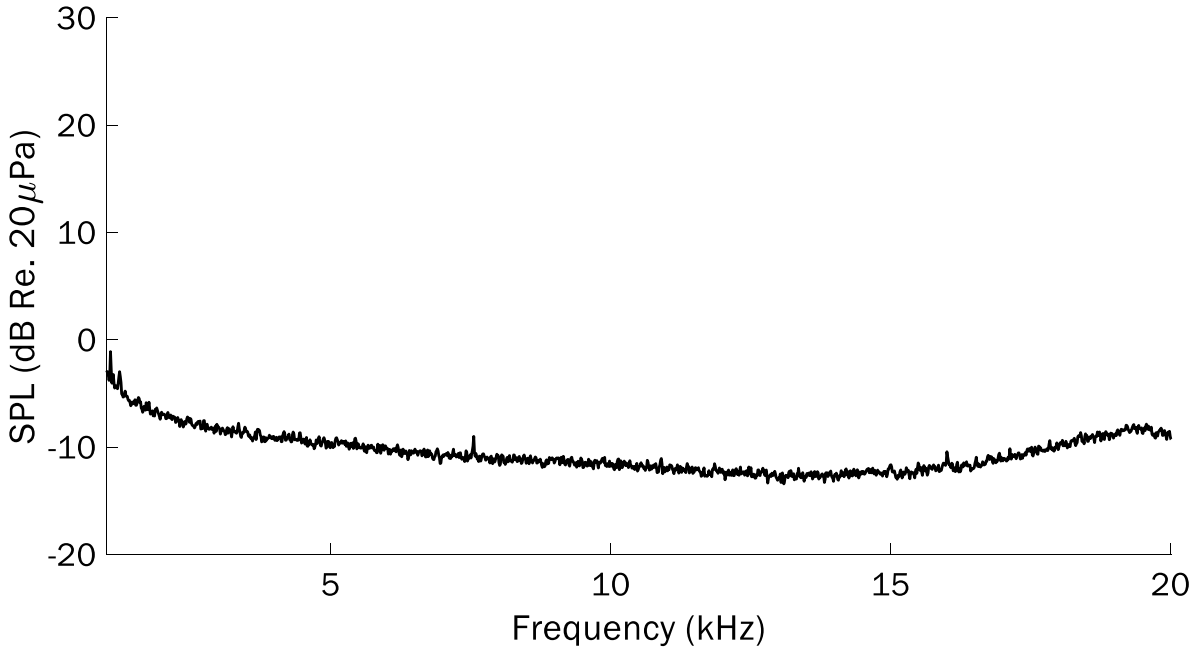

Figure 5.5: Sound Pressure Level recorded by the microphone array when encased by the two anechoic chambers with no acoustic section between them.

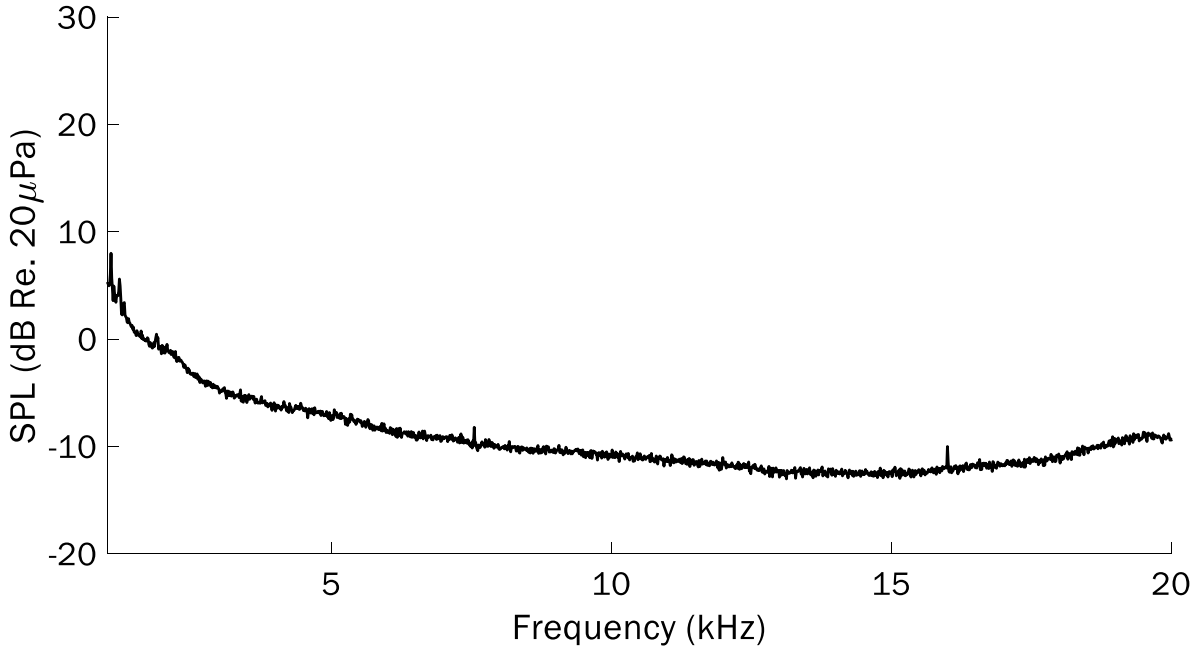

Figure 5.6: Sound Pressure Level recorded by the microphone array when in a normal operating configuration (see Figure 5.7).

To give context, the lowest Sound Pressure Level perceptible by the human ear at 1 kHz is 0 dB [36] (see Eq. (5.11)), therefore any frequency below 0 dB was below the level of human hearing. As depicted in the plot, the level at every frequency tested was below the range of hearing, and thus, imperceptible to the human ear in Figure 5.5, and only low frequency noise could be heard in Figure 5.6. The mean noise floor relative to 20 micropascals for just the two anechoic chambers was -10.2 dB, and when the chambers were attached to the test section in the tunnel, that level raised to -8.2 dB. For this reason, the anechoic chambers were deemed exceptionally effective at shielding the microphones from exterior acoustic signals.

As discussed earlier, the acoustic test section was surrounded on two sides by anechoic chambers. These chambers were manufactured by a mechanical engineering senior design team from Texas A&M University. The main wedge components were C-RAM SFC-WEDGE, a low-density polyurethane foam sold by Cuming Microwave [37]. This foam was specially used for its broadband noise absorption and customizable geometry. The selected foam was 8 in tall, as the height directly corresponds to the lowest attenuated frequency, using Eq. (5.1)

$$\mathbf{f = \frac{c}{4h}} \tag{5.1}$$

where f is the lower bound of attenuated frequency, c is the speed of sound in air, and h is the height of the wedge.

The wedges reduced reflection to a greater extent than the foam panels, as well as limited the amount of ambient noise reaching the microphones. The combination of the anechoic chambers (red outline) and acoustic test section (black/gray) is depicted schematically in Figure 5.7. The array was placed in the chamber not only to reduce acoustic reflection (which assists in source localization), but also to remove it from interaction with the majority of flow in the wind tunnel. The pressure fluctuations caused by normal wind tunnel operation was often orders of magnitude higher than the acoustic pressure fluctuations the microphone was looking for. As a result of placing the array within the chamber, the array received very few, if any, flow pressure fluctuations.

Additionally, the array was placed approximately 4 inches off the back foam wedges, which corresponded to around 25% of the wavelength of the lowest frequency measured (1000 Hz). This was done to further prevent low-frequency reflections from interfering with microphone data.

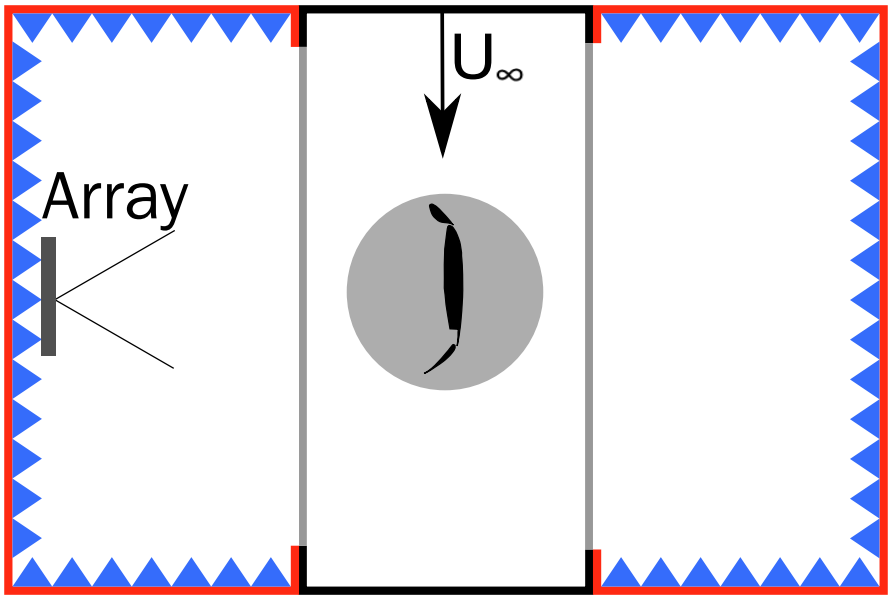

Figure 5.7: Acoustic wind tunnel test section surrounded by two anechoic chambers (reprinted from Leaton, 2020 [35]).

The most novel technology utilized in this work is the beamforming microphone array. The ACAM 120 microphone array, developed by Signal Interface Group, utilized 40 individual microphones and a central camera in order to visualize noise sources. This is accomplished using software called BeamformX [38], created by OptiNav. The 40 individual microphones each accurately recorded acoustic data between 50 Hz and 20 kHz, and had a sampling frequency of 51.2 kHz, meaning that the entire array collected more than two million samples every second. The central camera contained a five MP color sensor, although the image quality exported through the BeamformX software was significantly lower. Additionally, considering there is a stretched glass fiber wall between the array and wing, the quality of the image was degraded further. However, general features of the wing are still visible, which enabled sound source localization. The microphones

were arranged in a logarithmic spiral, which reduced side lobe features from noise sources when compared to an even or random microphone distribution [39]. Comparing a high quality single microphone, the GRAS 46AE 1/2 inch free-field microphone, to one of the less expensive central microphones within the array, we see in Figure 5.8 that the results were surprisingly similar. Considering that the single mic had a much higher price point and was considered free-field, whereas the array microphone was encased in the body of the array, the two results, taken by recording the empty wind tunnel at 15 m/s, seem to support the array as an accurate data collection device. The two microphones do begin to vary by 16 kHz, which may indicate that the array microphone calibration by the manufacturer may have been inferior. Considering the single mic was several orders of magnitude more expensive than each of the array microphones, this high frequency difference was not unexpected. However, since all testing in the rest of this is focused on the difference between two measurements made by the array (instead of comparing data between the array and single mic), this error likely did not influence results. While the microphone came calibrated from the manufacturer, its often good practice to re-calibrate every year. For instance, the free field mic came with a calibration kit which was used twice in a year. Any future research into aeroacoustics using this array should calibrate the microphones before further use.

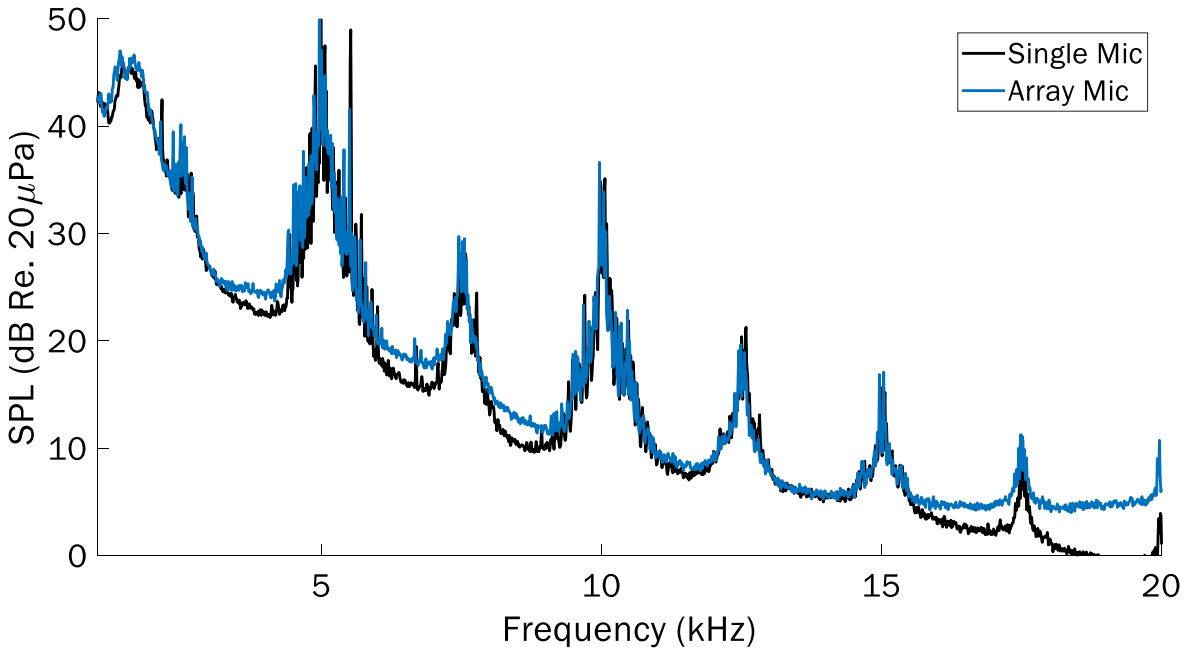

Figure 5.8: Comparison between a GRAS 46AE free-field mic and a centrally placed mic within the array.

The array and software are able to spatially localize sound sources using a concept called beamforming [40]. Beamforming relies on the principal that waves propagate through a constant-temperature medium at a constant velocity. Utilizing this concept, an acoustic wavefront produced by a source would reach individual microphones located at various distances at various times, and thus with various phase. With knowledge of the location of the microphones within the array (which was built into the software), and the phase of the incoming signal, the location of the source can be discovered, as depicted in Figure 5.9. Once the source has been localized, the BeamformX software overlaid a contour of the signal over the video captured by the central camera.

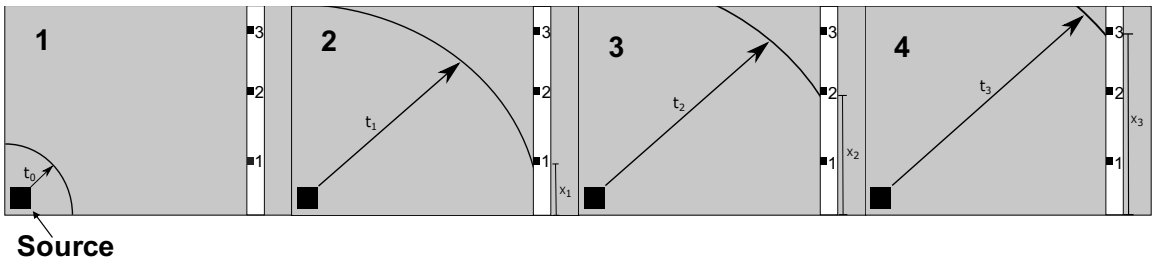

Figure 5.9: Schematic describing the process of beamforming. 1) Initial signal is emitted from a source, 2) the signal reaches microphone one at t_1, 3) microphone two at t_2, and 4) microphone three at t_3. Reprinted from Leaton, 2020 [35]

In addition to the software provided, additional post processing software was developed by Texas A&M University. The purpose of this software was to standardize plotting and the computation of other metrics, such as overall sound pressure level, which was not included in BeamformX. Some fixes to flaws inherent to the array, such as microphone responses, were implemented in the Texas A&M University version of the software, and depicted in Figure 5.15. This software imports the binary data files created by the BeamformX software, and has the ability to create spectra plots, OASPL values, and spectrograms (plots comparing frequency spectra as a function of time and SPL), making it suitable to analyze both steady-state and dynamic tests alike.

5.1.2 Senior Design Contributions to the Reduction of Wind Tunnel Background Noise

Accurate aeroacoustic noise data was collected using the software, hardware, and methods described in the previous section. However, due to the size and type of motor and fan blades utilized in the 3 ft x 4 ft wind tunnel, the noise produced by the motor assembly itself significantly overpowered the noise produced by the wing at specific frequencies. The main narrow band frequency was approximately 2.5 kHz, and harmonic tones existed at integer multiples of the main frequency, reducing in power as the frequency increased. In an attempt to reduce this background noise and increase the dynamic range of the microphones, a mechanical engineering senior design team was tasked with studying the problem and providing solutions for tunnel noise reduction. Ultimately, their solutions were to change the pitch of the fan blades to reduce the RPM of the motor at a given flow velocity, and to install foam panels onto the walls of the tunnel (both preceding and following

the test section) to attenuate motor noise before it reached the microphones. These methods were inspired by work done at Virginia Tech[41]. However, experiments with the picth of the fan blades demonstrated the blades were already in their lowest-noise-production position, therefore only the tunnel walls were treated, as depicted in Figure 5.10. The location of the panel installation is highlighted in Figure 5.11, as these areas would most effectively reduce noise at the test section from the tunnel.

Figure 5.10: Acoustic panels mounted to the settling chamber by senior design team.

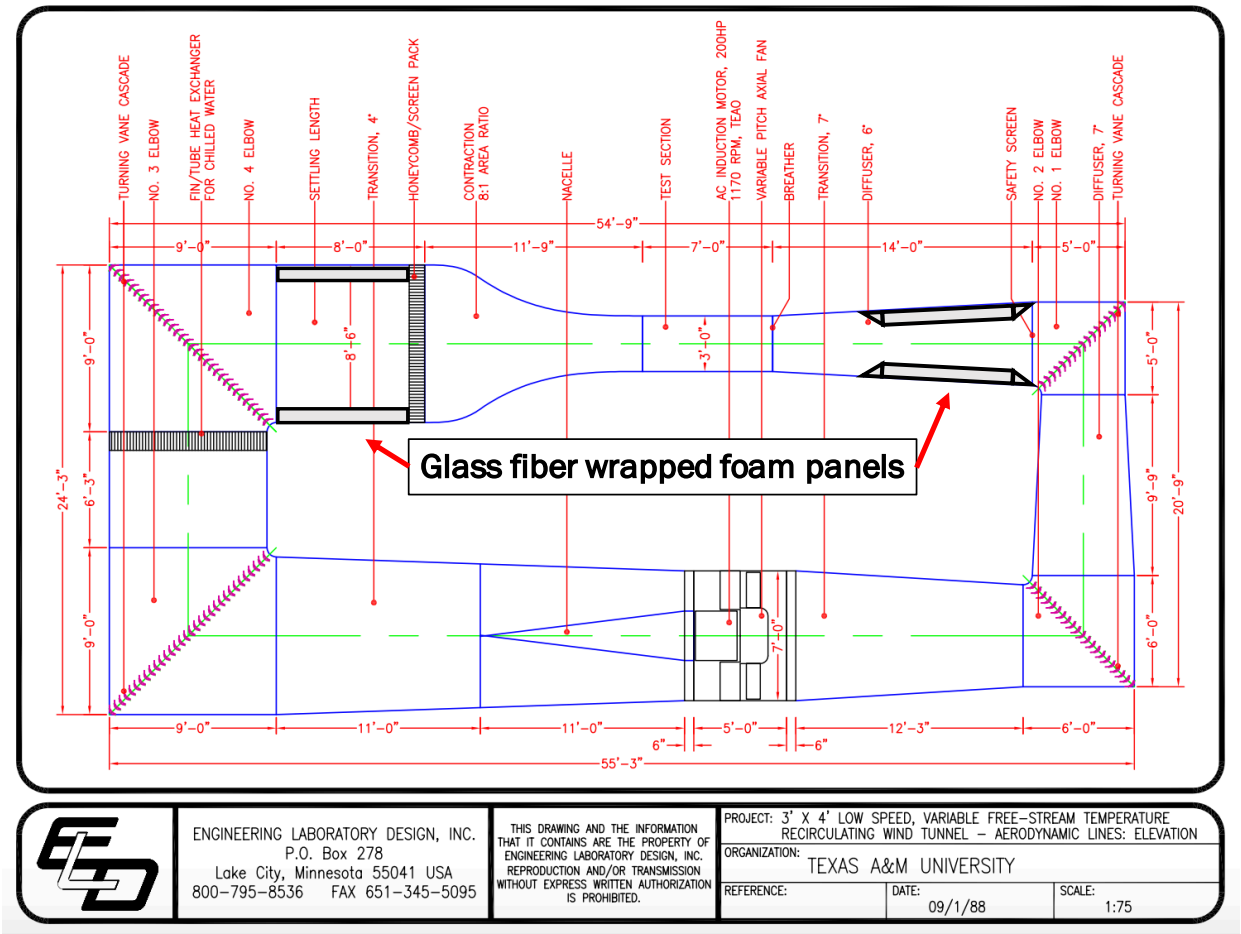

Figure 5.11: Schematic of wind tunnel with senior design acoustic additions highlighted.

The overall sound pressure level was recorded once the panels were installed and compared to the noise in the tunnel prior to the acoustic treatment. A significant reduction in noise (especially below 5kHz) was measured in the treated tunnel, as depicted in Figure 5.12. The tunnel treatment resulted in between a one and four dB reduction at all measured velocities, which in turn, should increase the dynamic range of the acoustic source of interest.

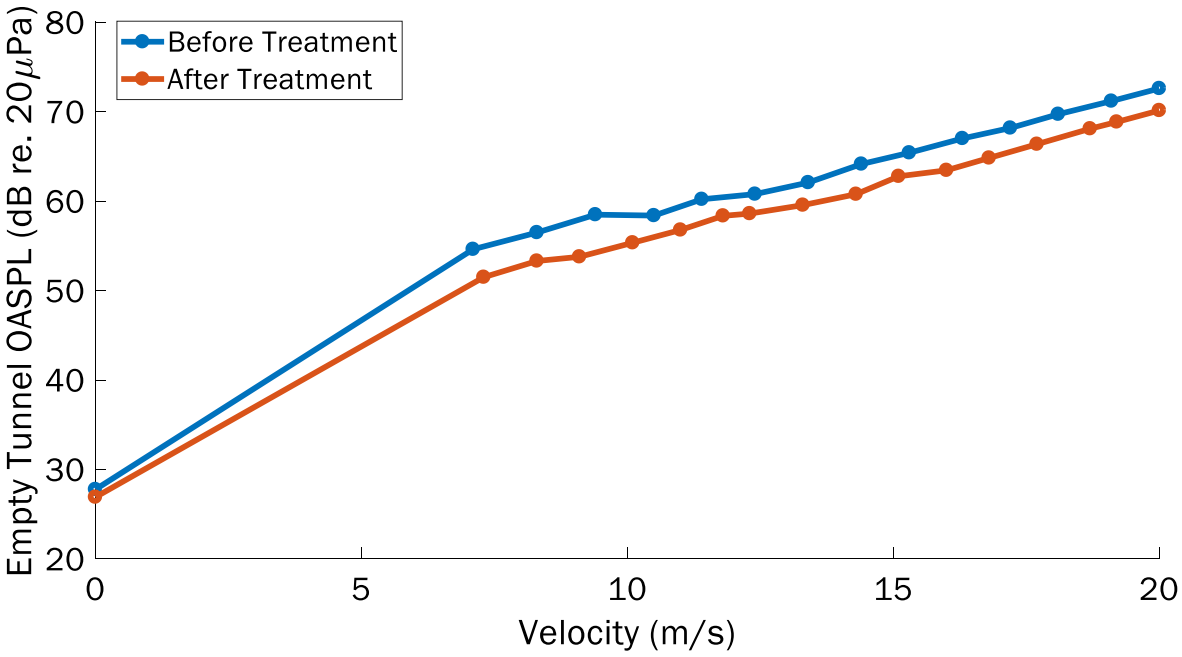

Figure 5.12: Empty tunnel Overall Sound Pressure Level comparison before and after senior design acoustic additions.

For all acoustic testing, the original aerodynamic test matrix was modified. While the deployment levels and velocities stayed the same (100% to 5% deployed in 10% increments and 15-30 m/s in 5 m/s increments, respectively) the angles of attack span was lessened. Instead of testing -2°-12° (which were originally derived from the maximum acceptable force on the load cells of the aerodynamic section), only 4°-12° were tested. While 3° [42] is typically used for the aircraft descent angle, many urban airports with surrounding buildings have higher angles (around 5.5° in London). Since urban airports would be most affected by aircraft noise, the minimum testing angle was adjusted to 4°. Additionally, this angle was used for Boeing acoustic testing of landing gear [43].

5.2 Beamforming Formulation

Beamforming has many algorithms by which the spatial, level (dB), and frequency content can be further refined and the accuracy improved. While the exact algorithm used in the BeamformX software isn't public knowledge, it is likely based on many of the same foundations that all beam-

forming software contains. The basic elements of most beamforming algorithms are as follows: i) Define a plane on which the observer believes the source is present, and mesh this plane into a grid (usually rectangular) with nodes at each corner. ii) Have each microphone look at each node, with the knowledge that the measured signal is delayed by

$$t_0 = \frac{|\mathbf{x} - \mathbf{x_0}|}{c_0} \tag{5.2}$$

where t_0 is referred to as the retarded time, $|\mathbf{x} - \mathbf{x_0}|$ is the distance between the observer (microphone) and grid node, and c_0 is the speed of sound. iii) Sum each microphone's signal and divided by the total number of microphones (N). Assuming a source is present near one of the nodes, the summed signal (including the phase delay given by the retarded time) will yield constructive interference and the acoustic source will be identified. If no source is present, no strong signal will be detected, and therefore, the beamformer will output nothing. This methodology is known as Delay-And-Sum beamforming.

Mathematically, the output of the beamformer can be expressed in the time domain as

$$L(t, \mathbf{x_0}) = \frac{4\pi}{N} \sum_{n=1}^{N} p_n(\mathbf{x_0}, t + t_0)|\mathbf{x} - \mathbf{x_0}|\,, \tag{5.3}$$

where N is the number of microphones, p_n is the recorded signal for each microphone, $\mathbf{x}$ is the microphone location and $\mathbf{x_0}$ is the node location. In order to gain frequency information from the underlying time-based pressure data, Fourier transforms are needed. The transform of Eq. (5.3) is then

$$L(\omega, \mathbf{x_0}) = \frac{1}{M} \sum_{n=1}^{M} s(\mathbf{x}, \omega) P(\mathbf{x}, \mathbf{x_0}, \omega)\,, \tag{5.4}$$

where s is the steering function defined as

$$s(\mathbf{x}, \mathbf{x_0}, \omega) = 4\pi|\mathbf{x} - \mathbf{x_0}|e^{-i\omega t_0}. \tag{5.5}$$

The steering function provides a built in way to address the inherent phase shift associated with

having microphones at various locations. This function can be collected into a vector for all N microphones within an array called the steering vector

$$g(\mathbf{x},\omega) = \begin{pmatrix} 4\pi|\mathbf{x_1} - \mathbf{x_0}|e^{-i\omega t_1} \\ 4\pi|\mathbf{x_2} - \mathbf{x_0}|e^{-i\omega t_2} \\ \vdots \\ 4\pi|\mathbf{x_N} - \mathbf{x_0}|e^{-i\omega t_N} \end{pmatrix}. \tag{5.6}$$

Within the steering vector, $|\mathbf{x_M} - \mathbf{x_0}|$ is the distance between microphone M and the grid node $\mathbf{x_0}$, and t_M is the wave propagation time between those two locations.

To combine the information gained by each of the microphones within the array, correlations must be calculated. Similar to cross correlation, which is the degree of similarity two variables share as one displaces with respect to the other, beamforming relies heavily on the Cross-Spectral Matrix (CSM), otherwise known as the cross power spectral density matrix. If it is assumed that the instantaneous signal from all the microphones within the array examining a single frequency bin, after a Fourier-transform, has content

$$M(\omega) = \begin{pmatrix} P_1(\omega) \\ P_2(\omega) \\ \vdots \\ P_N(\omega) \end{pmatrix}, \tag{5.7}$$

where P_1 is the pressure of microphone 1 at angular frequency ω, then the CSM of the signals from all N microphones at one frequency bin is

$$CSM(\omega) = \begin{pmatrix} M_1M_1^* & \cdots & M_1M_N^* \\ \vdots & \ddots & \vdots \\ M_NM_1^* & \cdots & M_NM_N^* \end{pmatrix}, \tag{5.8}$$

where * indicates a complex conjugate, and M_x represents the xth entry in M (which is the Fourier-

transformed signal from microphone x). A single matrix, as shown in Eq. (5.8), is created for each frequency bin shown. Assuming a coherent (signal with the same phase) signal is detected at a specific frequency, the elements related to the microphones receiving those signals will contain only real numbers and their contribution will be depicted on the beamforming map.

Another important concept intimately woven into the fabric of signal processing is the Point Spread Function (PSF), which provides information on the effectiveness and accuracy of the microphone array. Assuming the array was infinitely large with a continuous distribution of microphones throughout, beamforming would display a single point source output to a monopole input. However, given that no array can fit either of the criteria above, false sources and large side-lobes can appear on the beamforming map, indications of poor PSFs. Geometry, microphone distribution, and array size all have an effect on the PSF of the recorded signal. These errors can be attributed to the convolution between the actual input and the array PSF [40], which yields the recorded input, shown below

$$h = f * \mathbf{g} \tag{5.9}$$

where h is the recorded signal, f is the actual signal, **g** is the system transfer function (in this case, this is equivalent to the array PSF), and * is the convolution operator. In some applications, the actual signal is obtained by the deconvolution of the array PSF and the recorded signal to recover a more clear signal. These deconvolutions attempt to remove array-dependent inaccuracies, producing a more repeatable and accurate result.

With the steering vector, CRM, and PSF established, a beamforming map can be created. One of the newest beamforming map algorithms developed by Robert Dougherty [44] called Functional Beamforming has higher dynamic range and better resolution than previous algorithms. The formulation for this map is simply

$$b_\nu(g) = [g' C^{\frac{1}{\nu}} g]^\nu \tag{5.10}$$

where ν is the order of the formulation, g is the steering vector, and C is the CSM of the array. Functional Beamforming appears to accurately locate sources when $\nu \geq 1$, and seems to increase

in accuracy as $\nu \rightarrow \infty$. While this is one beamforming expression, many others exist with varying levels of accuracy, speed, and modularity, such as DAMAS (Deconvolution Approach for the Mapping of Acoustic Sources) [45], DAMAS2 [46], CLEAN-PSF [47], and CLEAN-SC [48].

Finally, additional advances in both microphone array geometry and beamforming formulation have been achieved by Shah et al. [49]. By utilizing a moving microphone array and novel formulation, Shah and his group were able to synthetically increase the effective number of microphones within the array, dramatically increasing spatial resolution and reducing side-lobes. Further research may enable the main entry-barrier into beamforming (cost) to be dramatically reduced without a reduction in data quality.

5.3 Acoustic Post-Processing

5.3.1 General Acoustic Processing

For all tests in which a single spectra was examined, microphone 18 was used. This microphone was chosen because it was among three other microphones that were closest to the center of the array, therefore possible interference caused by the sides of the array would be less severe. The array and selected reference microphone is displayed in Figure 5.13

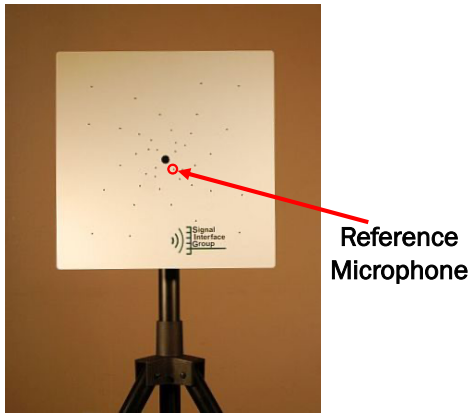

Figure 5.13: Microphone array with highlighted reference microphone used for the creation of all spectra plots.

In order to post-process data produced by the microphone array into usable SPL or OASPL results, several changes needed to be made. The raw data files produced by the ACAM 120 array were 24-bit binary files, padded to 32-bit. After selecting the desired data files and outputs within the script, MATLAB would import the file, read the metadata, convert the data to 24-bit, and store the raw acoustic data as integer values. This initially caused some trouble, as BeamformX does not output binary data in the standard format that Windows follows. Multi-byte binary data is arranged in either most significant byte first (Big-endian), or least-significant byte first (Little-endian). The array produced Big-endian data, while more typical systems produce and use little-Endian data. Once this was addressed using the 'ieee-be' flag in Matlab, the data processing went much more smoothly. Based on the metadata gathered, the data was divided based on the microphone that captured it and the time it was collected. Since the array had 40 microphones collecting pressures at 51.2 kHz, the array collected about 1.2 GB/min of data. Within the post processing script, the user had the option of processing all 40 microphones, or more commonly, just a single microphone. Typically, microphone 18 was used as a standard single mic, as its centrally located within the array. Once a microphone had been chosen, its data was then converted from the time domain to the frequency domain through a Fast Fourier Transform (FFT). The absolute value of the FFT was taken (which was needed as the MATLAB FFT algorithm computed the discrete Fourier transform, which may contain unwanted information such as phase), and the values were divided by the chosen transform length (TL) to normalize the output, correcting for the total energy present over different sampling times. If the data required the inverse Fourier transform to return to the temporal domain, phase information could not be disregarded, but since this work remained in the time domain and used averaging to increase the signal to noise ratio and reduce random noise, phase information was not needed. The transform length was essentially used as a measure of the frequency resolution of the FFT. Because of the implementation, the transform length had to be a power of 2 (a property of any FFT), and 4096 was most often selected for high levels of frequency resolution. However, during dynamic tests, when resolution in the time domain is equally important as the frequency domain, a TL of 512 was used which provided a

detailed acoustic time history at the expense of some frequency precision. Other TLs used were 1024 and 2048.

Now that a TL had been chosen for a particular test and the absolute value of the FFT had been divided by the TL, only a portion of the frequency data was used. This portion was defined by, again, the TL. Because of the way MATLAB computes the discrete Fourier transform, the spectrum output spans from $-F_{max}$ to F_{max}, which is referred to as a double sided spectrum. Since the negative portion is identical to the positive portion, only one side is used, referred to as a single sided spectrum. This introduces a signal processing topic that will only briefly be discussed known as the Nyquist Sampling Theorem. This states that the signal can be perfectly reconstructed if the sampling rate is over twice the value of the highest frequency component [50]. This helps to avoid aliasing, which allows artifacts to corrupt the signal. Although it had never been stated directly, the 51.2 kHz sample rate of the array is likely to accommodate this theorem, as the maximum frequency component of the array is 25 kHz. The necessary data was contained within the first $\frac{TL}{2}$ points (to satisfy the Nyquist Sampling Theorem), therefore subsequent data is truncated.

To compute an average pressure over the recorded period, the root mean square (RMS) of the pressure in each block of data was calculated, which was used as P_0 in Eq. (5.11). An example makes this process more understandable. Assuming data was collected over 10 seconds, 512000 total samples would be recorded (see the sampling rate above). Assuming a transform length of 4096 was chosen, once the data was transformed into the frequency domain, the data would be broken into blocks of 4096 samples, which describe the spectral content over that time period. Since each block was 4096 samples long, 125 blocks in total would be created over the 10 second data recording. Therefore, for an average pressure over the sampled period, the pressure recorded by each microphone at each frequency bin would be RMS averaged across all 125 blocks, leaving a single averaged pressure measurement for each frequency bin for each microphone. SPL could now be calculated. Finally, once SPL or OASPL was selected as the final output, the underlying data was adjusted to correct the microphone response. This is explained in more detail below.

5.3.2 Dynamic Acoustic Experimental Setup

While the majority of acoustic data was processed to be time-averaged, there were some instances where the time history, and how the acoustic data changed over that history, provided needed insights into the behavior of the SCF. These plots, which display time (or some function of time, such as deployment level during a retraction or deployment event in a dynamic test) on the x-axis, frequency on the y-axis, and SPL on the z-axis, are very helpful for dynamic testing. For dynamic acoustic tests, the system to create figures was more elaborate. First, the test data was recorded by LabView, which, in this work, was typically only used for aerodynamic tests. LabView gathered wind tunnel velocity, angle of attack, deployment location, and load cell data, but acoustic data collection was completed entirely independently, through the array's software. LabView output the average deployment % for slat and flap, and wrote this value to a text file at a rate of 3 Hz. Within LabView, the actuators, instead of being instructed to move the slat and flap independently, were commanded to move together. As a result of the different deployment paths, as well as contact between the SCF and leading edge, the slat required more time to move from a deployed position to a retracted position (or vise-versa). In order for both high lift devices to move in an approximately simultaneous manner, the current position of the slat was used as the instructed position of the flap, enabling both to actuate nearly identically.

Next, the LabView data recording, BeamformX acoustic recording, and actuator movement were all synchronized to begin at the same time. Once the test has been completed, the text file created by LabView was modified. To begin, the slat and flap values, which sometimes differed as much as 10%, were averaged to produce an averaged high lift device deployment level. With this averaged value and knowledge of the sampling rate of LabView, a relation between time and approximate % deployment was created. Instead of keeping the values as discrete, the built in Microsoft Excel polynomial fit tool was utilized, and a 6th order polynomial (relating % deployment to time) was created for each dynamic test. Once the fit was complete and a 6th order equation was created, this continuous equation was put inside the post-processing script for acoustic data. With this equation, acoustic SPL values were related to average deployment level at any sample

rate, enabling the creation of Figure 5.14. It is extremely important to note that a new relationship between time and deployment level must be developed for each test, as the amount of time the retraction and deployment process takes has been found to be inconsistent. This includes differing flow velocities, angles of attack, and configuration.

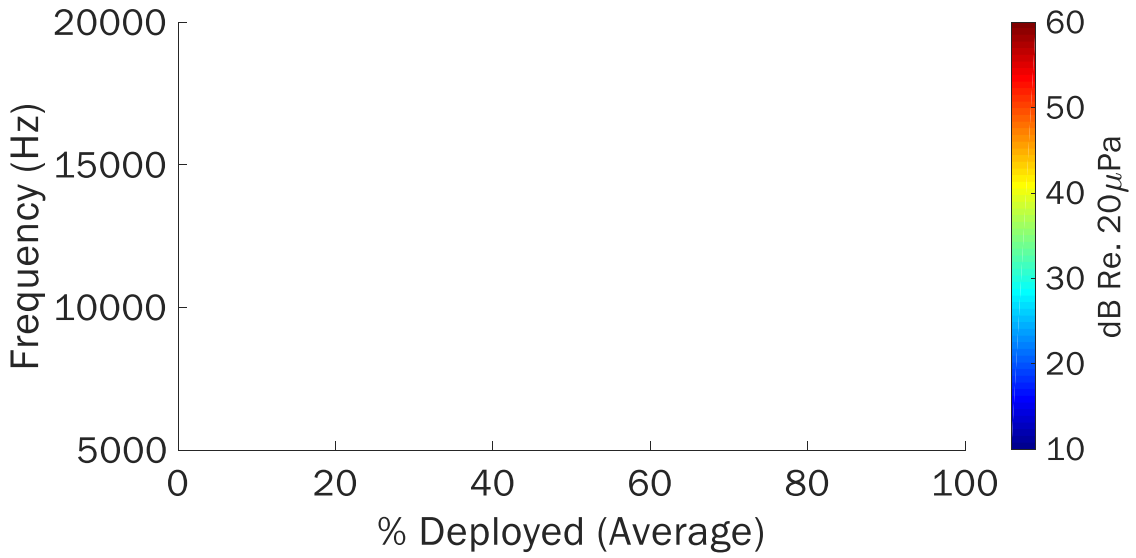

Figure 5.14: Example displaying the data utilized for spectrograms.

5.3.3 Acoustic Calibration and Beamforming Correction

Inaccuracies inherent in the microphones of the array were discovered. All microphones (to varying degrees) exhibited a non-flat frequency response manifested as a roll-up in sensitivity at around 7 kHz. These uneven responses could be theoretically helpful in certain situation, such as music recording where a smaller known frequency range will be recorded, and purposefully amplified. However, for this work, a flat frequency response was preferred, as all frequencies produced were important and the all the energy in the signal was accounted for. As a result, and with the help of a microphone response diagram provided by Optinav, a correction was built into the acoustic post-processing. Data was taken from the provided response and extracted using an online program called Web Plot Digitizer, which produced .csv files containing numerical data

taken from images of plots. Using this data, a correction was added to the script, which used the raw pressure data from the array, and modified it according to the response, before converting the data to SPL, OASPL, or any other data type. For instance, the microphone response data indicated that at 18 kHz, the microphones artificially increased the sound pressure level by nearly 10 dB. To correct this, the pressure data corresponding to 18 kHz is then reduced by the necessary amount to indicate the true SPL, approximately 10 dB lower. This change is depicted in Figure 5.15.

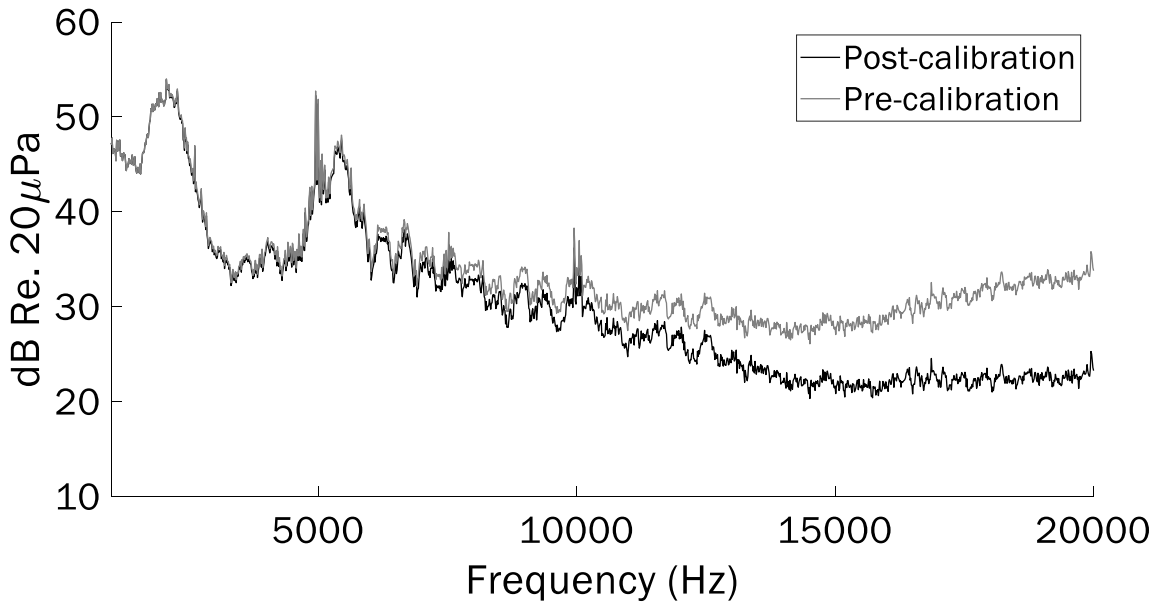

Figure 5.15: Microphone spectrum before and after implementing microphone response within post-processing. This test was completed using an untreated slat at 100% deployed, 6°, and 20 m/s.

Due to the problems inherent to common beamforming formulations, corrections to the beamforming image had to be made, dependent on flow velocity. Because the beamforming source localization image fundamentally relied on the propagation of acoustic pressure waves through air, the position of a point source could be corrupted by movement of the medium between the source and array. When operating in a wind tunnel, the high velocity flow needed to test the CRM wing also shifted the perceived location of sources downstream. Figure 5.16 demonstrates a simple test, in which a speaker (outlined in red) was driven at a tone, and the beamformed source location was

tracked as wind tunnel velocity increased.

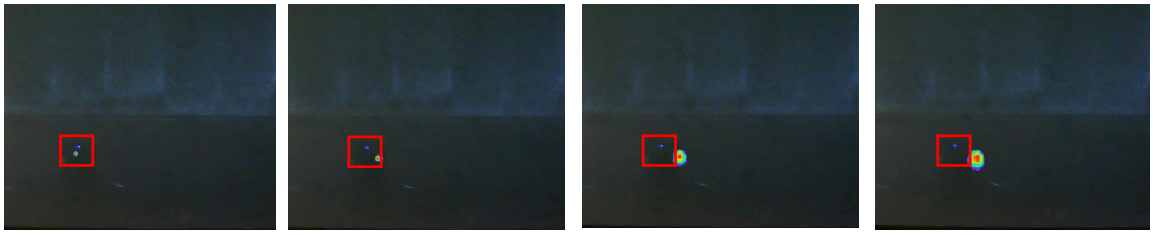

(a) 0 m/s (b) 20 m/s (c) 32 m/s (d) 38 m/s

Figure 5.16: Contour showing the source location as perceived by the array. As velocity increased, the source artificially shifted downstream. The size of the source (though not the level) appeared to increase as well, which could be caused by differences in refraction angle between microphones, as each has a unique angle to the source. The source size increases could not be corrected.

Because this is an issue inherent in many types of beamforming, the BeamformX software had a method of fixing the issue. The user could input a velocity, and the beamformed source would artificially shift back to its correct position. However, the velocity input needed to be calibrated to the specific experimental setup used at Texas A&M University, therefore a calibration plot was created and displayed in Figure 5.17. The velocity input for the software was in terms of Mach number, and a negative Mach was used, as the array default flow direction (right to left) was opposite to the experimental setup used (left to right). Given a known flow velocity at the tunnel section, the corresponding mach input given in Figure 5.17 ws entered into the "machX" field within the "Air Properties" tab of the BeamformX software GUI. This calibration was only accurate for the experimental setup at Texas A&M University, and was not globally applicable.

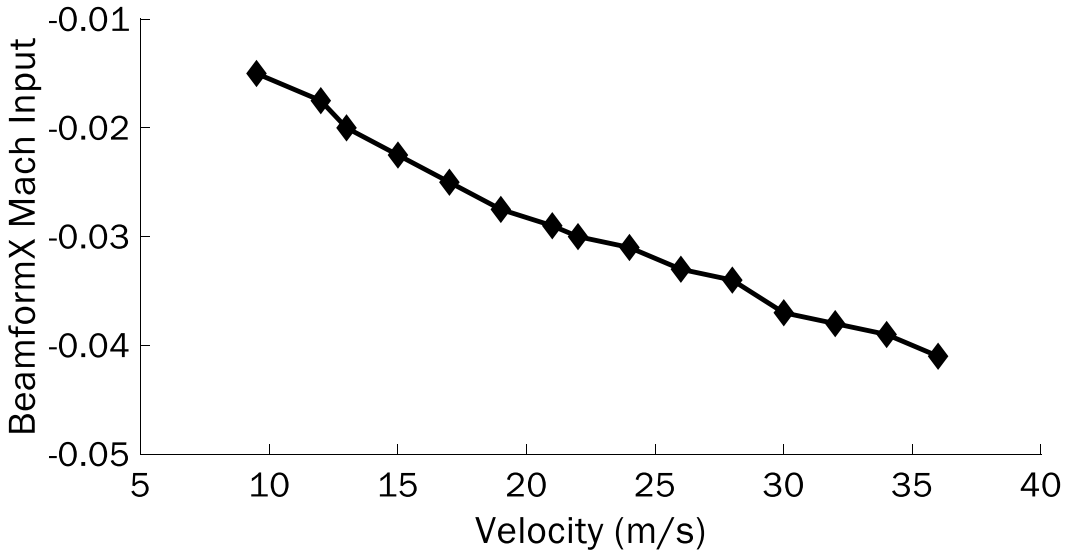

Figure 5.17: Using BeamformX software, the beamformed source location can be corrected by inputting a mach number given by the wind tunnel flow velocity.

5.4 Aeroacoustic Results

5.4.1 Model Scale Acoustic Spectrum Results

Computing the noise level at a specific frequency was completed using Sound Pressure Level (dB). SPL is a log relationship between the measured acoustic pressure at a specific frequency and some reference pressure. For all data presented here, the reference pressure was the standard 20 μPa [36], as this is the lowest pressure perceptible by the human ear at 1 kHz. To calculate SPL, the following equation was used.

$$\text{SPL (dB)} = 20log_{10}\frac{P_0}{20\mu Pa} \tag{5.11}$$

Using Eq. (5.11), SPL can be calculated at each frequency and plotted, as shown below in Figure 5.18(a). Again, all spectral content was created using microphone 18, one of the most central microphones within the array.

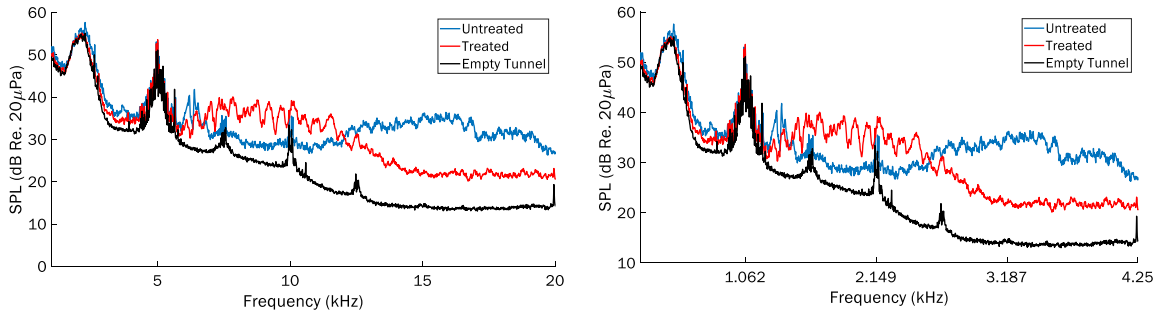

Figure 5.18: Sound Pressure Level at 5°, 20 m/s, 100% deployed, and a transform length of 4096. Both model and approximate full scale frequency content was computed.

Several things should be noted from examining Figure 5.18(a). First, the large narrowband increase in SPL for the untreated case at around 3 kHz was due to a small change in the outer mold line of the CRM wing. The identification and repair of this is detailed later in this section. Secondly, Figure 5.18(a) indicated that both treated and untreated appear to create broadband noise, but at differing frequency bands. Broadband noise creation is typically generated by, among other things, vortex shedding induced by trailing edge bluntness or turbulence caused by flow separation [51]. The purpose of the SCF was to stop flow separation and circulation around the slat cove, and assuming both broadband sources in the treated and untreated case were caused by separation, this may indicate the geometry of the SCF used was not appropriate for the tested length and velocity scales. Additionally, the SCF shape was created using a full scale CRM wing with sweep and taper. However, the current model scale version tested in this work did not include either of those characteristics. Taking a freestream-parallel 2D slice of the wing and SCF midspan may have been inconsistent with the original design, leading to separation. Several more angles were depicted in Figure 5.19, indicating very little change in frequency response given a change in angle of attack.

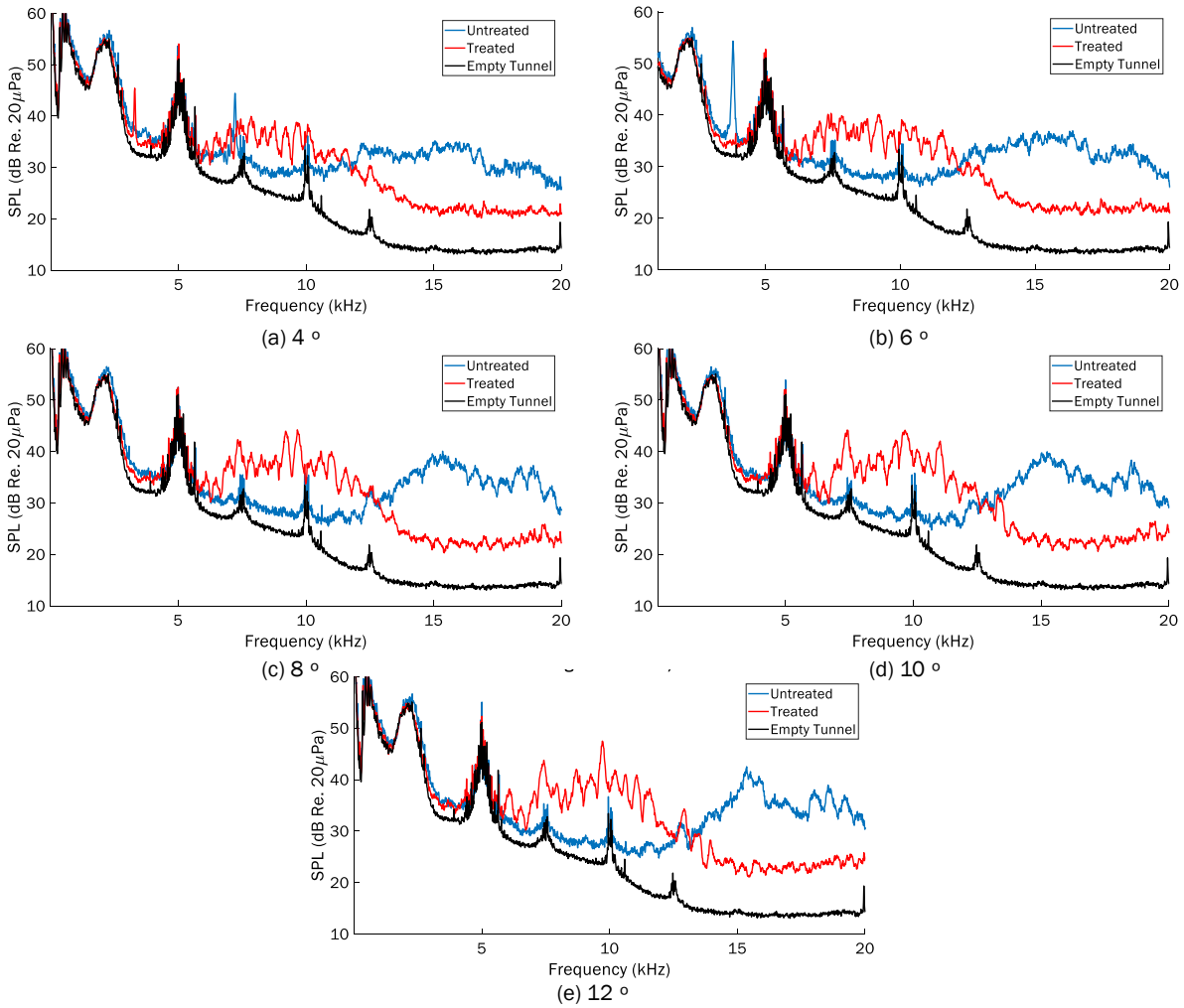

Figure 5.19: Sound Pressure Level at 20 m/s, 100% deployed, and a transform length of 4096. There appeared to be little frequency dependence on angle of attack when fully deployed.

5.4.2 Approximate Full Scale Acoustic Spectrum Results

While experimental testing was completed at model scale, approximating the data to full scale was necessary to provide context. In order to change data from model to full scale, the Strouhal number was used. This dimensionless number was often used to describe vortex shedding behavior [52] and is given by Eq. (5.12).

$$\text{Strouhal Number} = \frac{f * L}{U} \tag{5.12}$$

where f was the frequency content, L was the characteristic length, and U was flow velocity. By taking the Strouhal number as a constant 0.2 [53], the frequency content of various sized objects in various flow conditions was compared. Therefore, Eq. (5.12) was modified as

$$\mathrm{f} = \frac{\frac{U_{model}}{U_{full}}}{\frac{L_{model}}{L_{full}}} \tag{5.13}$$

where the subscripts model and full refer to model scale and full scale, respectively, and f is the frequency ratio between the two scales. A typical aircraft lands at approximately 150 mph (68 m/s), therefore this value was used as the full scale velocity. Additionally, the model was 1/16th scale, so the ratio between characteristic lengths was 1/16 or 0.0625. Finally, the only value needed was the current wind tunnel model flow condition. The frequency scaling factor for the tested velocities is given in Table 5.1.

Velocity (m/s)	**Scale Factor**
15	3.529
20	4.706
25	5.882
30	7.059

Table 5.1: Scaling factor relating the frequency content produced between model and full scale at each wind tunnel velocity.

In practice, to calculate the full scale frequency content given model scale data, the model scale frequency was divided by the scaling factor, yielding the approximate full scale frequency. This was demonstrated in Figure 5.18(b). While the sound pressure level of Figure 5.18(b) was the same as Figure 5.18(a), the frequency had been divided by 4.706 to accommodate the differing velocity and length scales experienced in a full scale aircraft. Most importantly when converting model

scale acoustic data to full scale was the effect on the human ear. Since the goal of this work was to test if the implementation of an SMA-based SCF would reduce the airframe noise level, which inherently includes the noise humans can hear, a range of sensitive tones was needed to compare the treated to the untreated data. The range most often used was referred to as A-weighting acoustics, which emphasized frequencies most easily perceived by humans and depreciated those that are more difficult for humans to perceive [54]. The most sensitive frequencies are between one and six kHz, with the maximum emphasis on approximately 2.5 kHz. The emphasis associated with this range was approximately a Gaussian distribution. Given that all broadband noise production created by both the treated and untreated configuration occur in this sensitive region, and are similarly distributed on either side of the A-weighting apex of 2.5 kHz (approximately where the treated and untreated cross each other), no strong distinctions between the model scale and full scale comparison of the SMA-based SCF were made. It appears the the same observations that were true about model scale were also true at full scale, given that neither treated nor untreated were significantly affected by A-weighting. Therefore a more comprehensive measure of noise creation was introduced.

5.4.3 Overall Sound Pressure Level and Beamforming Acoustic Results

When comparing the effectiveness of noise reduction created by the SCF, an overall measure of energy within a given frequency range was used, called Overall Sound Pressure Level.

$$\text{OASPL (dB)} = 20log_{10}\frac{RSS(P_0)}{20\mu Pa} \tag{5.14}$$

where RSS refers to the Root Sum Square of the measured pressure values across the intended frequency range [55]. OASPL is used to gain a more holistic view of the acoustic response, calculating a single measure of noise level across a band of frequencies. The array produced the most accurate data between 1-20 kHz, therefore the range used for the calculation of OASPL was the same.

Once spectra data was collected for all velocities, angles of attack, and deployment levels,

the OASPL was calculated and is shown in Figure 5.20. It is clear that, at 20 m/s, the addition of the SCF reduced the noise level at all angles of attack significantly, by an average of 1.5 dB. This result is true at 15 m/s as well, but to a lesser extent. However, past 20 m/s, the SCF did not appear to demonstrate significant acoustic savings, sometimes even increasing the noise level. A possible explanation for this phenomena is that, as flow speed increased, the frequency associated with noise created by the slat and wing increased as well. As displayed in Figure 5.18(a), the untreated wing had a higher frequency broadband noise characteristic than the treated wing did, and the central frequency increased with faster velocities. As a result, when velocity increased, some of that untreated broadband noise extended beyond 20 kHz (the upper bound in OASPL), and therefore was not accurately measured or used in OASPL calculations. Without the high dB level broadband noise of the untreated wing, calculations (incorrectly) appeared to show that more noise was created with the treated configuration. Utilizing microphones with higher frequency upper limit would likely continue to show the acoustic savings of the SCF.

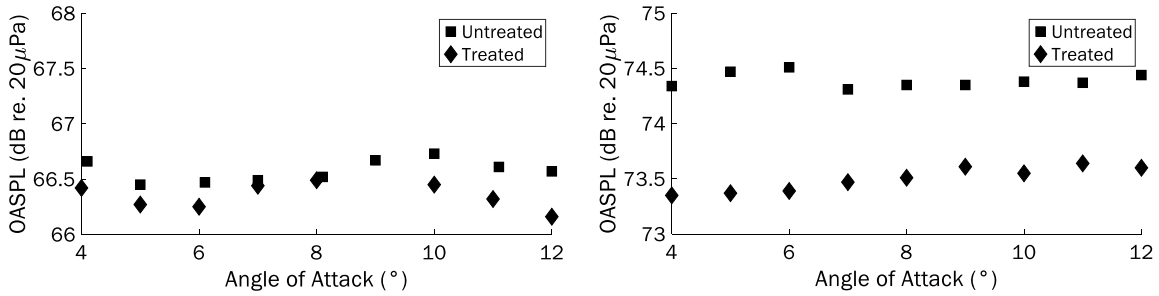

(a) 15 m/s. (b) 20 m/s.

Figure 5.20: Fully deployed Overall Sound Pressure Level (1-20 kHz) at 15 and 20 m/s.

Broadband noise creation is typically generated by, among other things, vortex shedding induced by trailing edge bluntness or turbulence caused by flow separation [51]. The spatial mapping of sound sources through the beamforming array is depicted in Figure 5.21. The main source location can be observed as existing within the slat cove, which could indicate either that trailing edge vortex shedding was being reflected into the cove (as the trailing edge was obscured on the other

side of the wing), or that flow was separated and circulated within the cove, creating a broadband noise source.

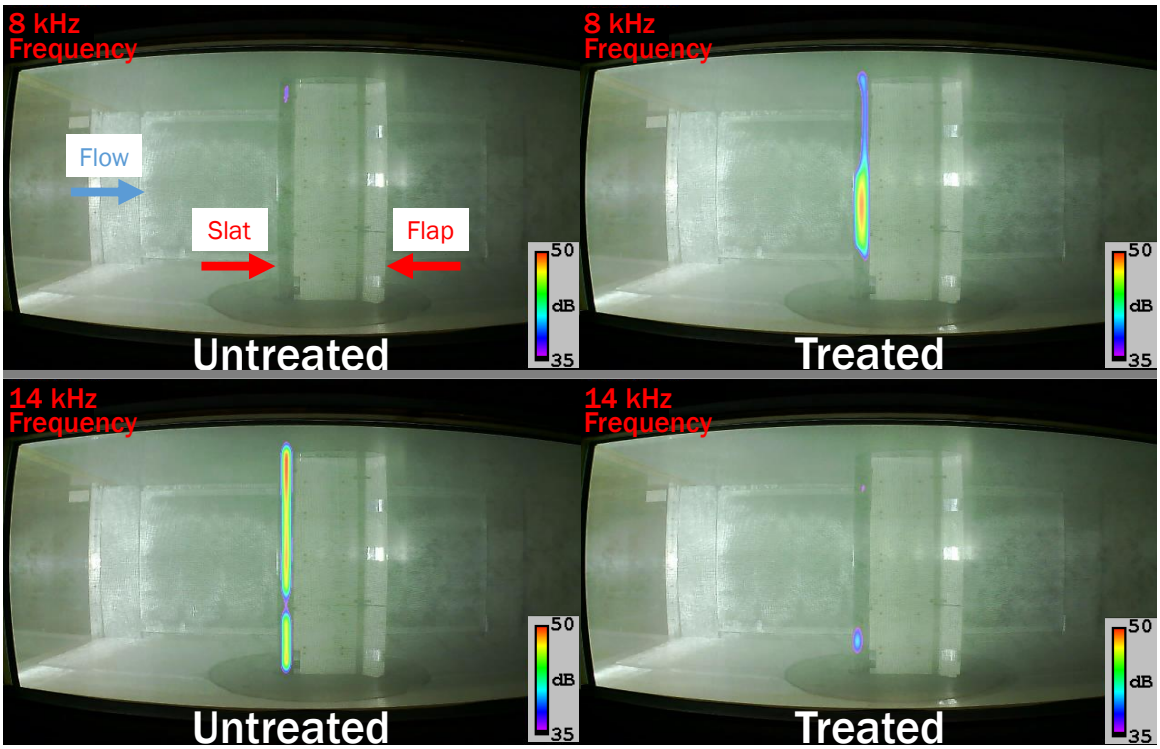

Figure 5.21: Beamforming map of the location of the main sound sources of the wing (8 kHz and 14 kHz) at 20 m/s and 6° angle of attack. The center of both broadband noise sources appears in the slat cove, suggesting that the current SMA SCF did not entirely change the mechanism causing the noise.

5.4.4 Dynamic Acoustic Results and Other Findings

Another aspect of the noise problem with high lift devices was during deployment and retraction, two dynamic sequences. As the slat moved into or away from incoming flow, the noise creation would differ from that measured during steady state tests, as a result of dynamic flow phenomena. These were best captured using spectrograms, which compare time (which can easily be converted to % deployed), frequency, and SPL. Typical spectrum plots were insufficient to display important dynamic information, as they were time-averaged. As depicted in Figure 5.22, several

events transpired during a typical fully-deployed to fully-retracted test. First, as the slat began to retract, the SCF made contact with the leading edge of the wing, cutting off flow between the two bodies. This flow was the source of some high dB noise, and as a result of its termination, an abrupt reduction in SPL was recorded. Secondly, as the slat approached 20% deployment, two distinct intense noises were observed. These corresponded to the SCF snapping from the deployed configuration to the stowed configuration. Recall that the SCF was broken into several sections along the span of the slat, separated by actuator arms. The two snaps were a product of the main SCF portion snapping in first, followed quickly by the SCF edge closest to the roof of the section. Considering that each SMA piece was heat-treated and installed separately, likely a small difference in shape and/or installation details led to the two separate parts of the SCF snapping in at different times.

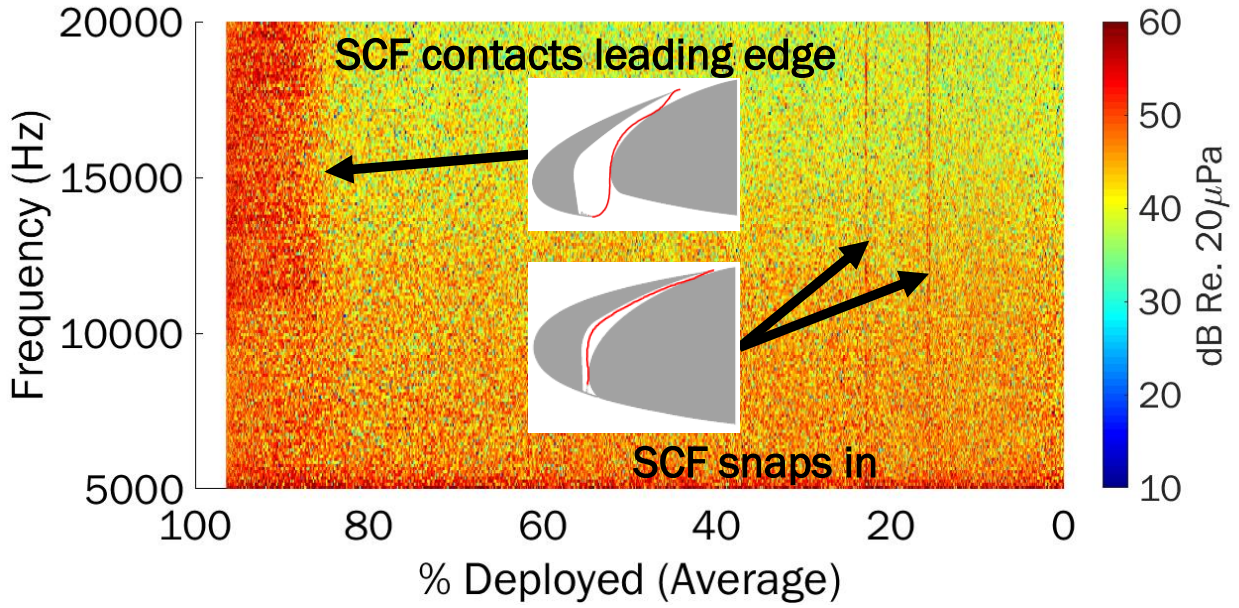

Figure 5.22: Sound Pressure Level at 6°, 30 m/s with a transform length of 512. This dynamic test began fully deployed and ended fully retracted.

Source localization images were added to the spectrogram to create Figure 5.23, which shows the impulsive noise occurred at the slat midspan and top, respectively.

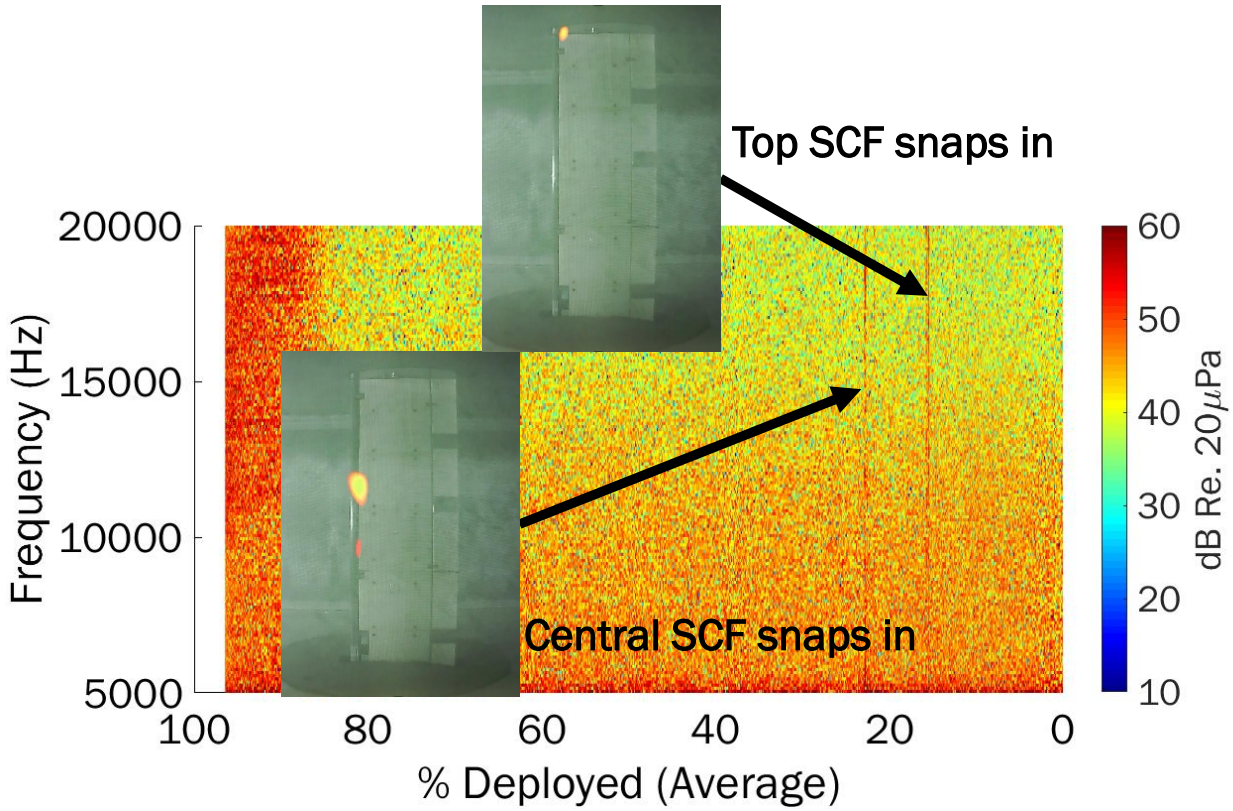

Figure 5.23: Sound Pressure Level at 6°, 30 m/s with a transform length of 512. The associated beamforming image spatially locates each of the snap in events to separate sections of the SCF.

Testing was also completed in the opposite direction, beginning with the slat fully retracted and ending fully deployed. In this sequence, the SCF appears to deploy or "snap out" at approximately 60% deployed, and loses contact with the wing leading edge near 70%, as depicted in Figure 5.24. Similar to Figure 5.22, two sharp tonal noises were detected during the snap-out event. The weaker source, which occurred at around 55% deployed, was caused by the SCF section closest to the roof of the section, with the stronger source caused by the main section snapping out. Once the slat and wing leading edge were no longer in contact and flow could travel between the two, broadband noise production once again began.

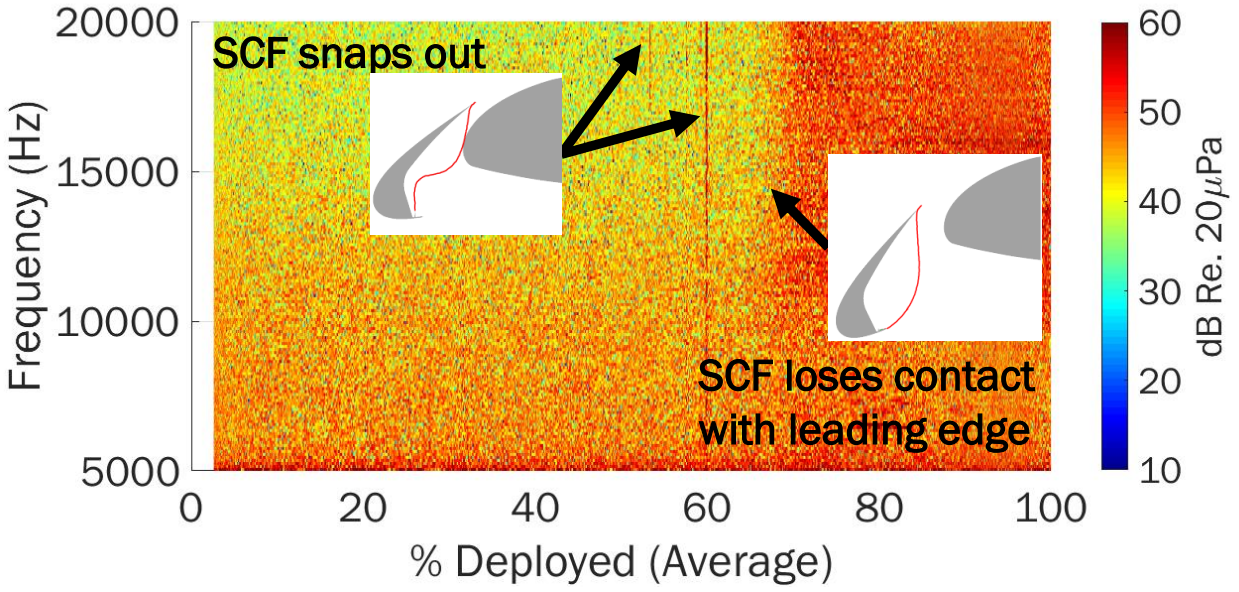

Figure 5.24: Sound Pressure Level at 6°, 30 m/s with a transform length of 512. This dynamic test began fully retracted and ended fully deployed.

While testing lower velocity flow conditions, previously unknown acoustic sources appeared on the spectrograms. Specifically, these structures modulated in frequency and lasted for long periods of time. Once the beamforming array was directed to capture images of these frequencies, the source became clear. It was believed that these acoustic sources were caused by actuator motion, and were never visible prior, as all tests had either been conducted at steady-state deployment levels or noise created by the wing and tunnel overpowered the noise created by these actuators. As depicted in Figure 5.25, the modulating source was located on the body of the wing, exactly where both slat and flap actuators were housed. This was a unique result, as all acoustic sources until this time were found either on the slat or were attributed to tunnel noise (and thus appeared at the section entrance and exit), with no sources appearing on the body of the main wing. This lends credence to the notion that the source was not aerodynamic in nature, but rather occurred beneath the 3D printed airfoil, where the actuators were placed.

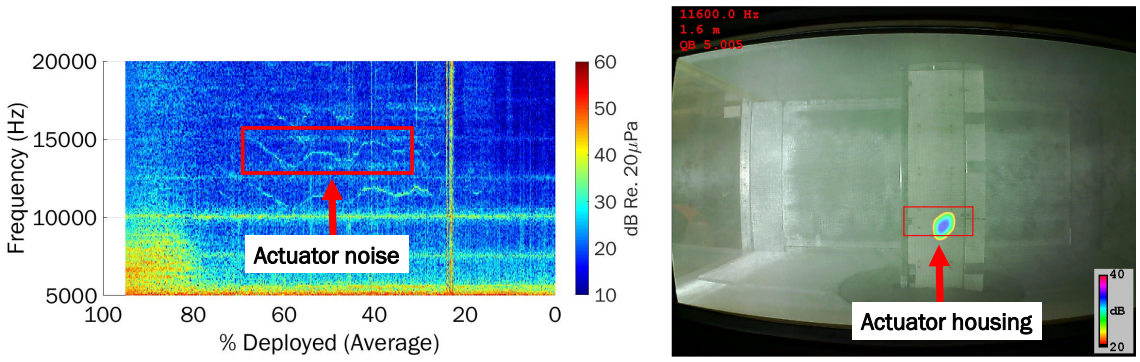

(a) spectrogram

(b) Beamforming image of actuator noise

Figure 5.25: Sound Pressure Level at 6°, 15 m/s with a transform length of 512. The spectrogram indicates a source generating varying frequencies, and beamforming spatially located the source to the actuator housing.

5.4.5 Wind Tunnel Acoustic Diagnostic Capabilities

While observing sound sources was incredibly useful for determining if acoustic noise was created in the slat cove, it was also utilized as a diagnostic tool, enabling real-time discovery of flaws within the CRM model. As depicted in Figure 5.18, a narrowband peak was discovered in several tests. Using conventional single microphones, the source would be exceedingly difficult to track down and fix, but with the acoustic array, the task was trivial. The narrowband frequency in question was entered into BeamformX and the location of the source was discovered. The peak was caused by missing material near one of the slat actuator arms. Flow traversing this region came in contact with this geometric discontinuity, and created a tone which was detected by the microphones. Once the location was found, tape was used to cover the missing material, and the wing was retested. The airfoil issue was highlighted in Figure 5.26, and the frequency content before and after the fix, as well as the beamforming image, are depicted in Figure 5.27. Figure 5.27 clearly demonstrates that the modification removed the tonal source, and this correction was only made possible by beamforming.

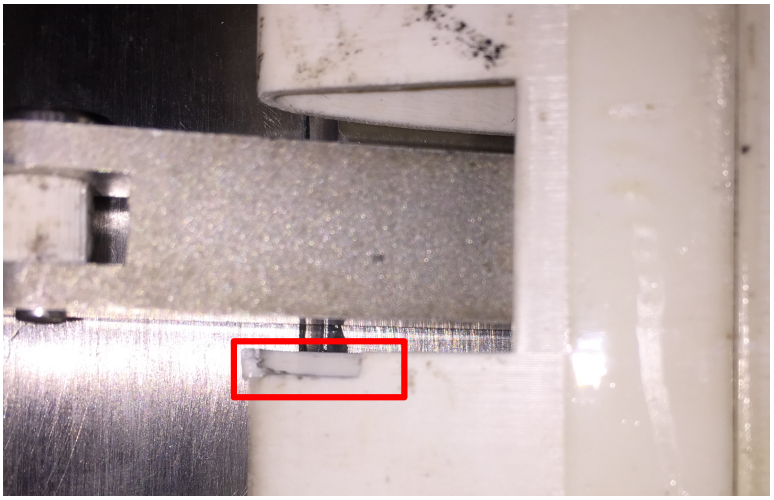

Figure 5.26: Missing material (highlighted in red) on the leading edge of the wing. This geometric discontinuity was the cause of high decibel tonal noise.

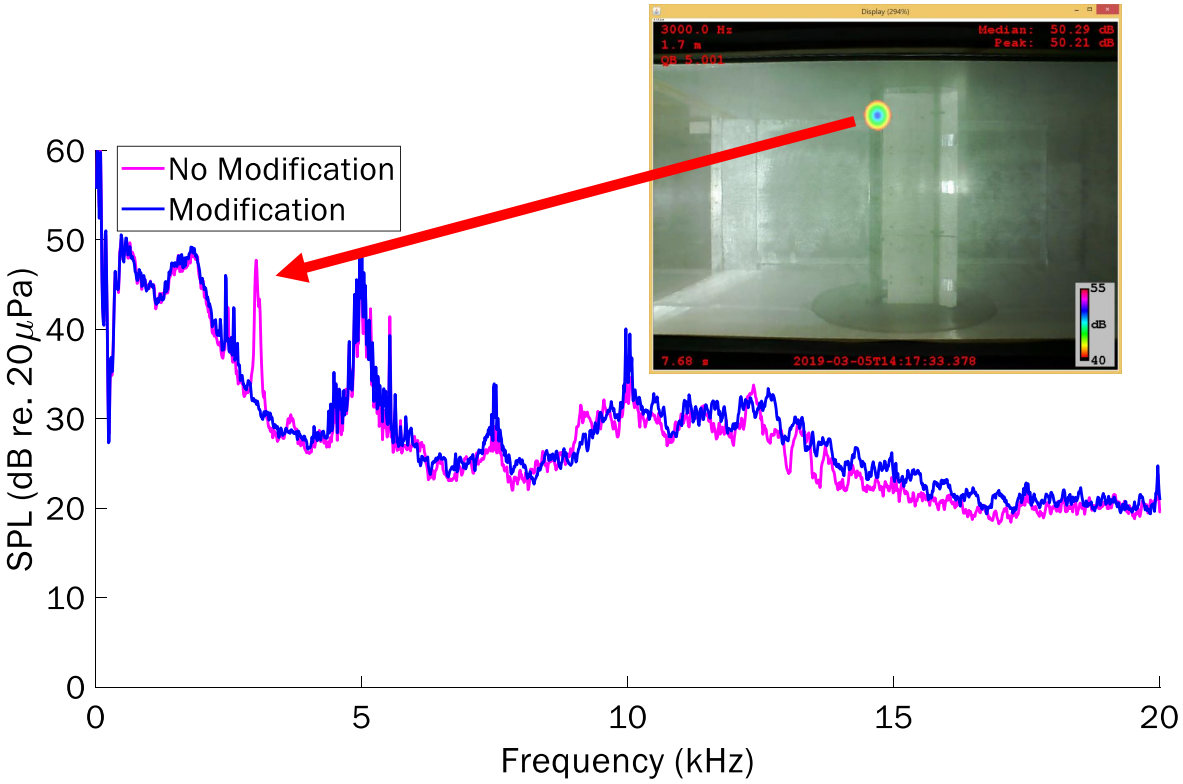

Figure 5.27: Sound Pressure Level of the wing before and after the missing material was remedied. The tone is shown in further detail using an image generated by beamforming, allowing for accurate source location and wind tunnel diagnostics.

5.4.6 3D Printed SCF Acoustic Spectrum Results

In order to gain insights into the acoustic behavior of an "ideal" SCF geometry, the slat with the 3D printed SCF was placed in the aeroacoustic section as well. It was expected that, assuming the ideal geometry was correct for the flow conditions, a noticeable decrease in OASPL would be observed relative to an untreated slat or a slat with an SMA-based SCF. However, at lower speeds, the ideal case actually slightly increased noise production when compared to even the untreated case. This is depicted in Figure 5.28.

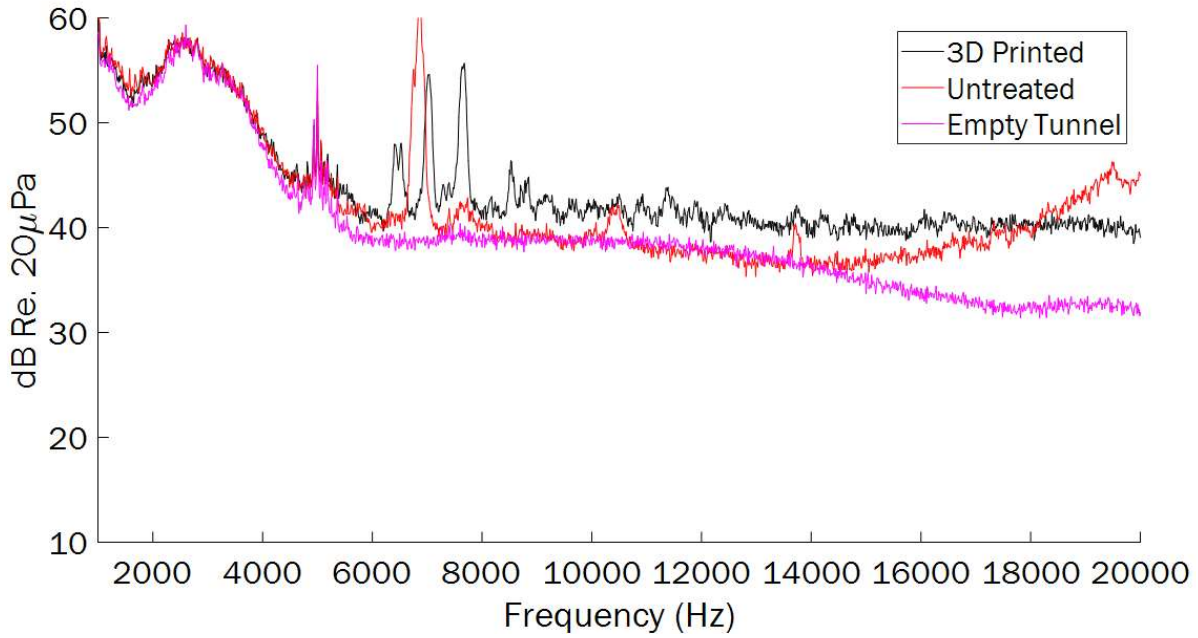

Figure 5.28: Comparison of an untreated slat to a slat with a 3D printed SCF. This test was performed at 30 m/s, 100% deployed, 6°, with a transform length of 4096 for maximum frequency resolution.

This result is unexpected, the underlying reason was further investigated. Two hypotheses were created as a result. The first was that the actual shape of even the ideal SCF was incorrect. This was supported by the fact that the original shape was derived from isobars generated by a computational fluid dynamic model of a full scale, 3-D CRM wing. The 3-D CRM wing had sweep and taper, meaning the 2-D slice used for our model scale (with no sweep or taper) may not have taken into account the complex aerodynamics necessary to find the original SCF geometry as optimal. Therefore, considering the scaling, the proper SCF shape for the 1/16th scale model used at Texas A&M University may vary. The other area of interest was the cavity between the slat cove and the 3D printed SCF. Due to the printing process, it was impossible to create the structure at the same thickness as the SMA (0.002 in). As a result of differing cross-sectional geometry between the 3D printed SCF and SMA SCF, it was possible that span-wise flow within the cavity created different acoustic signals. To test this idea, a cavity filler was 3D printed and installed to block any flow traversing the span of the slat within the slat cove. The test setup is depicted in Figure 5.29. The

entire face of the blocker and SCF were covered in tape to seal any cracks.

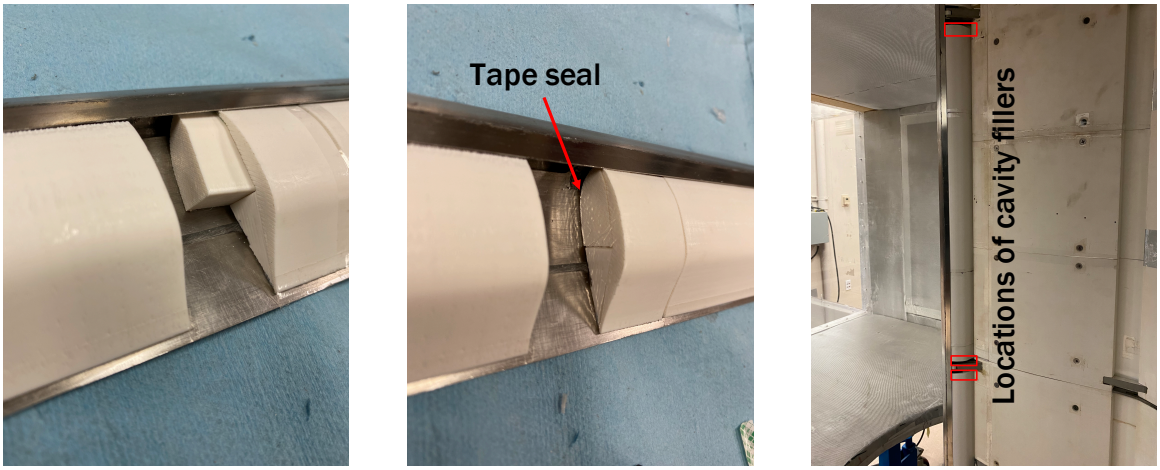

Figure 5.29: Installation of blocker for span-wise flow through the slat.

As a result of the testing, no acoustic savings were found. In fact, noise production increased slightly at all velocities. The spectra comparison between the "original" 3D printed SCF with no blocker and the "cavity filled" configuration is given in Figure 5.30.

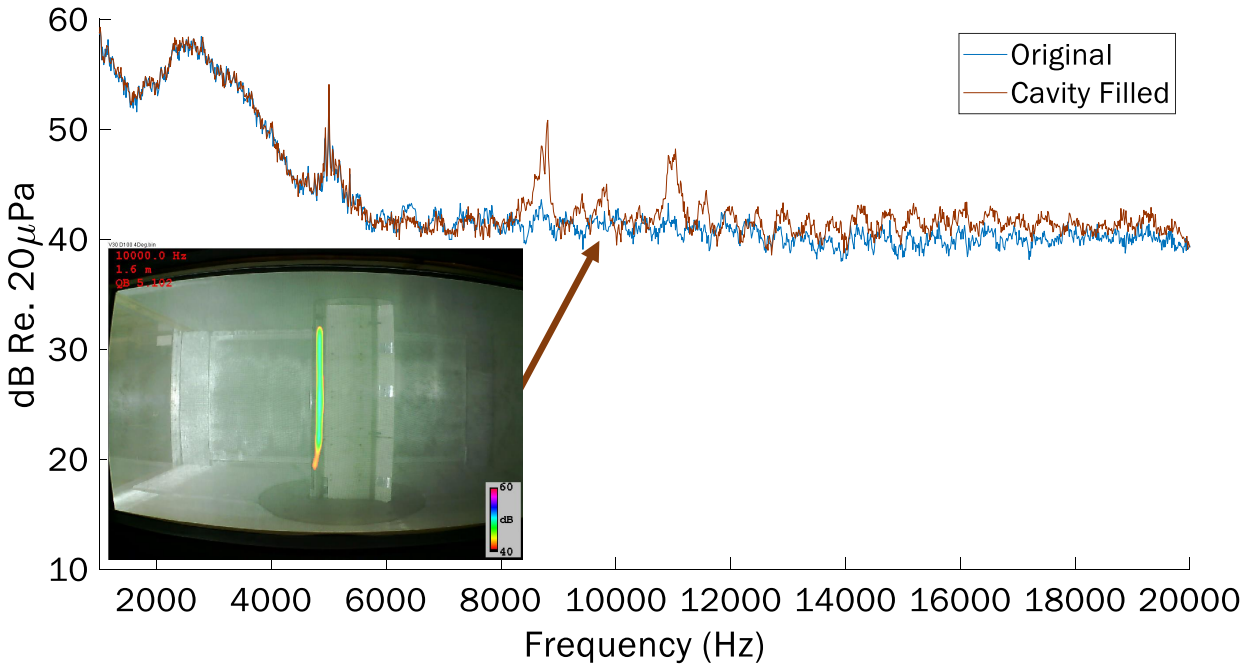

Figure 5.30: Spectrum comparison of 3D printed SCF with and without the span-wise flow blocker. An image produced by beamforming is shown as well, to illustrate the spatial location of broadband noise created by the blocked configuration. This test was performed at 30 m/s, 100% deployed, 4°, with a transform length of 4096 for maximum frequency resolution.

The cavity filled model follows closely with the original 3D printed SCF model, but produces slightly more noise. Additionally, the broadband signal produced is spatially located along the length of the slat, similar to the noise sources seen in both the SMA treated and untreated configurations. As a result, this evidence lends credence to the notion of an incorrect SCF geometry. In fact, Imamura et al. conducted experimental work on various SCF designs and found that small geometric changes to the profile caused large changes to both the spectrum and OASPL [56]. If this is the case, and, using the SMA SCF, acoustic savings have still been identified, then it is logical to assume that a properly formatted SCF for the length scale used in this study would yield acoustic savings to a greater extent.

6. CONCLUSIONS AND FUTURE WORK

6.1 Experimental Conclusion

This study has experimentally proven for the first time the acoustic reduction due to the implementation of an SMA SCF. Knowledge surrounding the acoustic phenomena associated with the SCF, both from a steady-state and dynamic perspective, has increased significantly. Given the reduction in noise across all angles of attack and similar aerodynamic characteristics, full-scale implementation of the SCF seems to be a feasible prospect. Noise production using an SMA SCF was not as distinct (in terms of broadband frequency production) as once hoped from its untreated counterpart, which likely indicated either the shape of the SCF was not correct, and therefore flow was still being separated and circulated, or, trailing edge bluntness was largely responsible for the noise level and should be addressed in follow up work. Likely, both of these two noise creation mechanisms were active during testing, but it was not proven which had a greater effect. An overview of the results from this work are given below:

- Treated produced the same or slightly more coefficient of lift and drag across all angles when fully deployed or fully retracted compared to the untreated case (Figure 3.10). This result corroborates previous experimental and computational work.

- Treated generally produced more coefficient of lift and drag when at intermediate deployment levels (Figure 3.10). This differed from Patterson's experimental work, as his SCF reduced coefficient of drag.

- Treated provided roughly equivalent coefficient of pressure as the untreated case when fully deployed (Figure 3.7), but varied to a great extent when at intermediate deployment levels (Figure 3.8). This result corroborates previous experimental and computational work at fully deployed.

- Roughly similar aerodynamic responses (coefficients of lift and drag moreso than pressure)

were observed between cases when the SCF was stowed and was deployed (Figure 3.10, Figure 3.8).

- Structurally, DIC provided reasonable displacement and shape information (Figure 4.7). The results demonstrated similar behavior to experimental work done by Patterson, though his SCF was 50% thicker.

- SMA-based SCF reduced noise created at all tested angles and velocities compared to the untreated case when fully deployed (Figure 5.20). The greatest acoustics savings were at 15-20 kHz at 20 m/s, where the average OASPL reduction across the tested angle range was 1.5 dB. A larger reduction was expected, but broadband behavior and source placement both indicated the acoustic production mechanism was not fully remedied using the SCF.

- Geometry may not be the optimal design for length and velocity scale, as broadband frequencies shifted instead of dissipating when the SCF was introduced (Figure 5.18).

- Dominant noise production of the wing was localized to slat cove for both treated and untreated cases (Figure 5.21), which suggests that noise production mechanisms still remained.

- Dynamic events such as the SCF stowing and deploying were captured and localized using beamforming (Figure 5.22, Figure 5.23).

- Real-time diagnostic capability was realized enabling fast correction of non-conforming model geometries (Figure 5.26, Figure 5.27).

- 3D printed SCF increased OASPL when compared to the SMA-based SCF, indicating that flow separation and circulation may still be present (Figure 5.28). This may have been indicative that the deformed SMA-based SCF was closer to the optimal geometry than the rigid 3D printed SCF.

- 3D printed SCF coefficient of lift and drag remained similar to the untreated case, but the coefficient of pressure differed at the suction peak (Figure 3.15). As depicted in Figure A.3,

the ports at the leading edge produced 2-3 times the error of subsequent ports, which may have caused this discrepancy. It appeared that any small change in deployment level, flow condition, or angle led to large changes to the suction peak.

6.2 Challenges

The main challenge in this work involved faulty sensors and cables. Originally, untreated aerodynamic and aeroacoustic testing would be completed first, followed by treated testing. However, due to a bad cable connected to one of the load cells in the aerodynamic test section, the load data collected on the untreated slat wasn't trusted. Unfortunately, these erroneous cable readings were not discovered until after the SMA had been epoxied to the slat. For this reason, the SCF had to be removed once all necessary treated SCF data had been collected, in order to collect the necessary untreated aerodynamic data. Had this problem been found sooner, several months of work would have been saved.

6.3 Further Study

In order to build upon this work, several research areas should be attempted. The first, and most simple, is to change the pitch of the fan running the wind tunnel. With minor modification to the wind tunnel, the blades can be pitched to a higher angle, allowing a lower RPM to result in the same flow velocity. With the fan operating at a lower RPM, less background noise would be created (unless the blade tips exceed the speed of sound). This reduction in background noise would enable better aeroacoustic results and comparisons.

The second area of research that should be investigated is, instead of filling the slat cove to reduce flow circulation and noise generation, research [57] has explored the use of a slat gap filler, which prevents flow from passing from the pressure (lower) side to the suction (upper) side of the wing through the gap between the slat trailing edge and leading edge of the wing. As shown in Figure 5.22, as the slat came in contact with the wing (and thus flow between the two was reduced), a significant reduction in SPL was recorded. This result lends credence to the notion that a slat gap filler could reduce just as much noise, if not more, than the SCF. With the two research areas

combined, the future of aeroacoustic testing at Texas A&M University will continue to produce quality and informative data.

Lastly, if the suspicion of an incorrect geometry of the SCF is proven true, additional research could be conducted to first, find the optimal shape for a 1/16th scale mode, and second, determine the aerodynamic, structural, and aeroacoustic performance. Greater acoustic savings may be obtained using this new shape.

REFERENCES

[1] S. Candel, "Concorde and the future of supersonic transport," *Journal of Propulsion and Power*, vol. 20:1, 2004.

[2] ""reduction of noise at source" by international civil aviation organization." Web, 2013.

[3] A. Hansell, M. Blangiardo, and L. F. et al., "Aircraft noise and cardiovascular disease near heathrow airport in london: small area study," *BMJ*, 2013.

[4] J. Mabe, F. Calkins, and G. Butler, "Boeing's variable geometry chevron, morphing aerostructure for jet noise reduction," *AIAA Paper*, 2006-2142.

[5] W. Scholten, D. Hartl, T. Turner, and R. Kidd, "Development and analysis-driven optimization of a superelastic slat-cove filler for airframe noise reduction," *AIAA Paper*, vol. 54, p. 1078–1094, 2016.

[6] K. Mau and W. Dobrzynski, "Flexible airflow separator to reduce aerodynamic noise generated by aleading edge slat of an aircraft wing," *US Patent Nol US 6,789,769 B2*, 2004.

[7] M. Roger and S. Moreau, "Broadband self-noise from loaded fan blades," *AIAA Paper*, vol. 42, 2004.

[8] C. L. Streett, J. H. Casper, D. P. Lockard, M. R. Khorrami, R. W. Stoker, R. Elkoby, W. F. Wenneman, and J. R. Underbrink, "Aerodynamic noise reduction for high-lift devices on a swept wing model," *AIAA Paper*, 2006-212.

[9] W. Horne, K. James, T. Arledge, P. Soderman, N. Burnside, and S. Jaeger, "Measurements of 26 percent-scale 777 airframe noise in the nasa ames 40 by 80 foot wind tunnel," *AIAA Paper*, 2005-2810.

[10] T. Imamura, H. Ura, Y. Yokokawa, S. Enomoto, K. Yamamoto, and T. Hirai, "Designing of slat cove filler as a noise reduction device for leading-edge slat," *AIAA Paper*, 2007-3473.

[11] W. Gleine, K. Mau, and U. Carl, "Aerodynamic noise reducing structure for aircraft wing slats," *US Patent Nol US 6,394,396 B2*, 2002.

[12] T. Turner, R. Kidd, W. Scholten, and D. Hartl, "Development of an sma-based, slat cove filler for reduction of aeroacoustic noise associated with transport-class aircraft wings," *SMASIS Paper*, SMASIS2013-3100.

[13] D. Lagoudas, *Shape Memory Alloys: Modeling and Engineering Applications*. Springer, 2008.

[14] K. Otsuka and C. M. Wayman, *Shape Memory Materials*. Cambridge University Press, 1999.

[15] F. J. Gil and J. A. Planell, "Effect of copper addition on the superelastic behavior of ni-ti shape memory alloys for orthodontic applications," *Journal of Biomedical Materials Research*, vol. 48:5, 2002.

[16] K. Yoshida and H. Furuya, "Mandrel drawing and plug drawing of shape-memory-alloy fine tubes used in catheters and stents," *Journal of Materials Processing Technology*, vol. 153-154, pp. 145–150, 2004.

[17] P. Rossin, "Eyeglasses and parts thereof made with specially processed niti shape memory alloy," *US Patent Nol US 6,557,993 B2*, 2003.

[18] T. Waitz, T. Antretter, F. D. Fischer, and H. P. Karnthaler, "Size effects on martensitic phase transformations in nanocrystalline niti shape memory alloys," *Material Science and Technology*, vol. 24:8, pp. 934–940, 2008.

[19] W. Scholten, R. Patterson, M. Eustice, S. Cook, D. Hartl, T. Strganac, and T. Turner, "Aerodynamic and structural evaluation of an sma slat-cove filler using computational and experimental tools at model scale," *SMASIS Paper*, SMASIS2018-8129.

[20] R. Patterson, "The effects of a sma-based slat cove filler on the aerodynamic and structural characteristics of a wing prototype," *Master's Thesis*, 2017.

[21] H. Stroud, P. Leal, and D. Hartl, "Experimental multiphysical characterization of an sma driven, camber morphing owl wing section," *SPIE Paper*, 2018-10599.

[22] D. J. Hartl and D. C. Lagoudas, "Aerospace applications of shape memory alloys," *Proceedings of the Institution of Mechanical Engineers, Part G: Journal of Aerospace Engineering*, vol. 221(4), pp. 535–552, 2007.

[23] S. Barbarino, E. I. S. Flores, R. M. Ajaj, I. Dayyani, and M. I. Friswell, "A review on shape memory alloys with applications to morphing aircraft," *Smart Materials and Structures*, vol. 23, 2014.

[24] J. K. Strelec, D. C. Lagoudas, M. A. Khan, and J. Yen, "Design and implementation of a shape memory alloy actuated reconfigurable airfoil," *Journal of Intelligent Materials Systems and Structures*, vol. 14, 2003.

[25] J.-H. Roh, K.-S. Kim, and I. Lee, "Shape adaptive airfoil actuated by a shape memory alloy and its aerodynamic characteristics," *Mechanics of Advanced Materials and Structures*, vol. 16(3), 2009.

[26] V. Vishwanathan, M. Szőke, J. E. Duetsch-Patel, D. J. Fritsch, A. Gargiulo, A. Borgoltz, K. T. Lowe, C. J. Roy, and W. J. Devenport, "Aerodynamic design and validation of a contraction profile for flow field improvement and uncertainty quantification in a subsonic wind tunnel," *AIAA Paper*, 2020-2211.

[27] Y. Mayer, H. Jawahar, M. Szoke, S. Ali, and M. Azarpeyvand, "Design and performance of an aeroacoustic wind tunnel facility at the university of bristol," *Applied Acoustics*, vol. 155, pp. 358–370, 2019.

[28] K. Pascioni, R. Reger, A. Edstrand, and L. Cattafesta, "Characterization of an aeroacoustic wind tunnel facility," *Inter-noise*, 2014.

[29] D. Lacy and A. Sclafani, "Development of the high lift common research model (hl-crm): A representative high lift configuration for transonic transports," *AIAA Paper*, 2016-0308.

[30] T. Zimmerman, K. Blohowiak, M. Dilligan, F. Calkins, and J. Mabe, "Adhesive bonding of hybrid acuated shape memory alloy-composite structures," *SAMPE Fall Technical Conf.*, pp. 1–13, 2010.

[31] W. Scholten, R. Patterson, D. Hartl, T. Strganac, Q. Chapelon, and T. Turner, "Computational and experimental fluid-structure interaction analysis of a high-lift wing with a slat-cove filler for noise reduction," *AIAA SciTech Paper*, 2017.

[32] A. Pope, *Wind-Tunnel Testing*. Wiley, 1964.

[33] "Vic-3d 7 manual." Web, November 2016.

[34] J. Duetsch-Patel, V. Vishwanathan, J. Minionis, E. Totten, A. Gargiulo, D. Fritsch, M. Szoke, A. Borgoltz, C. Roy, K. Lowe, and W. Devenport, "Aerodynamic design and assessment of modular test section walls for cfd validation in hybrid anechoic wind tunnels," *AIAA Paper*, 2020-2214.

[35] A. Leaton, W. Scholten, K. Lieb, D. Hartl, T. Strganac, and T. Turner, "Aerostructural and aeroacoustic experimental testing of shape memory alloy slat cove filler," *AIAA Paper*, 2020-1040.

[36] R. Young, "On the energy transported with a sound pulse," *The Journal of the Acoustical Society of America*, vol. 47, p. 441, 1970.

[37] "C-ram sfc wedge technical bulletin 390-2." Web, 2011.

[38] "Beamformx reference manual." Web, 2018.

[39] E. Arcondoulis, L. Brooks, and C. Doolan, "A modification to logarithmic spiral beamforming arrays for aeroacoustic applications," *AIAA Paper*, 2011-2820.

[40] L. de Santana, "Fundementals of acoustic beamforming," *NATO STO-EN-AVT-287*.

[41] M. Remillieux, E. Crede, H. Camargo, R. Burdisso, W. Devenport, M. Rasnick, P. V. Seeters, and A. Chou, "Calibration and demonstration of the new virginia tech anechoic wind tunnel," *AIAA Paper*, 2008-2911.

[42] C. R. Moren, "Pilots, airplanes, and the tangent of three (3) degrees," *The PUMAS Collection*, 1999.

[43] Y. P. Guo, K. J. Yamamoto, and R. M. Stoker, "Experimental study on aircraft landing gear noise," *Journal of Aircraft*, vol. 43(2), 2006.

[44] R. Dougherty, "Functional beamforming," *Berlin Beamforming Conference Paper*, BeBeC-2014-01.

[45] T. Brooks and W. Humphreys, "Extension of damas phased array processing for spatial coherence determination (damas-c)," *AIAA Paper*, 2006-2654.

[46] Y. Yang, Z. Chu, H. Jiang, and Y. He, "Research on damas2 beamforming sound source identification," *Chinese Journal of Scientific Instruments*, vol. 34(8), pp. 1779–1786, 2013.

[47] P. Sijtsma, R. Merino-Martinez, A. Malgoezar, and M. Snellen, "High-resolution clean-sc: Theory and experimental validation," *International Journal of Aeroacoustics*, vol. 16(4-5), pp. 274–298, 2017.

[48] S. Luesutthiviboon, A. Malgoezar, M. Snellen, P. Sijtsma, and D. Simons, "Improving source discrimination performance by using an optimized acoustic array and adaptive high-resolution clean-sc beamforming," *Berlin Beamforming Conference Paper*, BeBeC-2018-D07.

[49] P. Shah, A. White, D. Hensley, D. Papamoschou, and H. Vold, "Continuous-scan phased array measurement methods for turbofan engine acoustic testing," *Proceedings of ASME Turbo Expo 2018*, GT2018-77033.

[50] B. Widrow, "A study of rough amplitude quantization by means of nyquist sampling theory,," *IRE Transactions on Circuit Theory*, vol. 3, no. 4, pp. 266–276, 1956.

[51] T. Brooks, D. S. Pope, and M. Marcolini, "Airfoil self-noise and prediction," *NASA Reference Publication 1218*, 1989.

[52] A.-B. Wang, Z. Travnicek, and K.-C. Chia, "On the relationship of effective reynolds number and strouhal number for the laminar vortex shedding of a heated circular cylinder," *Physics of Fluids*, vol. 12, 2000.

[53] V. Okulov, I. Naumov, R. Mikkelsen, I. Kabardin, and J. Sorensen, "A regular strouhal number for large-scale instability in the far wake of a rotor," *Journal of Fluid Mechanics*, vol. 747, pp. 369–380, 2014.

[54] R.Faventi, H.Hopper, and M. Rodriguez, "Low power transmission plastic gear trains: which parameters affect the subjective acoustic quality?," *Proceedings of the International Gear Conference 2014*, pp. 208–218, 2014.

[55] "Acoustic noise requirement, nasa practice no. pd-ed-1259." Web, May 1996.

[56] T. Imamura, H. Ura, Y. Yokokawa, T. Hirai, and K. Yamamoto, "Numerical and experimental research of low-noise slat using simplified high-lift model," *AIAA Paper*, 2008-2918.

[57] T. Turner and D. Long, "Development of an sma-based, slat-gap filler for airframe noise reduction," *AIAA Paper*, 2015-0730.

APPENDIX A

ERROR ANALYSIS

While repeatability trials were completed on nearly every test to verify that the same experimental data collection procedure would yield the same result, an additional error analysis was completed. This added scrutiny was to investigate how noisy or transient data was without the assistance of time-averaging (used in aerodynamic, pressure, and acoustic measures). First, coefficients of lift and drag were recalculated, incorporating non-time averaged data to find the standard deviation of the data set. This data was then added to the original CL and CD plot for comparison, and shown in Figure A.1 and Figure A.2.

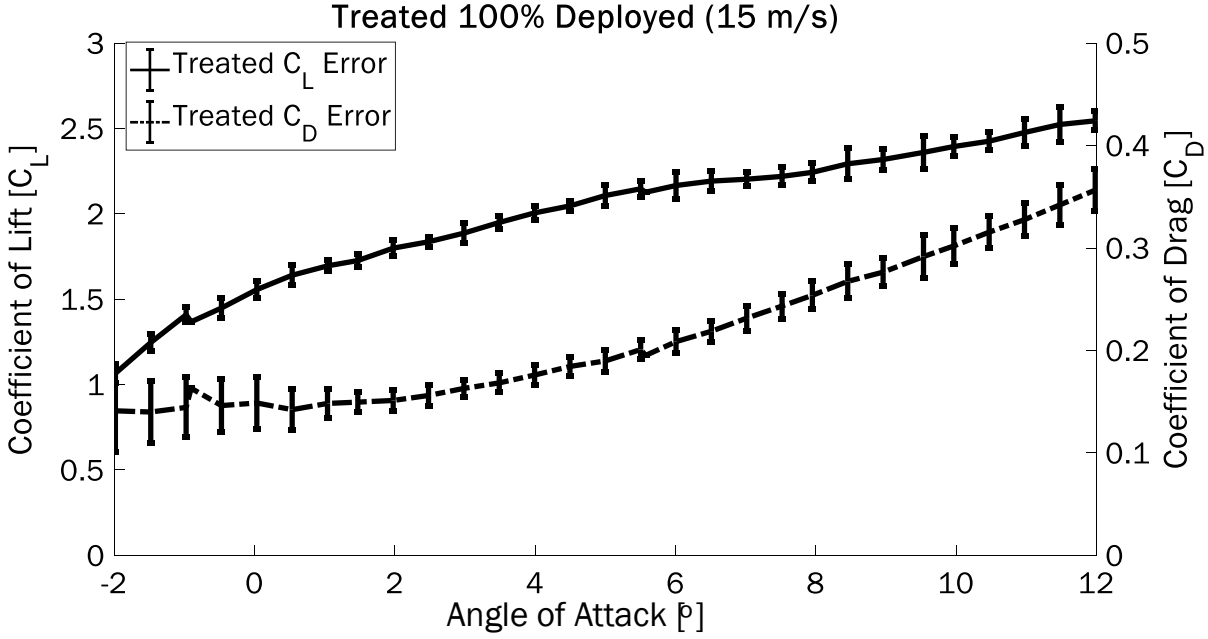

Figure A.1: CL and CD values across a range of angles of attack at 100% deployed and 15 m/s, incorporating error bars depicting one standard deviation.

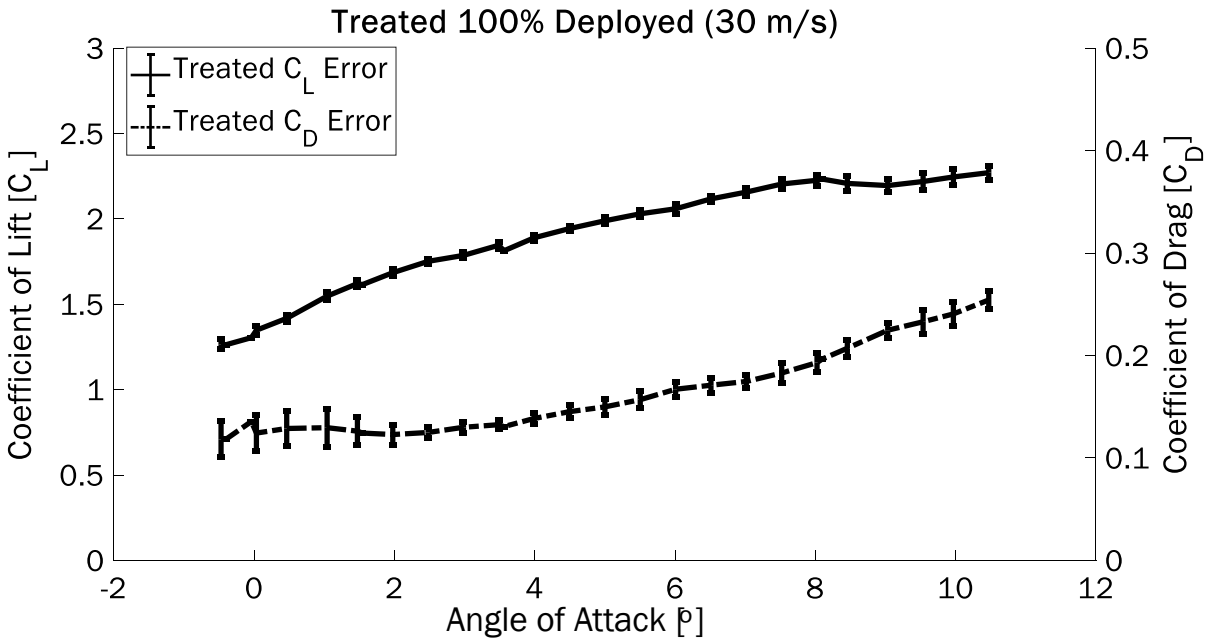

Figure A.2: CL and CD values across a range of angles of attack at 100% deployed and 30 m/s, incorporating error bars depicting one standard deviation.

As depicted above, the errors for coefficients of lift and drag are relatively small, moreso for higher velocity. A likely reason behind this is that, at lower speeds, such as 15 m/s, the wind tunnel fan produced flow velocities with twice the error when compared to 30 m/s. This error then would have propagated to larger variations when calculating dynamic pressure and measuring forces, which would finally influence the coefficients.

Coefficient of pressure was also investigated. For this data, coefficient of variance was used as a measure of error over time. For each position, 100 data points were collected by the pressure sensor over the course of 20 seconds. This data was then time averaged when calculating coefficient of pressure. However, for coefficient of variance, the standard deviation of each of the 15 pressure ports was found along with the mean during the 20 second collection window. The deviation was divided by the mean and multiplied by 100 to yield the coefficient of pressure in %, shown in Eq. (A.1)

$$\text{Coefficient of Variance } (\%) = \frac{\sigma}{\mu} * 100 \tag{A.1}$$

where σ was the standard deviation and μ was the mean. The values are shown in Figure A.3 and Figure A.4. At this specific angle of attack, very little variation is present. However, at high or low angles of attack, when flow either separates from either surface or is simply unsteady, these values increased to nearly 15% near the trailing edge of the wing. These values are shown in Figure A.5. As depicted, it appears separation occurs near the trailing edge, leading to a large variance in data collected over the 20 second period.

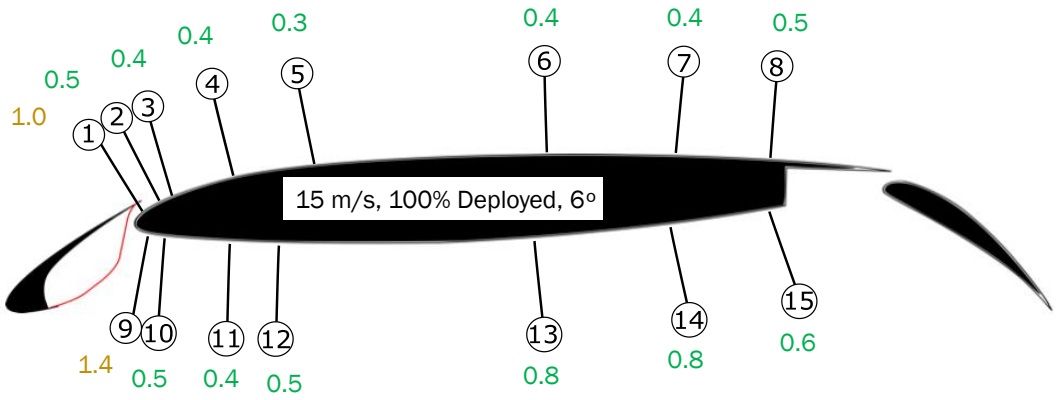

Figure A.3: Coefficient of variance (%) of CP across the chord of the airfoil at 6° and 15 m/s.

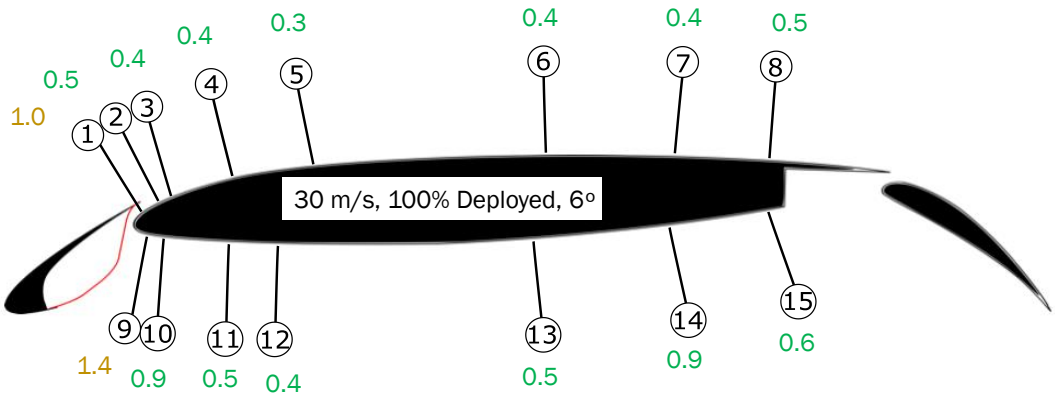

Figure A.4: Coefficient of variance (%) of CP across the chord of the airfoil at 6° and 30 m/s.

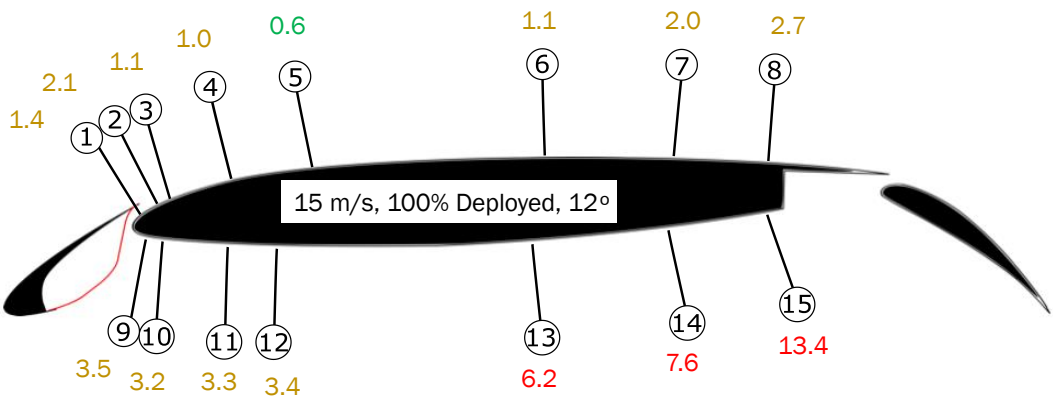

Figure A.5: Coefficient of variance (%) of CP across the chord of the airfoil at 12° and 15 m/s.

Acoustic error was calculated as well. However, due to the random noise associated with acoustic measurements, and the necessary time-averaging used in almost every meaningful measure, the results were deemed unnecessary and are not included in this work.